Active Safety Measures for Vehicles Involved in Light Vehicle-to-Vehicle Impacts

by

Jing Zhou

A dissertation submitted in partial fulfillment
of the requirements for the degree of
Doctor of Philosophy
(Mechanical Engineering)
in The University of Michigan
2009

Doctoral Committee:

Professor Huei Peng, Chair
Professor Timothy J. Gordon
Professor N. Harris McClamroch
Professor Noel C. Perkins

Acknowledgments

First and foremost, I would like to thank my advisor, Professor Huei Peng, for his support, guidance, and motivation throughout my doctoral study. He provided remarkable inspiration and latitude, both of which stimulated me to pursue my interests all along the course of the research.

I also would like to express my deep appreciation to Professor Timothy J. Gordon, Professor N. Harris McClamroch, and Professor Noel C. Perkins, for the valuable suggestions, comments, and time that they shared with me.

I gratefully acknowledge the support from Ford Motor Company through the Ford-University of Michigan Innovation Alliance Project program. Particularly, my gratitude goes to Dr. Jianbo Lu for his guidance, insights into vehicle dynamics and control systems, and care for my personal development. In addition, regular discussions with Dr. Bengt Jacobson of Volvo Cars were vital to this research. I would also like to thank Daniel Eisele at Ford Motor Company for his forthcoming assistance in the veDYNA simulation models used in the study.

I will remember my colleagues and friends, including but not limited to Kangwon Lee, Chan-Chiao Lin, Minjoong Kim, Daekyun Kim, Jinming Liu, Yongsong Chen, Youseok Kou, Sehyun Chang, Sean Yang, Jeong-Seok Kim, and Mikael Thor, whose friendship and inspiring ideas were a great source of encouragement.

Finally, I would like to express my loving appreciation to my wife, Han Zhang, and my parents. Their sustained love and support made this work possible.

Table of Contents

List of Figures

List of Tables

List of Appendices

List of Symbols

a, b	Distance from axles to vehicle CG (m)
a_y	CG lateral acceleration (m/s^2)
C_f , C_r	Cornering stiffness per axle (N/rad)
d	Distance from CG to impact position on vehicle body (m)
D_s	Total suspension roll damping (N·m·s/rad)
e	Coefficient of restitution (-)
F_x, F_y	Longitudinal and lateral forces (N)
F_{yf} , F_{yr}	Lateral tire forces per axle (N)
F_z	Wheel vertical load (N)
g	Gravitational acceleration (m/s^2)
G_b	Linearized gain from cylinder pressure to brake torque (N/bar)
h	Distance from sprung mass CG to the roll axis (m)
h_{CG}	CG height above the ground (m)
I_{xxs}	Sprung mass roll moment of inertia about the roll axis (kg·m^2)
I_{xz}	Sprung mass product of inertia about roll and yaw axes (kg·m^2)
I_{zz}	Vehicle yaw moment of inertia about z axis (kg·m^2)
I_w	Wheel inertia (kg·m^2)
k_δ	Steering wheel turning rate (deg/s)
K_s	Total suspension roll stiffness (N·m/rad)
L	Wheelbase (m)
m_R	Rolling (sprung) mass (kg)
m_{NR}	Non-rolling (unsprung) mass (kg)

M	Total vehicle mass (kg)
M_z	Yaw moment (N·m)
N	Prediction window length (number of time steps)
P_b	Braking pressure (bar)
P_n, P_t	Collision impulses decomposed in *n-t* directions (N·s)
P_x, P_y	Collision impulses decomposed in *x-y* directions (N·s)
Q	Weights penalizing states
R	Weights penalizing control inputs
R_w	Wheel radius (m)
S	Sliding surface tracking error
T_b	Wheel torque (N·m)
T_w	Vehicle track width (m)
u	Actual control input
v	Virtual control input
v_x	Longitudinal velocity (m/s)
v_y	Lateral velocity (m/s)
V_x	Post-impact longitudinal velocity (m/s)
V_y	Post-impact lateral velocity (m/s)
x_A, y_A, z_A	Coordinates locating impact position (m)
Y_{CG}	CG lateral displacement (m)
α	Wheel slip angle (rad)
β	CG sideslip angle (rad)
δ	Road wheel steering angle (rad)
ϕ	Sprung mass roll angle (rad)
η	Convergence rate in sliding mode control
λ	Wheel longitudinal slip ratio (-)
μ	Coefficient of tangential interaction in collision (-)
μ_R	Road adhesion coefficient (-)
θ	Orientation angle of the vehicle before impact (rad)

ω_x	Roll rate (rad/s)
ω_z	Yaw rate (rad/s)
ξ	Polar angle to locate impact position on vehicle body (rad)
ψ	Vehicle yaw angle (rad)
Δt	Duration of collision (s)
Γ	Angle between *n*-*t* and *x*-*y* coordinate systems in collision (rad)
Ω_z	Post-impact yaw rate (rad/s)
Ω_x	Post-impact roll rate (rad/s)

Abstract

Road traffic statistics have shown multi-event crashes typically result in higher fatalities and injuries than single-event crashes do, especially when the initial harmful event leads to a loss of vehicle directional control and causes secondary collisions. In this work, the topic of stabilization control for vehicles involved in light vehicle-to-vehicle impacts is addressed. A post-impact stability control (PISC) system is developed to attenuate undesired vehicle motions (spin-out, skid, rollover) induced by the initial impacts, so that subsequent crashes can be avoided or mitigated.

First a vehicle collision model is developed to characterize vehicle motions due to the light impact, which is based on an assumption of substantial changes of kinematic states but minor structural deformations. Colliding vehicles are modeled as rigid bodies with four degrees of freedom, and the influences of tire forces are taken into consideration to improve the prediction accuracy of collision consequences. Then a collision sensing/validation scheme is developed to detect impulsive disturbances and trigger the activation of PISC. The vehicle responses to the impulse are predicted and used to compare with subsequent measurements for collision confirmation.

The stabilization controller, which is derived from the multiple sliding surface control approach, regulates the disturbed vehicle motions via differential braking/active steering. The system effectiveness is verified through CarSim/Simulink simulations for angled rear-ends collisions. When compared with the performance of existing electronic stability control (ESC) systems and four-wheel braking approach, PISC demonstrates improved capability to reject the collision disturbances and to assist the driver to regain control.

For more integrated control of longitudinal/lateral/yaw/roll motions, a hierarchical control architecture for vehicle handling is proposed. It consists of three coordinated stages: the generation of virtual control commands through model predictive control, the generation of actual commands through constrained optimal allocation, and the tracking of wheel slips at the actuator level. This cascade modular design allows for better trade-off among various control objectives and explicit consideration of control input constraints at handling limits.

This proposed active safety feature can be deemed as a functional extension to current ESC systems, and constitutes a complementary module towards a comprehensive vehicle safety system.

Chapter 1

Introduction

1.1 Motivation

Traffic safety is of great importance for drivers, manufacturers, and government agencies. Significant technological and regulatory efforts have been devoted to promote ground vehicle safety [1]. The safety of automobiles is affected by a variety of factors (Figure 1.1):

- Environment: weather, road pavement, traffic conditions, traffic signs and markings, etc
- Vehicle: maintenance condition, availability and capability of safety features, etc
- Human driver: driving skills, physical and psychological states, etc

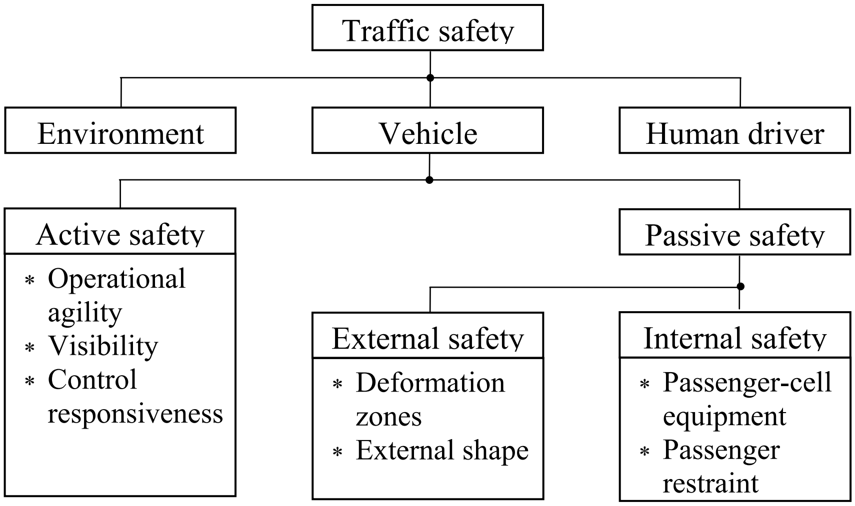

Figure 1.1: Role of vehicle active and passive safety systems in traffic safety [2]

Safety measures from the aspect of vehicle can be broadly categorized into two major fields, active safety and passive safety. They have a profound impact on enhanced vehicle safety. Vehicle active safety systems refer to automotive systems designed for accident prevention and avoidance, as opposed to vehicle passive safety, which includes features that mitigate the severity of injuries if an accident occurs. Popular active safety systems include anti-lock braking system (ABS) [2], electronic stability control (ESC) [3], adaptive cruise control (ACC) [4, 5], lane-keeping assist (LKA) [6], and so on. Passive safety features [7], such as crumple zone designs, reinforced body structural members, restraint systems, and airbags, help to minimize occupant injuries.

Despite tremendous technological advances in vehicle safety, the death toll of road traffic accidents remains steady. According to traffic safety statistics, approximately 6.2 million motor vehicle traffic crashes were reported to the police during 2006 in the United States [8]. Among them, 38,588 crashes involved fatalities and 42,642 people were killed. On the positive side, since more miles are driven by the driver population in recent years, after normalization the trend of traffic safety demonstrates steady progress.

Based on an estimate on traffic statistics [9, 10] using NASS-CDS (National Automotive Sampling System - Crashworthiness Data System) data collected from 1988 through 2004, every year in the US, about 2.9 million light passenger vehicles are involved in crashes that are severe enough to require towing from the scene. Approximately 31% of them are involved in crashes where a second harmful event follows the initial collision. In about 70% of these multiple-event crashes, the second harmful event is a collision with another vehicle. The rest secondary events consists of collisions with fixed objects (23%), such as trees or utility poles, and rollovers (7%).

Although a variety of crash scenarios are included in this analysis, there is clear evidence suggesting that a significant portion of multiple-event collisions involves loss of vehicle stability as a consequence of the initial impacts. The CDS data analysis also suggests that the risks of both injury and fatality increase with the number of collision events. For example, the fatality risk in two-event accidents is twice that of single-event accidents (Table 1.1). In addition, a separate accident statistical study performed by the German Insurance Association confirms that a vehicle involved in a light impact is likely to experience a severe secondary crash, and one-third of all accidents with severe injuries consist of multiple impact events [11].

Table 1.1: Number of impact events vs. maximum injury scale (breakdown in percentage)

Maximum injury scale in crashes	Number of events		
	1	2	≥3
None/Unknown	50.3	39.3	31.9
Minor	41.8	48.6	50.0
Moderate	5.2	7.7	10.3
Serious, severe, critical	2.2	3.4	5.4
Fatal	0.5	1.0	2.4
Sum	100%	100%	100%

Source: NASS-CDS from 1988 through 2004 [9].

An accident archived in the NASS-CDS database provides a representative example to illustrate the severe outcome resulting from an initial minor collision. The case number is NASS-CDS 2003-079-057 [12]. Besides detailed accident and vehicle descriptions, the online database also provides access to multiple on-site and vehicle damage photos.

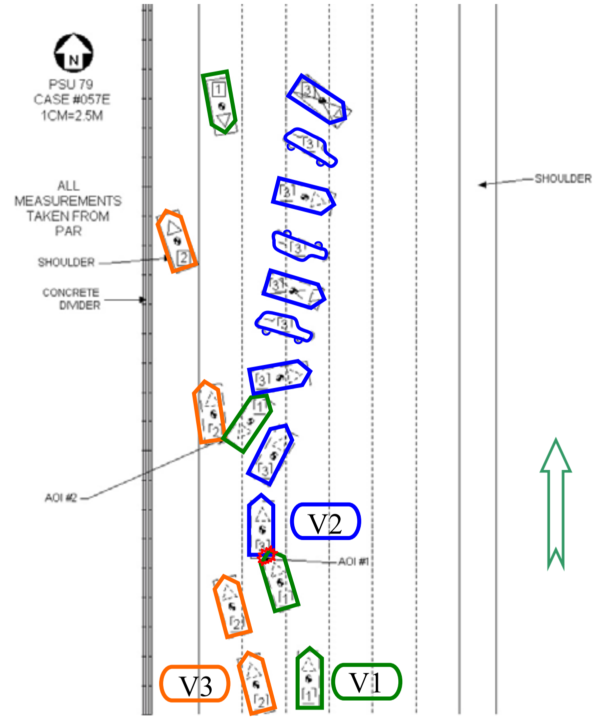

Figure 1.2: Accident sketch of case #NASS-CDS 2003-079-057

This multi-event accident occurred on a physically divided, level, dry, multi-lane highway. The three vehicles involved were originally traveling northbound in separate lanes (Figure 1.2). As Vehicle 1 negotiated a lane change, its left front corner contacted the right rear corner of Vehicle 2. Vehicle 1 spun counter-clockwise then it struck Vehicle 3 as Vehicle 3 veered to the left in an attempt to avoid the crash. Vehicle 2, after being impacted by Vehicle 1, spun clockwise and rolled over about six quarter turns, landing on its roof. Eventually Vehicle 2 was towed with rollover damage and had deployed side curtain air bags. Both driver and occupants of Vehicle 2 incurred visible injuries and were transported by emergency medical service. However, the rear bumper of Vehicle 2 sustained only minor cosmetic damages, and photos in the police report show no substantial structural deformation in the area struck by Vehicle 1. These facts are indications that despite the grave consequences of Vehicle 2, the initial collision with Vehicle 1 was actually minor.

Post-accident analysis found that since current stability control algorithms were not specifically designed to intervene when a vehicle-to-vehicle impact occurs, only limited automatic braking actions were applied. There exists a need to enhance the existing stability controls to counteract the undesired motion of a vehicle after an impact [9, 10].

Therefore, once a collision occurs, it is critical to actively maneuver the vehicle in order to avoid secondary accidents or mitigate their severity. If the vehicle response can be reverted to the operation range familiar to the driver [13], s/he will have a much higher chance to fully stabilize the vehicle. With recent development of advanced vehicle actuation and sensing capabilities, it is reasonable to conceive of post-impact control strategies for improved accident mitigation.

1.2 Research Background

Vehicle accident mitigation is not an uncharted territory. “Precrash safety systems” have emerged as a safety feature to moderate the damage caused by a collision [14]. A precrash safety system monitors the following distance and closing rate between the host and the preceding vehicle, uses audio, visual and tactile signals to alert drivers regarding the risk of collision, and automatically activates braking and tensions seat belts to help mitigate impact damage should a collision become unavoidable. These precrash safety systems are marketed under different names by their manufacturers, for instance, “Collision Warning with Brake Support (CWBS)” by Volvo, “PRE-SAFE” brake support by Mercedes-Benz, and “Collision Mitigation Braking System” by Acura.

Despite the improved protection afforded by precrash safety systems, there is still large room for further improvement. Those precrash safety systems would greatly benefit the bullet (striking) vehicle by alerting its driver to the imminent accident and reducing the impact severity. On the other hand, the protection of the target (struck) vehicle deserves equal attention. Traditionally, efforts in this field have exclusively relied on passive occupant protections. Air bags and other restraint systems have proven valuable in reducing fatalities and injuries. Given the advances in automotive control, sensing, and actuation technologies, opportunities exist for their applications in post-impact control.

Under typical highway driving conditions, a collision between two vehicles can give rise to abrupt changes in vehicle velocities and yaw rates, and may cause the vehicle to deviate from its original course considerably. Without appropriate control, the resulting intense skid, yaw, and/or roll motions may lead to devastating consequences, such as lane departures, secondary collisions with adjacent vehicles or roadside objects, and/or roll-over. In the meantime, drivers may panic or freeze, and thus behave improperly.

The primary objective of this study is to develop a Post-Impact Stability Control (PISC) system, which attenuates undesired vehicle motions (spin-out, skid, rollover) induced by an initial light impact with another vehicle, so that subsequent crashes can be avoided or mitigated. The proposed PISC system constitutes a building block towards a comprehensive vehicle safety system that comprises conventional active safety systems, post-crash active safety measures, and passive safety systems, along with their interactions (Figure 1.3). Such a total safety system expands the operational horizon of active safety systems from preventive measures to post-event mitigation measures, which have previously been the responsibility solely of passive safety devices.

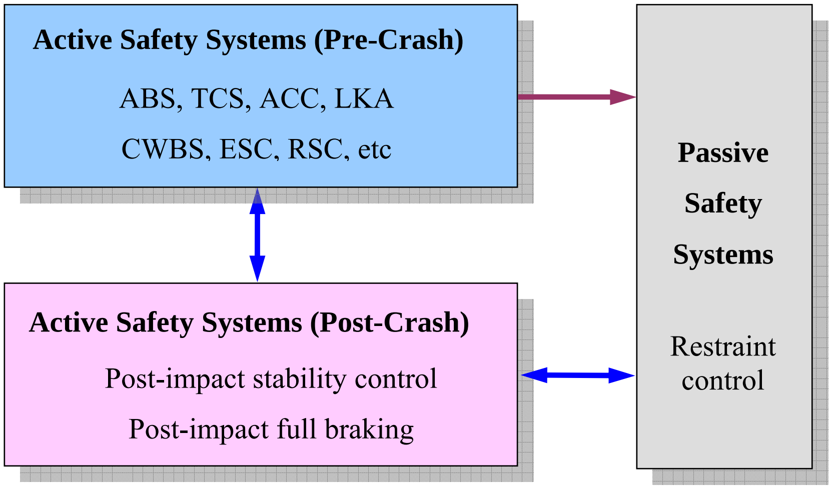

Figure 1.3: Concept of a comprehensive vehicle safety system

Table 1.2: Haddon matrix applied to the analysis of motor vehicle crashes

		Influencing Factors		
		Host – Driver & Occupants	Agent – Vehicle	Environment
Accident Phases	Pre-Crash	Driver inattention; Alcohol impairment; Skills; Risk-taking	Vehicle maintenance & inspection; ABS, ESC, RSC; Crash warning and avoidance	Traffic control devices; Road condition; Weather
	In-Crash	Wearing of seatbelt	Airbag deployment; Restraint system in action; Vehicle crashworthiness	Presence of roadside objects; Location
	Post-Crash	Victims' health status & vulnerability	Fire suppression; Tank integrity Event data recorder, OnStar®	Availability of ambulance & hospital

The Haddon Matrix [15] is frequently used as a template for categorizing both the phases and influencing factors relevant to traffic safety. As shown in Table 1.2, the Haddon Matrix is a three-tiered approach to accident and injury cause analysis. It provides a framework for analyzing accident and injury based on the host (i.e. the person injured), the agent (i.e. the medium that caused the injury), and the environment (i.e. the physical and social context in which the injury occurred). The proposed PISC system serves the dual role as both the post-crash agent element for the initial collision and the pre-crash agent for the possible secondary accidents, thus constitutes an important complementary link to a holistic approach to automotive safety.

Selective braking and/or active steering will be considered as means of actuation for the PISC system, preferably on vehicles already equipped with electronic stability control (ESC) or active front steering (AFS) system. Moreover, unlike the deployment of passive safety devices (front airbags, inflatable side curtains), the activation of the proposed PISC system is reversible, thus offers greater flexibility.

1.3 Related Studies

There are few studies that directly addressed the problem of post-impact vehicle stability control. One prominent example was documented in [10], where the difference between body-force disturbances (such as in a vehicle-to-vehicle impact) and tire-force disturbances is studied and the need for different control design is addressed. An earlier study was reported by Chan *et al.* [16], in which a steering control system was developed to demonstrate the feasibility of post-impact maneuvers that aimed to mitigate accident consequences. A look-ahead steering controller was applied to stabilize the trajectories of vehicles involved in a collision. A number of collision scenarios were simulated to demonstrate the effectiveness of the control system. Other issues such as limitations of applicability and performance requirements were also addressed. However, its controller relied on the information about vehicle position in lane and heading angle, which are challenging to obtain unless a reliable computer vision or a magnetic marker sensing system is installed. Furthermore, the collision scenarios targeted by this work were fairly mild (peak post-impact heading angle < 10°). For collisions with higher severity, steering control alone is probably incapable of stabilizing the vehicle, and a control system integrating steering and braking actuations would be necessary.

In summer 2007, BOSCH released a prototype Secondary Collision Mitigation (SCM) feature built on its CAPS (Combined Active and Passive Safety) system, a modular vehicle safety platform [17]. The SCM function networks between restraint control module (passive safety) and ESP system (active safety), and triggers automatic braking on four wheels after a sensed collision, so that traveling speed can be maximally reduced. Since the total kinetic energy decays fast, the tendency of secondary collisions is averted or at least their severity is moderated. BOSCH anticipates offering this function to automobile manufacturers for integration into their vehicles from 2009.

A significant number of studies have addressed issues related to Electronic Stability Control (ESC). ESC systems provide stability enhancement and handling predictability of vehicles, and have already been widely commercialized on production passenger vehicles by various manufacturers, such as Ford [18], GM [19], BMW [20], Bosch [21], among others. Under Normal driving conditions, vehicles behave linearly and drivers have little problem controlling their vehicles. However, when the vehicle operates close to the friction limit, the tires behave nonlinearly and it becomes challenging for the driver to maneuver. Under such situations, significant vehicle sideslip can develop and the vehicle may lose stability. The ESC system can intervene and assist the driver via differential braking [21], active front steering [22, 23], or active four-wheel-steering (4WS) [24]. Sometimes ESC goes with commercial names such as Electronic Stability Program (ESP), Dynamic Stability Control (DSC), Interactive Vehicle Dynamics (IVD), among others.

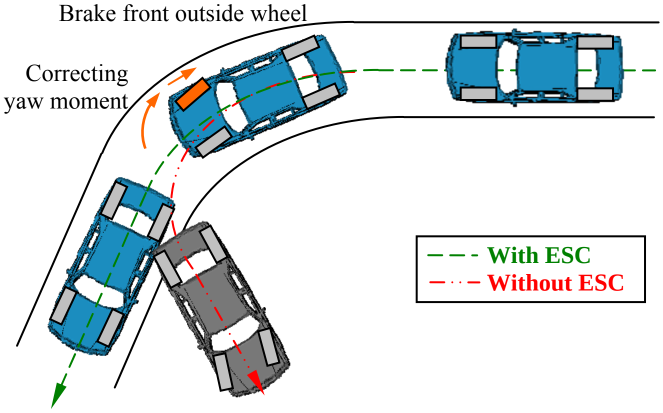

(I) Oversteering – Spinning out

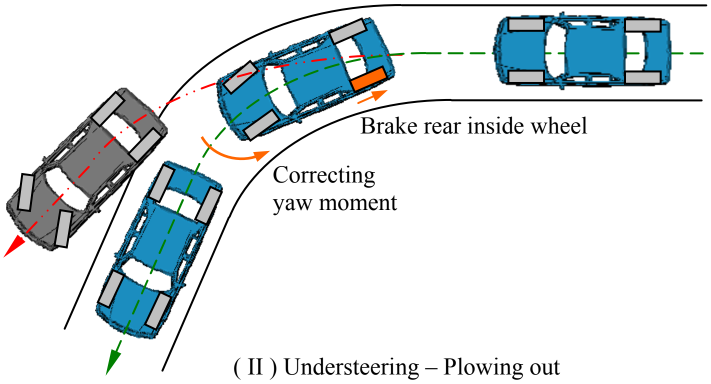

(II) Understeering – Plowing out

Figure 1.4: Operation of ESC systems during understeer and overstee situations

A vehicle equipped with ESC compares driver's intent with the vehicle's responses via measurements of steering wheel angle, lateral acceleration, yaw rate, and individual wheel velocities. When the inferred and measured yaw rates start to diverge, or when significant sideslip angle is developed, the vehicle is judged to be losing control. As a result, the ESC system may selectively activate braking at the four corners, steer actively, and/or reduce engine torque to correct possible oversteering (spin-out) or understeering (plow-out).

Figure 1.4 illustrates two typical ESC correction scenarios. The first is an oversteer scenario in which the vehicle without ESC spins out when cornering. For the vehicle with ESC, a correcting yaw moment is generated by applying brake to the front outside wheel. This reduces oversteer tendency and allows the vehicle to stay on the desired path. The second is an understeer scenario where the vehicle without ESC plows out off the road. For the vehicle with ESC, a correcting yaw moment is generated by applying brake to the rear inside wheel. This reduces understeer tendency and allows the vehicle to follow the desired path.

According to studies from the National Highway Traffic Safety Administration (NHTSA), ESC systems have significantly reduced the amount of fatalities and accidents on American roads [25]. The NHTSA study provided estimates of ESC effectiveness for both cars and sport utility vehicles (SUVs). Based on crash data from 1997 to 2002 in five states, it was found that the reduction in the odds of a single-vehicle crash was 35% for cars and 67% for SUVs. In Sweden, a study using data from crashes reported during 1998 to 2004 [26] shows a positive and consistent effect of ESC as well. The overall effectiveness on all injury crash types, except rear-end crashes, was estimated at 16.7 ± 9.3%, while for serious and fatal crashes, the effectiveness was 21.6 ± 12.8%.

It is noteworthy that by analyzing police-reported crashes in seven states over two years, the Insurance Institute for Highway Safety (IIHS) [27] concluded that ESC affects single-vehicle crashes to a greater extent than multiple-vehicle crashes, and crashes with fatal injuries to a greater extent than less severe crashes. Overall, ESC reduced single-vehicle crash involvement risk by approximately 41%; however, it showed only marginal positive effects on multiple-vehicle crashes (a mere reduction of 3%). This might be due to the fact that many multiple-vehicle crashes like head-on do not lead to unstable vehicle motions. However, there are cases where post-impact vehicle motion can be unstable. One typical example of post-impact stability problem can be seen from the so-called PIT maneuver, where police uses vehicle-to-vehicle contact to spin out a pursued vehicle [28].

The IIHS study substantiated the proposal that ESC systems might need to be enhanced so that they can be more effective in avoiding or mitigating multiple-vehicle crashes or secondary crashes. To some extent, the proposed PISC system shares a number of attributes with the ESC systems currently available on many vehicles [29, 30]. Both systems are intended to assist the driver and aim to prevent the loss of stability in critical driving conditions. For successful operation, both of them depend heavily on measured and estimated vehicle states, in particular yaw rate, lateral acceleration, and sideslip angle. As means of actuation, both achieve their control objectives via selective braking and/or active steering. An assessment of existing electronic stability control systems for post-impact stabilizing purposes was conducted by Thor [31]. Using side-impacts as simulation scenarios, it is found that the benefits of ESC after light collisions depend greatly on how the driver of the struck vehicle reacts during the post impact motion. A competent driver responding in an active and prompt way will receive more assistance from ESC than a "passive" driver does, thus the benefits will be more pronounced for this type of "active" driver.

Compared with automatic control systems, typically it takes more time for the human driver to perceive the risk and take reactions. Brake Reaction Time (BRT) is a measure of the time taken for the driver to move the foot from the accelerator to the brake. A mean BRT value of 0.50 seconds is reported in [32] among 1461 subjects for regular driving. When the driving task is undermined by increasing complexity of the environment and the disposition of the driver (fatigue, drugs, age), BRT can range from three-quarters to two full seconds [33]. For ESC systems to be valuable, it is important for the controller to recognize and follow the driver's intention. Therefore, the driver's intention, interpreted mainly from the steering wheel angle, is fed to the controller, so that a comparison between the desired and the actual trajectories can be made, and proper braking and steering actuators are executed. In case of an unexpected collision, the driver (especially of the struck vehicle) might suffer from physical and mental traumas due to the impact. Consequently, s/he may freeze and this inactivity makes the reaction time even longer. However, since the operation of PISC does not require the involvement of the driver, it gets activated immediately after a collision event is detected. During the crucial one or two seconds after the collision, PISC is supposed to mitigate the intense yaw/roll/skid motions of the vehicle, so that when the driver does start to take actions, the vehicle is more manageable than the case without automatic controls. The reduced level of hazard allows the driver to safely stop or steer clear of roadside objects more easily, and avoid secondary crashes.

1.4 Contributions

Certain light vehicle-to-vehicle collisions can create impulsive disturbance forces and result in abrupt changes of position and orientation for the vehicles involved. This dissertation focuses on the conceptual development of an active safety feature called Post-Impact Stability Control (PISC) system targeting post-crash vehicle stabilization applications. Its major parts include the modeling of light vehicle-to-vehicle collision process, the prompt detection and verification of the impulsive collision disturbances, and the regulation of vehicle states to mitigate intense post-impact vehicle motions. The main contributions of this work are summarized as follows:

- Developed a vehicle-to-vehicle collision model to determine the impulses generated therein and to characterize vehicle sideslip, yaw, and roll motions induced by the impact. The modeling approach is based on a 4-DOF vehicle model and is applicable to collisions without substantial structural deformations. The generation of tire lateral forces during the brief collision process is taken into consideration to improve the modeling accuracy.
- Designed a logic to detect abrupt changes of measurable vehicle states caused by an impulsive disturbance. An accompanying crash validation algorithm is developed to minimize the possibility that the PISC system is improperly activated due to sensor malfunction or noise. An estimation scheme of impulse magnitude and location is built, and the prediction of vehicle responses to the estimated collision impulse is used to verify the presence of impulsive disturbances.

- Devised counteracting measures to mitigate vehicle post-impact skid and yaw motions by employing selective braking, and/or active steering control. Based on the multiple sliding surface control theory, a desired corrective yaw moment is derived and proper braking intervention is determined. System effectiveness and performance enhancement for impacts of various severity and directions are investigated and compared favorably with an existing ESC system.
- Developed a hierarchical control system for vehicle handling, so that multiple control objectives, such as yaw/sideslip attenuation, rollover mitigation, velocity reduction, as well as driver intent following, can be coordinated and prioritized. The proposed control system consists of three stages: virtual command generation, tire force optimal allocation, and wheel slip tracking. It explicitly accommodates constraints on vehicle inputs while seeking to achieve optimal handling performance.

1.5 Outline of the Dissertation

The rest of this dissertation is organized as follows. Chapter 2 presents a collision model to characterize vehicle motion after light impacts, which predicts post-impact vehicle states and computes crash impulses between colliding vehicles. In Chapter 3, a crash sensing and validation scheme is proposed to detect potential crash events. Based on the multiple sliding surface control approach, the design of a post-impact stability controller actuating through differential braking and active steering is conducted in Chapter 4. The proposed PISC system integrates modules for impact detection and validation, desired yaw moment generation, braking force distribution, and front wheel steering command. Its effectiveness is demonstrated in rear-end collision events.

Essentially the nature of post-impact stabilization task is a vehicle state regulation problem on the yaw plane. However, if the vehicle develops a tendency to roll over, the roll stabilization should take priority. Moreover, if there is an additional deceleration request, tire forces have to be distributed to meet both stabilization and speed-reduction objectives. Therefore, a methodology for vehicle handling control consisting of a model predictive control (MPC) based supervisory controller and an optimal tire force allocator is developed in Chapter 5, which is applicable to more general handling tasks. Finally, conclusions and future work are outlined in Chapter 6.

Chapter 2

Collision Model for Vehicle Motion Prediction after Light Impacts

2.1 Introduction

Vehicle collision mechanics has extensive applications in fields such as vehicle crashworthiness, passenger injury analysis, forensic accident reconstructions, and so on. The objective of this chapter is to develop a collision model that predicts the changes of vehicle kinematic states immediately before and after impacts in light vehicle-to-vehicle crashes.

Many vehicle collision models have been developed in the literature. Structural analysis methods can be used to construct complex numerical models (e.g., LS-DYNA [34] and PAM-CRASH [35]) to determine vehicle structural deformations after crashes. However, to use these models, a large set of vehicle component and material properties must be provided.

Additionally, for accidents reconstruction purposes, dedicated softwares such as HVE from the Engineering Dynamics Corporation [36] and PC-Crash from DSD GmbH [37] have been developed. The collision model in HVE is based on the EDSMAC simulation program, which evolved from the SMAC (Simulation Model of Automobile Collisions) program developed by Calspan [38] in the 1970's. To determine vehicle motions during a collision, the algorithm in HVE checks for possible deformation zones caused by the collision and calculates collision forces based on the vehicle structure stiffness and deflections. The forces are then used to calculate accelerations and velocities [36]. In contrast, PC-Crash uses a momentum-based 2- or 3-dimensional collision model. Energy loss is accounted for with a coefficient of restitution. It does not attempt to solve the collision forces during an impact. Instead, it relies on the law of momentum conservation to solve for velocity changes before and after the collision [37].

The focus of this chapter is on the characterization of changes in vehicle kinematic states due to light impacts, and here light impacts refer to those collisions in which vehicles' structural deformations are not substantial, and dimensional changes can be ignored. In addition, all sensors and estimation modules are assumed functional as usual. Newton's equations of motion relating momentum with impulse are the foundations for vehicle collision mechanics [37, 39, 40, 41, 42]. Brach uses this approach extensively in his books [39, 40] to model collision events. The vehicle is typically treated as a rigid body with three degrees of freedom (DOF), and vehicle deformations and contact forces are not directly modeled. Another common assumption made in earlier treatments is that other external forces, such as tire forces and aerodynamic drag, are negligible. Therefore, linear and angular momentums are conserved for the two-vehicle system. Although in many situations the tire forces have much smaller absolute values than the impact forces, the momentum change induced by tire forces may not be trivial during an impact, especially when tire slip angles are large. As will be shown later in this chapter, if tire forces are ignored, appreciable deviations can be introduced in predicting lateral motions of the vehicle in some cases.

Another novel idea proposed in this chapter is to model colliding vehicles as rigid bodies with four degrees of freedom, as opposed to bodies confined in the x-y plane. This approach makes it possible to predict post-impact vehicle roll motion. This additional DOF, along with the inclusion of tire forces during the collision, reduces the error in predicting vehicle lateral and yaw motions. The proposed model is not intended to capture the detailed structural deformations; instead, it is more concerned with the changes in vehicle motions, in particular, longitudinal and lateral velocities as well as yaw and roll rates. Simulation results will be demonstrated by comparing the prediction results of this 4-DOF model against the commercial vehicle dynamics software CarSim.

The rest of this chapter is organized as follows. The momentum-based collision model is reviewed in Section 2.2. Section 2.3 presents a new 4-DOF vehicle dynamics model that accounts for both impact and lateral tire forces. The formulation of the inter-vehicle collision problem using the 4-DOF model is detailed in Section 2.4. The parameter calibration of the modeled vehicle is discussed in Section 2.5. Section 2.6 compares the computation results of the proposed approach against those provided by the traditional momentum-conservation method. In Section 2.7, the proposed approach is applied to analyze a particular police maneuver involving intentional vehicle impacts. Finally, conclusions are drawn in Section 2.8. This chapter was published in [43].

2.2 Momentum-Conservation-Based Collision Model

A well-known impact model based on the conservation of momentum method was developed by Brach [39, 40], which has been used widely for accident reconstruction. This section reviews this planar model, which also serves as both the benchmark, and the foundation for the model proposed later.

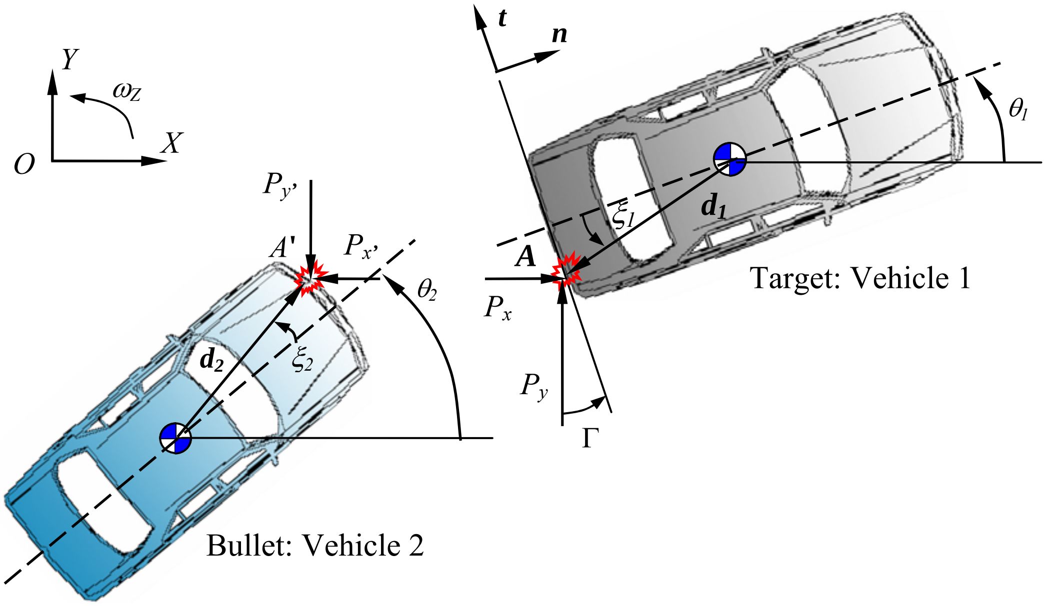

Figure 2.1: A planar view of the free body diagrams for colliding vehicles

Figure 2.1 shows a planar view of the free body diagrams of two colliding vehicles. Throughout the remainder of this chapter, the target vehicle is denoted as Vehicle 1, and the bullet vehicle is denoted as Vehicle 2. An earth-fixed coordinate system (*XOY*) is assumed to align with the road tangential direction. The orientation angle of the vehicles is denoted as θ. An additional local coordinate system (*n-t)* is associated with the impact impulse. The *t*-axis is parallel to a virtual crush plane common to both vehicles, and the *n*-axis is normal to that plane. The choice of the crush plane is case-dependent and should define a nominal deformation surface. The *n-t* coordinate system is related to the *XOY* coordinate system through the angle Γ.

To make the collision problem manageable, additional assumptions need to be made. The resultant impulse vector is assumed to have a specific point of application. Following Brach [39], it is assumed that the location of this point (*A*/*A*') is known and can be located by a distance (d) and a polar angle (ξ) measured from the vehicle center of gravity (CG).

Since the vehicles are confined to the *x-y* plane, six pre-impact vehicle kinematic states (v_{1x}, v_{1y}, ω_{1z}, v_{2x}, v_{2y}, ω_{2z}) are sufficient to describe the motions of the two vehicles. The values of these variables are assumed to be known. Accordingly, there are six unknown post-impact vehicle motion variables (V_{1x}, V_{1y}, Ω_{1z}, V_{2x}, V_{2y}, Ω_{2z}) to be determined. Six independent equations are sought to solve these variables.

In [39], tire forces are ignored and only collision-induced impulse inputs are considered. Linear momentum is thus conserved for the two-vehicle system:

$$P_x = m_1 \cdot \left(V_{1x} - v_{1x}\right) = -m_2 \cdot \left(V_{2x} - v_{2x}\right) \tag{2.1}$$

$$P_y = m_1 \cdot \left(V_{1y} - v_{1y}\right) = -m_2 \cdot \left(V_{2y} - v_{2y}\right) \tag{2.2}$$

By taking moment of the momentum about vehicle CGs, two additional equations can be obtained to relate pre- and post-impact vehicle yaw rates:

$$I_{zz1}\left(\Omega_{1z} - \omega_{1z}\right) = P_x d_c - P_y d_d \tag{2.3}$$

$$I_{zz2}\left(\Omega_{2z} - \omega_{2z}\right) = P_x d_a - P_y d_b \tag{2.4}$$

where $\begin{cases} d_a = d_2 \sin(\theta_2 + \xi_2), & d_c = d_1 \sin(\theta_1 + \xi_1) \\ d_b = d_2 \cos(\theta_2 + \xi_2), & d_d = d_1 \cos(\theta_1 + \xi_1) \end{cases}$.

Finally, two more equations are derived from collision constraints: the coefficient of restitution and the coefficient of tangential interaction [39]. The coefficient of restitution (e) is a lumped measure of the energy loss during an impact. It is defined as the negative ratio of the final to initial relative normal velocity components at the impact point (*A*/*A*').

$$e = -\frac{V_{2n} - V_{1n}}{v_{2n} - v_{1n}} \tag{2.5}$$

The magnitude of the coefficient of restitution depends on the body/bumper materials, surface geometry [44], impact velocity [45], mass difference, among other factors. Determining its value accurately requires extensive empirical data. Typical values of e are found to have an inverse relationship to closing velocity [46], and range between 0.0 and 0.3 for rear-end impacts [47]. As shown in Figure 2.2, large variation in test results exists. Inter-vehicle velocity difference also significantly affects its value.

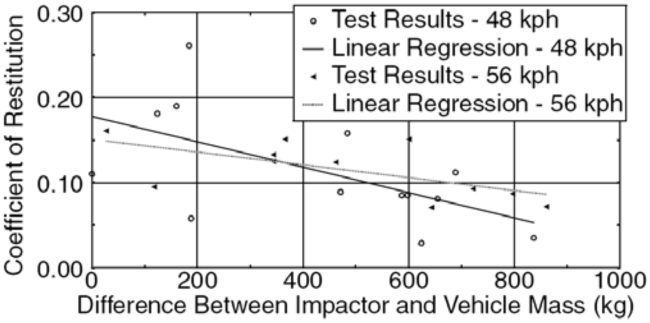

Figure 2.2: Coefficient of restitution vs. mass difference in rear-end collision tests [47]

From Figure 2.1, the normal components of the vehicle velocities at the impact point (*A*/*A*') can be substituted into Eq. (2.5) to obtain

$$\begin{aligned}&\left(V_{1y} - d_d \Omega_{1z} - V_{2y} - d_b \Omega_{2z}\right)\sin\Gamma + \left(V_{1x} + d_c \Omega_{1z} - V_{2x} + d_a \Omega_{2z}\right)\cos\Gamma = \\ &-e\left[\left(v_{1y} - d_d \omega_{1z} - v_{2y} - d_b \omega_{2z}\right)\sin\Gamma + \left(v_{1x} + d_c \omega_{1z} - v_{2x} + d_a \omega_{2z}\right)\cos\Gamma\right]\end{aligned} \tag{2.6}$$

The coefficient of tangential interaction (μ) is a lumped measure of the frictional dissipation during the impact, and relates the tangential impulse with the normal impulse:

$$\mu = \frac{P_t}{P_n} \tag{2.7}$$

A detailed discussion of inter-vehicle friction and its application in accident reconstruction can be found in [48]. By decomposing the total impulse along the *n*-*t* axes, one obtains

$$\mu \cdot \left(P_x \cos\Gamma + P_y \sin\Gamma\right) = P_y \cos\Gamma - P_x \sin\Gamma \tag{2.8}$$

Collecting Eqs. (2.1), (2.2), (2.3), (2.4), (2.6) and (2.8), and assembling them into a matrix form lead to

$$
\begin{pmatrix}
m_1 & m_2 & 0 & 0 & 0 & 0 \\
0 & 0 & m_1 & m_2 & 0 & 0 \\
0 & m_2 d_c & m_1 d_d & 0 & I_{zz1} & 0 \\
0 & m_2 d_a & m_1 d_b & 0 & 0 & I_{zz2} \\
\cos\Gamma & -\cos\Gamma & \sin\Gamma & -\sin\Gamma & d_c\cos\Gamma - d_d\sin\Gamma & d_a\cos\Gamma - d_b\sin\Gamma \\
0 & m_2\left(\sin\Gamma + \mu\cos\Gamma\right) & m_1\left(\cos\Gamma - \mu\sin\Gamma\right) & 0 & 0 & 0
\end{pmatrix}
\cdot
\begin{pmatrix}
V_{1x} \\ V_{2x} \\ V_{1y} \\ V_{2y} \\ \Omega_{1z} \\ \Omega_{2z}
\end{pmatrix}
=
$$

$$
\begin{pmatrix}
m_1 & m_2 & 0 & 0 & 0 & 0 \\
0 & 0 & m_1 & m_2 & 0 & 0 \\
0 & m_2 d_c & m_1 d_d & 0 & I_{zz1} & 0 \\
0 & m_2 d_a & m_1 d_b & 0 & 0 & I_{zz2} \\
-e\cos\Gamma & e\cos\Gamma & -e\sin\Gamma & e\sin\Gamma & -e\left(d_c\cos\Gamma - d_d\sin\Gamma\right) & -e\left(d_a\cos\Gamma - d_b\sin\Gamma\right) \\
0 & m_2\left(\sin\Gamma + \mu\cos\Gamma\right) & m_1\left(\cos\Gamma - \mu\sin\Gamma\right) & 0 & 0 & 0
\end{pmatrix}
\cdot
\begin{pmatrix}
v_{1x} \\ v_{2x} \\ v_{1y} \\ v_{2y} \\ \omega_{1z} \\ \omega_{2z}
\end{pmatrix}
\tag{2.9}
$$

If vehicle parameters and collision conditions (such as orientation angle, coefficient of restitution, etc.) are known, Eq. (2.9) can be solved either forwards (given the pre-impact states, predict the post-impact states) or backwards (given the post-impact states, reconstruct the pre-impact states). The only exception is when $e = 0$, the coefficient matrix on the right hand side becomes singular, and the pre-impact vehicle states cannot be uniquely reconstructed.

2.3 Four-DOF Vehicle Dynamics Model

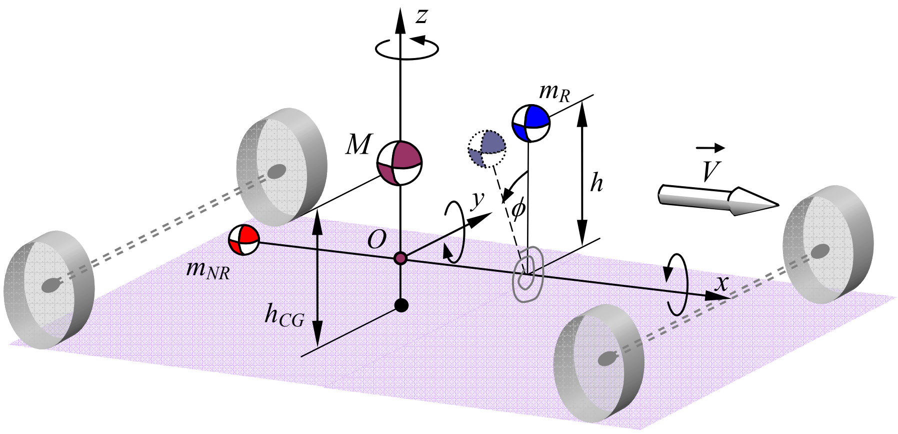

Figure 2.3: 3D schematic diagram of a 4-DOF vehicle model

The impact model presented in the previous section is a 3-DOF planar model, which only accounts for longitudinal, lateral, and yaw motions. In this section, a 4-DOF model based on Segel's lateral-yaw-roll model [49] is employed to develop a new impact model. Heave and pitch motions of the vehicle are ignored. The schematic diagram of the vehicle model is shown in Figure 2.3.

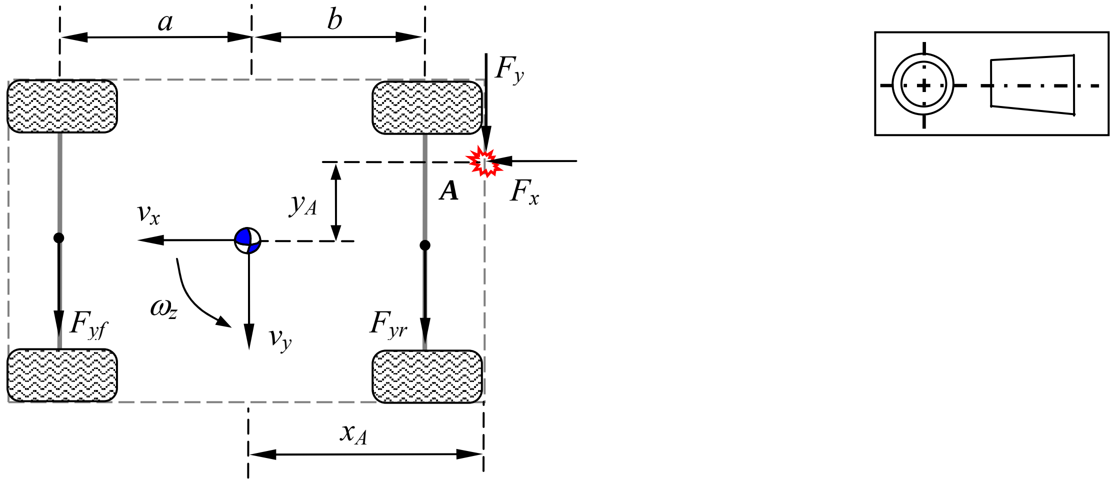

(a) Top view

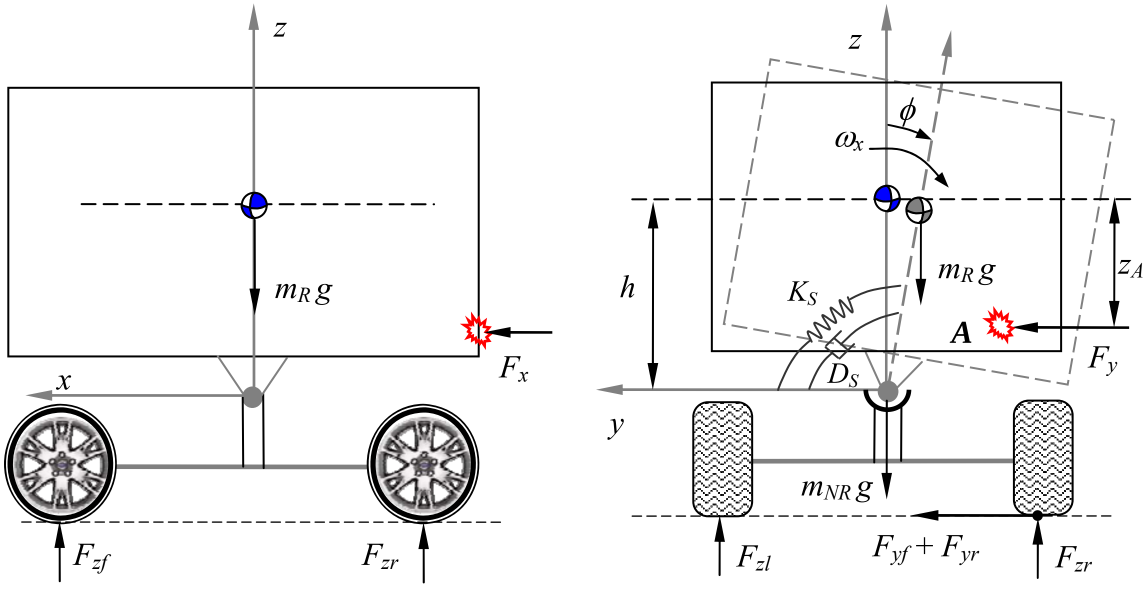

(b) Side view

(c) Rear view

Figure 2.4: Schematic diagrams of the vehicle model with impact forces applied

This vehicle model separates the rolling (sprung) mass m_R from the non-rolling (unsprung) mass m_{NR}. The rolling mass interacts with the non-rolling mass via suspensions (not shown). The effect of the suspension elements at four corners is lumped into an equivalent torsional spring and a damper around the roll axis (see also Figure 2.4 (c)). The overall CG of the vehicle is denoted *M*. The coordinate system *xyz* is fixed on the vehicle body, and its orientation conforms to the ISO coordinate convention. The roll axis (the same as the *x*-axis here) passes through the non-rolling mass and is assumed parallel to the ground. The distance between the rolling mass CG and the roll axis is denoted h, whereas the height of the overall CG above the ground is denoted h_{CG}.

Figure 2.4 shows this vehicle model in three orthogonal views with impact forces applied to the rear bumper. Also shown are vehicle longitudinal velocity (v_x), lateral velocity (v_y), yaw rate (ω_z), and roll rate (ω_x). The impact forces (F_x, F_y) are assumed horizontal only. The impact position (A) is located by the coordinates (x_A, y_A, z_A), and both x_A and y_A are negative in the rear-end collision scenario depicted in Figure 2.4. The equations of motion in terms of longitudinal, lateral velocities, as well as rotational motion about the *x*-axis (roll) and the *z*-axis (yaw) can be written as

$$M(\dot{v}_x - v_y\omega_z) = F_x \tag{2.10}$$

$$M(\dot{v}_y + v_x\omega_z) - m_R h\dot{\omega}_x = F_y + F_{yf} + F_{yr} \tag{2.11}$$

$$I_{zz}\dot{\omega}_z + I_{xz}\dot{\omega}_x = x_A F_y - y_A F_x + aF_{yf} - bF_{yr} \tag{2.12}$$

$$I_{xxs}\dot{\omega}_x + I_{xz}\dot{\omega}_z - m_R h(\dot{v}_y + v_x\omega_z) = F_y\left(z_A - h\right) + (m_R gh - K_s)\phi - D_s\omega_x \tag{2.13}$$

where $\begin{cases} F_{yf} = C_f\left(\delta_f - \dfrac{v_y + a\omega_z}{v_x}\right), & \left|F_{yf}\right| < Mg\mu_R\dfrac{b}{L} \\ F_{yr} = C_r\left(\dfrac{-v_y + b\omega_z}{v_x}\right), & \left|F_{yr}\right| < Mg\mu_R\dfrac{a}{L} \end{cases}$.

In other words, the lateral tire forces F_{yf} and F_{yr} are assumed to vary linearly with slip angles [50] through per-axle cornering stiffness C_f and C_r, but saturate at the static adhesion limits.

2.4 Four-DOF Vehicle Collision Model

In this section, a 4-DOF vehicle collision model is developed. To simplify the equations, it is assumed that the fore-aft centerline of the target vehicle is parallel to the road (θ_l = 0). Two additional local coordinate systems are defined in Figure 2.5. The coordinate system x-y is fixed on the target vehicle and the system x'-y' is fixed on the bullet vehicle, corresponding to their longitudinal and lateral axes respectively. The action and reaction impact forces can then be decomposed into F_x and F_y, or $F_{x'}$ and $F_{y'}$, which relates more directly to the vehicle dynamics. A total of 12 unknowns need to be solved: post-impact longitudinal and lateral velocities, yaw and roll rates for both bullet and target vehicles (V_{1x}, V_{1y}, Ω_{1z}, Ω_{1x}, $V_{2x'}$, $V_{2y'}$, Ω_{2z}, $\Omega_{2x'}$), as well as the collision-induced impulses acting on the vehicles (P_x, P_y, $P_{x'}$, $P_{y'}$). The eight pre-impact vehicle states (v_{1x}, v_{1y}, ω_{1z}, ω_{1x}, $v_{2x'}$, $v_{2y'}$, ω_{2z}, $\omega_{2x'}$) are assumed to be available.

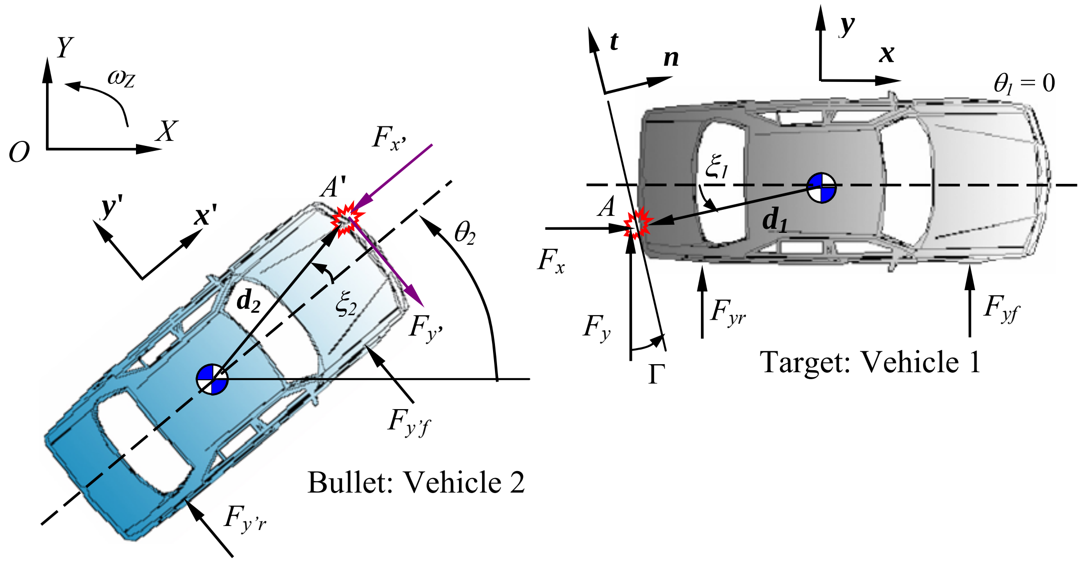

Figure 2.5: A planar view of colliding vehicles with body-fixed coordinates systems

During a collision, peak acceleration levels are high, and velocity changes are limited in magnitude. The typical time duration for a collision is around 0.1 to 0.2 second [46, 51, 52]. A time duration of this magnitude justifies a trapezoidal approximation for the integral of cross-terms in Eqs. (2.10)-(2.13). Equations (2.14)-(2.17) present the formulation in integral form for the target vehicle. The corresponding four equations for the bullet vehicle can be obtained in the same way and are omitted here.

$$M_1 \cdot \left(V_{1x} - v_{1x}\right) - M_1 \frac{\Delta t}{2}\left(V_{1y}\Omega_{1z} + v_{1y}\omega_{1z}\right) = P_x \tag{2.14}$$

$$\begin{aligned} &M_1 \cdot \left(V_{1y} - v_{1y}\right) + M_1 \frac{\Delta \mathrm{t}}{2}\left(V_{1x}\Omega_{1z} + v_{1x}\omega_{1z}\right) - m_{R1}h_1 \cdot \left(\Omega_{1x} - \omega_{1x}\right) = \\ &\quad P_y - \frac{\Delta \mathrm{t}}{2} C_{f1}\left(\frac{V_{1y} + a_1\Omega_{1z}}{V_{1x}} - \frac{v_{1y} + a_1\omega_{1z}}{v_{1x}}\right) - \frac{\Delta \mathrm{t}}{2} C_{r1}\left(\frac{V_{1y} - b_1\Omega_{1z}}{V_{1x}} - \frac{v_{1y} - b_1\omega_{1z}}{v_{1x}}\right) \end{aligned} \tag{2.15}$$

$$\begin{aligned} &I_{zz1}\left(\Omega_{1z} - \omega_{1z}\right) + I_{xz1}\left(\Omega_{1x} - \omega_{1x}\right) = P_y x_A - P_x y_A - \\ &\quad \frac{\Delta \mathrm{t}}{2} a_1 C_{f1}\left(\frac{V_{1y} + a_1\Omega_{1z}}{V_{1x}} - \frac{v_{1y} + a_1\omega_{1z}}{v_{1x}}\right) + \frac{\Delta \mathrm{t}}{2} b_1 C_{r1}\left(\frac{V_{1y} - b_1\Omega_{1z}}{V_{1x}} - \frac{v_{1y} - b_1\omega_{1z}}{v_{1x}}\right) \end{aligned} \tag{2.16}$$

$$\begin{aligned} &I_{xxs1}\left(\Omega_{1x} - \omega_{1x}\right) + I_{xz1}\left(\Omega_{1z} - \omega_{1z}\right) - m_{R1}h_1 \cdot \left(V_{1y} - v_{1y}\right) - \\ &\quad m_{R1}h_1 \frac{\Delta \mathrm{t}}{2}\left(V_{1x}\Omega_{1z} + v_{1x}\omega_{1z}\right) = P_y\left(z_A - h_1\right) - D_{s1}\frac{\Delta \mathrm{t}}{2}\left(\Omega_{1x} + \omega_{1x}\right) \end{aligned} \tag{2.17}$$

In the above equations, the duration of collision (Δt) is assumed known. Lateral tire forces appear in the equations for lateral and yaw motions and assumed to develop instantaneously when sideslip angle is present. When the vehicle is subject to substantial lateral/yaw motions, lateral tire forces may reach saturation limits even before the collision ends. In that case, the lateral tire force terms in Eqs. (2.15) and (2.16) will be replaced with tire adhesion limits.

Two additional equations are derived from the coefficient of restitution (*e*) and the coefficient of tangential interaction (μ), both of which are assumed to be known a priori. The restitution relationship is described by Eq. (2.18) and the tangential interaction is accounted for in the same way as in Eq. (2.8).

$$\begin{aligned} &\left[\left(V_{2x'}\cos\theta_2 - V_{2y'}\sin\theta_2 - d_a\Omega_{2z}\right)\cos\Gamma + \left(V_{2x'}\sin\theta_2 + V_{2y'}\cos\theta_2 + d_b\Omega_{2z}\right)\sin\Gamma\right] - \\ &\quad \left[\left(V_{1x} + d_c\Omega_{1z}\right)\cos\Gamma + \left(V_{1y} - d_d\Omega_{1z}\right)\sin\Gamma\right] = e\left[\left(v_{1x} + d_c\omega_{1z}\right)\cos\Gamma + \left(v_{1y} - d_d\omega_{1z}\right)\sin\Gamma\right] - \\ &\quad e\left[\left(v_{2x'}\cos\theta_2 - v_{2y'}\sin\theta_2 - d_a\omega_{2z}\right)\cos\Gamma + \left(v_{2x'}\sin\theta_2 + v_{2y'}\cos\theta_2 + d_b\omega_{2z}\right)\sin\Gamma\right] \end{aligned} \tag{2.18}$$

Finally, two more equations projects the collision impulses from the bullet vehicle coordinate frame to the target vehicle coordinate frame.

$$P_x = -P_{x'}\cos\theta_2 + P_{y'}\sin\theta_2 \tag{2.19}$$

$$P_y = -P_{x'}\sin\theta_2 - P_{y'}\cos\theta_2 \tag{2.20}$$

These 12 equations can be collected and assembled in a matrix form that relates the post-impact vehicle states to the pre-impact states. Equation (2.21) presents the block-matrix formulation for a special collision scenario, in which both vehicles are assumed to travel along their own longitudinal axes when the collision occurs. The specific terms in matrix **A** and vector **B** are detailed in Appendix A. The formulation for cases with nonzero pre-impact v_y, ω_z, ω_x can be readily accommodated by modifying corresponding entries in **B**.

$$\begin{pmatrix} A_{11} & \mathbf{0} & A_{13} \\ \mathbf{0} & A_{22} & A_{23} \\ A_{31} & A_{32} & A_{33} \end{pmatrix} \cdot \mathbf{x} = \mathbf{B} \tag{2.21}$$

where $\mathbf{x} = \begin{pmatrix} V_{1x} & V_{1y} & \Omega_{1z} & \Omega_{1x} & V_{2x'} & V_{2y'} & \Omega_{2z} & \Omega_{2x'} & P_x & P_y & P_{x'} & P_{y'} \end{pmatrix}'$.

It should be pointed out that unknown velocities (V_{1x}, V_{1y}, $V_{2x'}$, $V_{2y'}$) also appear in the coefficient matrix on the left hand side, thus the 12 unknowns cannot be solved by direct matrix inversion. This problem can be cast into a nonlinear least-squares formulation and be solved by general optimization routines (such as lsqnonlin in Matlab). As a more practical solution, pre-impact velocities (v_{1x}, v_{1y}, $v_{2x'}$, $v_{2y'}$) can be used as initial guesses for the four unknown velocities. Then the post-impact vehicle states and corresponding impulses can be obtained by iteratively solving the 12 algebraic equations, until a specified tolerance is met between two successive iterations.

The contact force at the impact point cannot be determined directly from this model. Various collision impulse shapes (sinusoidal, square, triangular, and sine square profiles) have been proposed to fit observed accelerometer signals in crash experiments [52, 53]. In the end, after the collision impulses have been resolved, given the assumed collision time duration Δt, the impact force profile can be approximated.

2.5 Obtain Vehicle Parameters for Simulation

In order to verify the improved accuracy of the proposed approach over the method based on the momentum-conservation assumption, simulated collisions need to be set up to compare the computation results numerically. The staged collision is also implemented in CarSim®, a widely-used nonlinear multi-body vehicle dynamics software from the Mechanical Simulation Corporation [54]. CarSim simulates and analyzes the dynamic behavior of light vehicles on 3-D road surfaces. It is capable of predicting 3D forces and vehicle motions in response to driver inputs (steering, braking, etc) as well as other external sources (for instance, impacts and wind gusts). CarSim also generates a great number of output variables for visualization and analysis, and allows an interactive animation of simulated tests.

Parameters for the 4-DOF vehicle model need to be specified before a computation is performed. Some vehicle parameters can be obtained directly from the definition files in CarSim, such as vehicle mass, inertia, and length measures; others are less straightforward, since they are either lumped (such as suspension stiffness and damping) or have to be linearized (such as tire cornering stiffness). In order to fully specify the parameters for the 4-DOF model, an array of simulations are run with both the CarSim model and the 4-DOF model. Then the responses to the same input are compared and the to-be-determined parameters are tuned to achieve a reasonably close agreement.

Based on vehicle equations of motion at steady state, tire cornering stiffness can be obtained by solving Eqs. (2.22) and (2.23) simultaneously.

$$Mv_x\omega_z = C_f\left(\delta_f - \frac{v_y + a\omega_z}{v_x}\right) + C_r\left(\frac{-v_y + b\omega_z}{v_x}\right) \tag{2.22}$$

$$\frac{\omega_z}{\delta_f} = \frac{v_x}{L + K_{us}v_x^2} \tag{2.23}$$

where the understeer coefficient $K_{us} = \frac{M}{L}\left(\frac{b}{C_f} - \frac{a}{C_r}\right)$.

The relationship between roll angle and lateral acceleration at steady state is given by Eq. (2.24), from which the total suspension stiffness K_s can be computed. Then the total suspension damping D_s is adjusted to achieve a reasonable match during the transient roll motion.

$$K_s = m_R h(g + \frac{a_y}{\phi}) \tag{2.24}$$

The vehicle parameters are summarized in Table 2.1, which corresponds to the “Baseline Big SUV” dataset in CarSim. Figure 2.6 presents a comparison of responses when both models are subject to a step input in steering wheel angle, which induces a lateral acceleration of 0.2 g at steady state. In all subplots, solid lines represent responses from the CarSim model and dashed lines are from the 4-DOF model. A sufficiently close agreement between these two sets of responses has been achieved, especially at the steady-state.

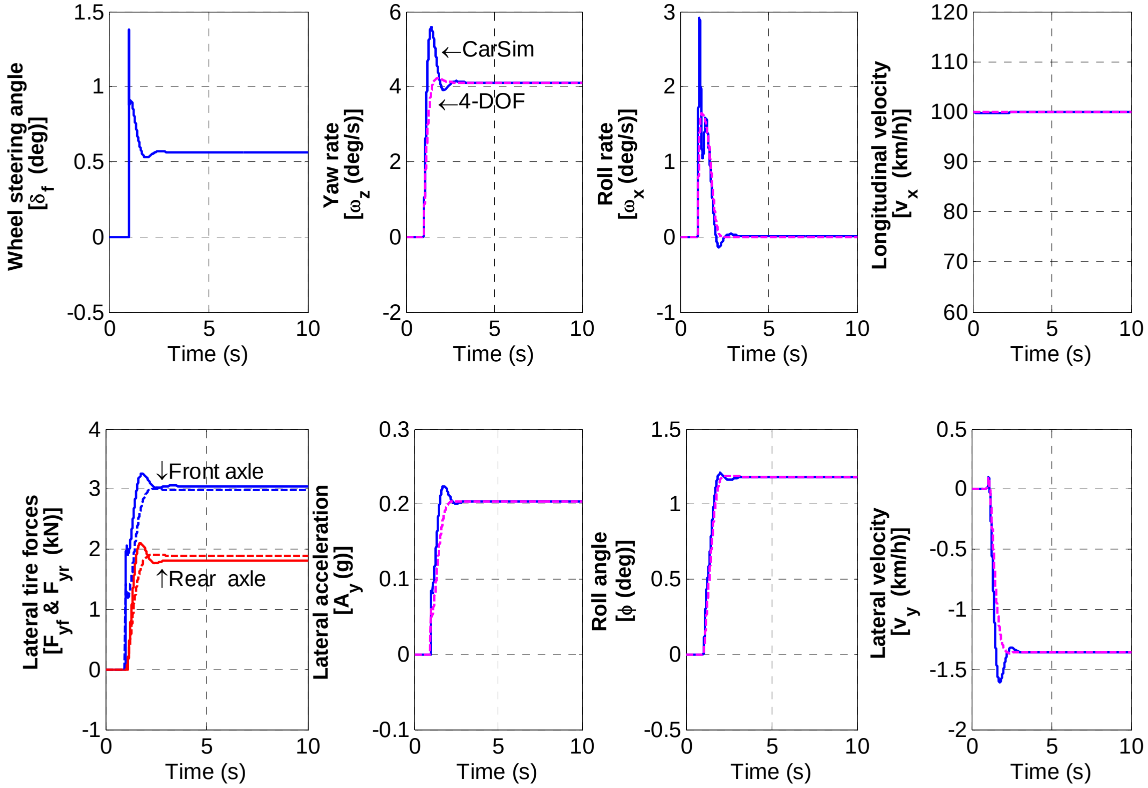

Figure 2.6: A comparison of responses from a CarSim model and a 4-DOF model to a step steering angle input (a_{yss} = 0.2 g)

Table 2.1: Vehicle parameters for the 4-DOF "big SUV" model

Parameter	Description	Value	Unit
M	Total vehicle mass	2450	kg
m_R	Rolling mass	2210	kg
m_{NR}	Non-rolling mass	240	kg
a, b	Distance from axles to vehicle CG	1.105, 1.745	m
L	Wheelbase	2.850	m
h_{CG}	CG height above the ground	0.66	m
h	Distance from sprung mass CG to the roll axis	0.40	m
I_{zz}	Vehicle yaw moment of inertia about z axis	4946	kg·m^2
I_{xz}	Sprung mass product of inertia about roll and yaw axes	40	kg·m^2
I_{xxs}	Sprung mass roll moment of inertia about the roll axis	1597	kg·m^2
K_s	Total suspension roll stiffness	94000	N·m/rad
D_s	Total suspension roll damping	8000	N·m·s/rad
C_f	Front axle cornering stiffness	145750	N/rad
C_r	Rear axle cornering stiffness	104830	N/rad

2.6 Comparison of Collision Computation Results

The accuracy of the developed impact model is studied in this section. The computation results from CarSim serve as the benchmark to assess the accuracy of the planar model and the proposed 4-DOF collision model.

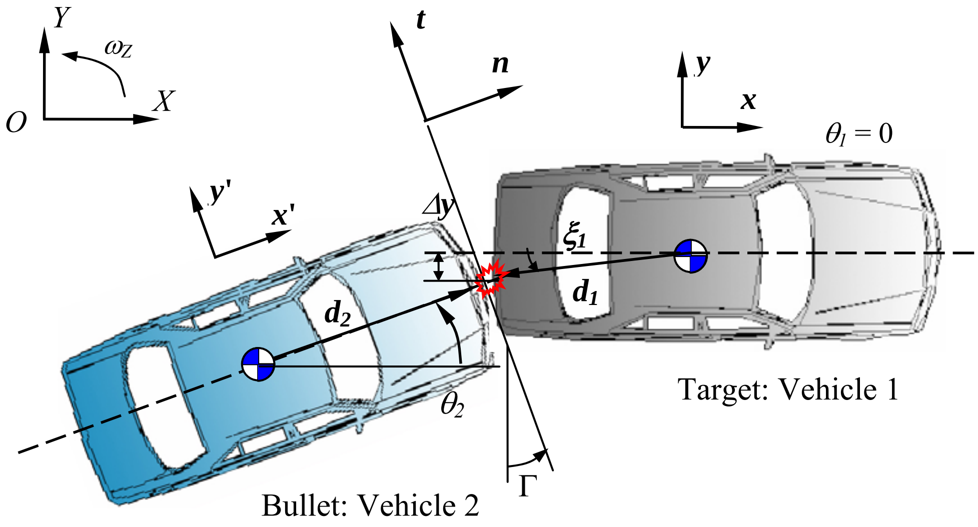

Figure 2.7: An angled rear-end collision. Assume the bullet vehicle is subject to longitudinal forces only

In the simulation, the bullet and target vehicles are identical vehicles with parameters summarized in Table 2.1, which correspond to the "baseline big SUV" dataset in CarSim. The collision scenario is illustrated in Figure 2.7. Before the impact, the target vehicle is aligned with the road tangent, whereas the bullet vehicle has a certain orientation angle θ_2. Both the bullet and target vehicles are traveling along their longitudinal directions when the collision occurs, with $v_{1x} = 29$ m/s, $v_{2x'} = 33.5$ m/s; their initial lateral velocity, yaw rate, and roll rate are all zero. The coefficient of restitution (e) is assumed to be 0.20 for this rear-end crash. It is further assumed that no tangential impulse is generated during the collision ($\mu = 0$). The road adhesion condition is assumed at $\mu_R = 0.70$.

It is assumed that the impact point of the bullet vehicle is located at the center of its front bumper ($\xi_2 = 0$), and no lateral impulse is generated on the bullet vehicle ($P_{y'} = 0$). Therefore, the bullet vehicle is subject only to longitudinal resistant impulses, and no post-impact lateral/yaw/roll motions will be generated on it.

The study will focus on the post-impact motions of the target vehicle. The impact location of the target vehicle (Δy) is 0.1 m to the left of the rear bumper center, and the impact incidence angle θ_2 is 25°. Computation results of more general settings will be presented later in this section. According to the computation in CarSim, after the impact the bullet vehicle remains on the original course, but its velocity is reduced to $V_{2x'} = 30.6$ m/s. The post-impact states of the target vehicle at the end of the collision ($\Delta t = 0.15$ s) are shown in Table 2.2 under the column heading "CarSim."

Table 2.2: Comparison of computation results in an angled rear-end collision

Kinematic States		Bullet Vehicle	Target Vehicle		
			CarSim	4-DOF	Planar
Pre-impact	v_x (m/s)	33.5×cos25°	29		
	v_y (m/s)	33.5×sin25°	0		
	ω_z (deg/s)	0	0		
Post-impact	V_x (m/s)	30.6×cos25°	31.3	31.1	31.9
	V_y (m/s)	30.6×sin25°	4.3	4.5	1.4
	Ω_z (deg/s)	0	-89.9	-95.3	-109.0
	Ω_x (deg/s)	0	-13.2	-15.8	—

The time responses to impact forces of the target vehicle are shown in Figure 2.8. The collision starts at 2.0 s and ends at 2.15 s. The impact forces (F_x, F_y), which are based on the collision impulse, are assumed to follow triangle profiles. Intense yaw motion and transient roll motion are generated by the collision. As a result, large tire slip angles make lateral tire forces saturate at adhesion limits. Since no driver intervention or activation of vehicle stability systems is scheduled, the vehicle simply spins out and skids sideways after the impact, eventually with a lateral acceleration of approximately 0.7g.

The same collision problem is then solved by both the proposed approach based on the 4-DOF vehicle model and the momentum-conservation method as formulated in Section 2.2. For easier comparison, the obtained post-impact states of the target vehicle are collected in Table 2.2 under the headings "4-DOF" and "planar" separately.

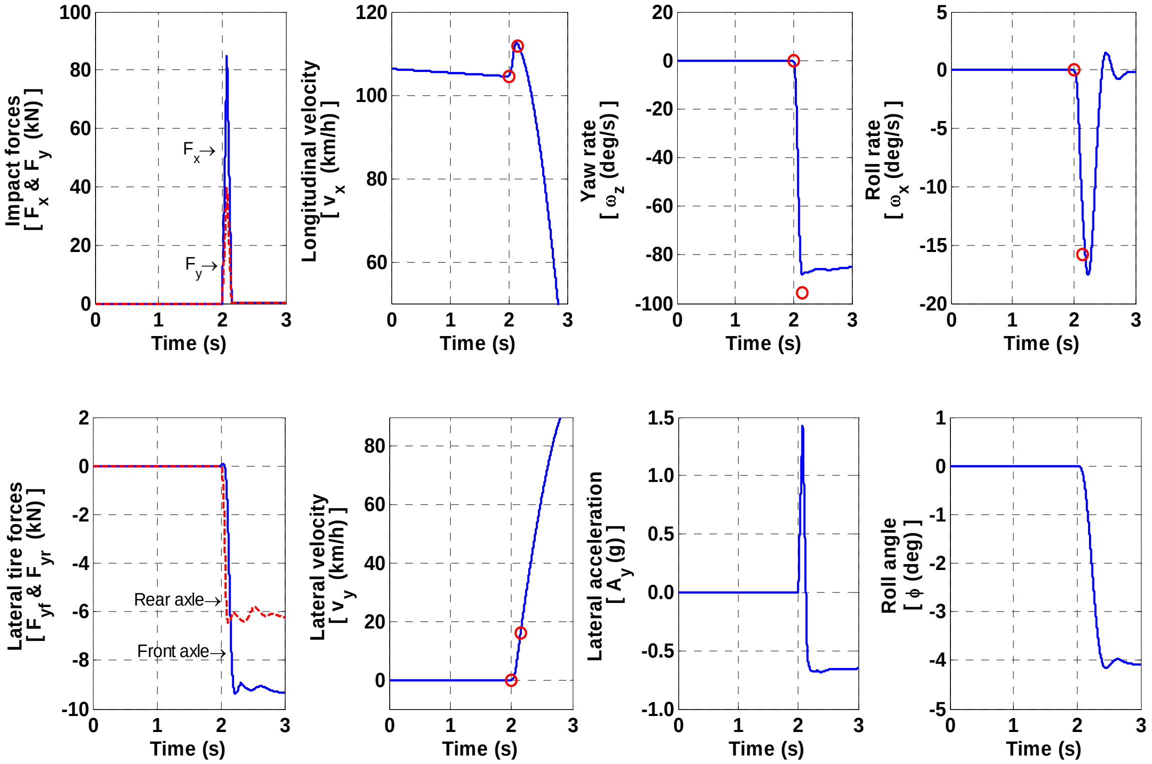

Figure 2.8: Response of the target vehicle involved in a collision. Circles indicate the pre-impact and the post-impact vehicle states predicted by the proposed approach

With the proposed approach, the post-impact translational velocities agree well with those computed by CarSim. Compared with the results obtained from the planar model, the accuracy of predicted yaw rate and roll rate are also improved. The error in roll rate prediction is largely due to the nonlinear effects of the suspensions. The pre- and post-impact translational and rotational velocities are also plotted on Figure 2.8 and marked with circles for easier comparison.

The momentum-conservation-based planar model over-predicts the yaw rate, and cannot be used to calculate the vehicle roll motion. As a matter of fact, if one further analyzes the CarSim results within the collision time interval, it is found that the ratio of the impulses due to tire lateral forces and those due to the external impact is roughly 0.37 for this particular case, a value too substantial to be disregarded. By ignoring the contribution of tire forces in a collision, the momentum-conservation computation risks producing appreciable errors in predicted results [31].

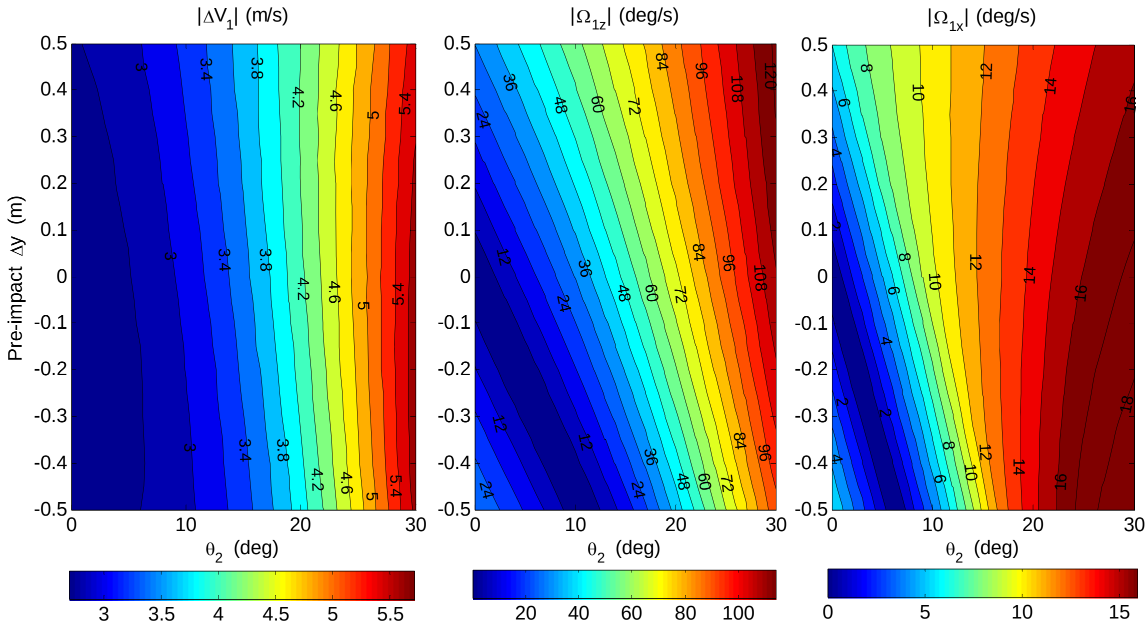

Figure 2.9: Contour plots of absolute CG velocity change, post-impact yaw rate, and roll rate for the target vehicle in angled rear-end collisions

Figure 2.9 shows contour plots for a matrix of rear-end collisions, with respect to absolute CG velocity change, post-impact yaw rate, and roll rate for the target vehicle. The simulated rear-end collisions are similar to that illustrated in Figure 2.7, but the incidence angle of the bullet vehicle and the impact point on the target vehicle are varied. Prior to the impact, the target vehicle was parallel to the road tangent, and the bullet vehicle had an orientation angle (θ_2) varying between 0° and 30°, whereas the collision offset (Δy) ranges between -0.5 m and 0.5 m. Both vehicles were traveling along their own longitudinal axes, with velocities v_{1x} = 29 m/s and $v_{2x'}$ = 33.5 m/s. Values of collision coefficients are assumed to be the same for all cases: $e = 0.20$, $\mu = 0$, thus $\Gamma = \theta_2$. Plots in Figure 2.9 offer a compact way to examine the consequences of collisions with similar layout.

Given the relative speed of approximately 4.5 m/s, Figure 2.9 shows that the post-impact yaw rate of the target vehicle can exceed 100°/s when the incidence angle is just 30°. Overall, the post-impact yaw rate and roll rate are much more sensitive to incidence angle than to collision offset. Similar contour plots can also be plotted for collisions of other configurations, such as side impact and frontal impact. These plots offer an efficient and a reasonably accurate way to examine the consequences of a matrix of light collisions.

In summary, in this section a collision problem is first solved in a full-feature vehicle dynamics software, and the computation results are used to evaluate the accuracy of other simplified approaches. The approach proposed in this study is based on a 4-DOF vehicle model and accounts for impact forces and tire forces simultaneously. Computation results confirm improved accuracy in the predicted post-impact vehicle states, especially translational velocities and roll rate.

2.7 Collision Modeling Applied to PIT Maneuvers

Vehicle collisions do not occur just as accidents. Sometimes vehicle impacts are generated on purpose. The Precision Immobilization Technique (PIT) is a maneuver frequently used by the law enforcement to terminate a hazardous vehicle pursuit situation. The maneuver is performed by intentionally nudging the pursued vehicle sideways to create large yaw motion that renders the pursued vehicle out of control. This section investigates the behavior of vehicles involved in this maneuver, develops dynamics models for the pre-impact and in-impact stages. Computation results can provide guidelines for the effective execution of the maneuver.

2.7.1 Introduction to the PIT Maneuver

Motor vehicle pursuit is a high-risk activity for the law enforcement to undertake. Every year in the United States, hundreds of persons (including police officers, fleeing suspects, and innocent passers-by) are killed or injured during the course of pursuits [55]. Pursuit-related accidents, injuries and fatalities impose tremendous psychological stress on officers. In an effort to reduce the risks inherent in motor vehicle pursuits, the Precision Immobilization Technique (PIT, also known as Pursuit Intervention Technique) [56] is judiciously used by the police to avert a prolonged vehicle chase in a safe manner. In a PIT maneuver, the police vehicle purposely strikes the fleeing vehicle at a certain location, which throws the vehicle into an abrupt spin, and puts a swift end to a high-speed pursuit (see Figure 2.10, screen captures from [57]).

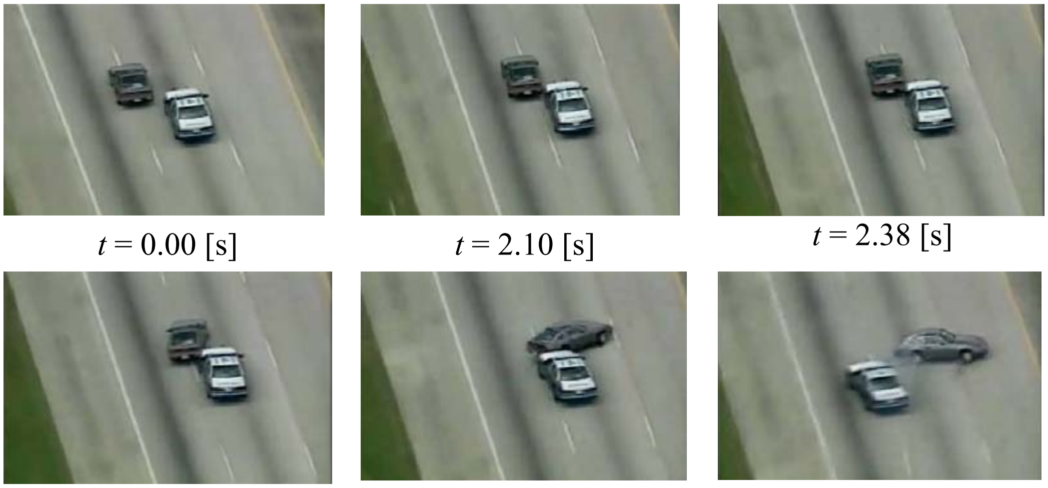

t = 0.00 [s]
t = 2.10 [s]
t = 2.38 [s]
t = 2.80 [s]
t = 3.27 [s]
t = 3.58 [s]

Figure 2.10: A PIT maneuver in action

The execution of PIT requires proper training, planning, choice of site, and careful timing. Under high stress, the police officers must not only choose the best tactics to put the pursued vehicle out of action, but also minimize its safety impact on the surrounding traffic, themselves, and even the suspect. In the court case Scott v. Harris [58], decided by the U.S. Supreme Court in 2007, it was ruled that “a police officer’s attempt to terminate a dangerous high-speed car chase that threatens the lives of innocent bystanders does not violate the Fourth Amendment, even when it places the fleeing motorist at risk of serious injury or death”. This court decision provides favorable judicial support for the law enforcement to use controlled impact (including PIT) against fleeing violators.

Because of the similarities between PIT collisions and some lane change/merge accidents, the modeling approach in previous sections is applied to the analysis of PIT maneuver. Collision models for the vehicles involved in a PIT maneuver are developed, which provides insight into the improvement of PIT maneuver effectiveness [28].

2.7.2 Modeling of Vehicle Dynamics in a PIT Maneuver

As illustrated in Figure 2.11, the pursuing vehicle (pursuer) first adjusts its longitudinal position relative to the pursued vehicle (target), so that the portion of the pursuing vehicle forward of the front axle is aligned with the portion of the pursued vehicle behind the rear axle. The pursuer then maintains a limited lateral clearance from the target's rear fender. When the opportunity comes to initiate intervention maneuver, the pursuer steers sharply towards the target vehicle, develops a pre-impact yaw rate until the two vehicles collide. This sudden steering imparts an impulsive force to the pursued vehicle, and compels it to spin out if the maneuver succeeds.

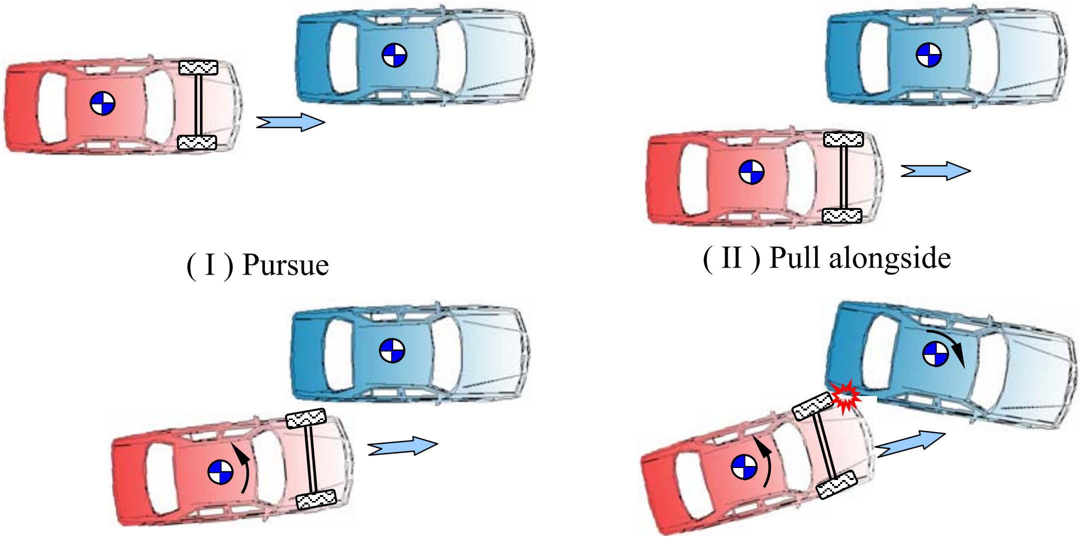

Figure 2.11: Stages of a PIT maneuver

Given road adhesion conditions and forward speed, the pursuer should properly adjust two operation variables to maximize the effect of collision: steering wheel angular velocity and initial lateral clearance. For simplicity, the steering action of the pursuer is modeled with a ramp input below, where the steering wheel turning rate is k_δ, and $t = 0$ denotes the instant of steering initiation.

$$\delta_{SW}(t) = k_\delta \cdot t \tag{2.25}$$

The initial lateral clearance (ΔY) affects the development of the pre-impact states of the pursuer. Given the vehicle's half-width (HW), the angle between vehicle centerline and the front fender (ξ), the lateral displacement (Y_{CG}), as well as the heading angle (ψ), their geometric relationship is depicted in Figure 2.12, in which the struck side of the target vehicle is represented by a wall. Accordingly, the clearance between the pursuer and the target (y_{remain}) is given by

$$y_{\text{remain}} = \Delta Y + \text{HW} - Y_{CG} - d\sin(\psi + \xi) \tag{2.26}$$

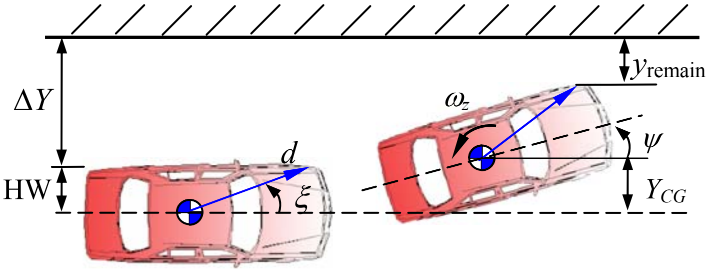

Figure 2.12: Determination of the collision instant

Collision occurs at the instant when y_{remain} drops to zero. The vehicle dynamic responses to the ramp steering input can be approximated by using a standard 2-DOF bicycle model, or computed from a nonlinear model of higher complexity, such as in the CarSim software. Unlike typical circumstances encountered in the studies on vehicle passive safety, usually no substantial structural deformation occurs in a PIT maneuver. Therefore, the emphasis is on the characterization of vehicle kinematic changes due to collisions, and the previously developed model for light impacts is applied to the PIT scenario.

The purpose of a PIT maneuver is to compel the target vehicle to "fishtail" so that the fleeing suspect cannot recover. One straightforward index of the severity of a PIT maneuver is the post-impact yaw rate of the pursued vehicle (Ω_{1z}). The models of pre-impact steering and vehicle collision developed in previous sections can be applied to investigate the influences of operating variables (e.g., initial lateral clearance, steering wheel rate, and forward speed) and parameters (e.g., coefficient of restitution and road adhesion coefficient) on Ω_{1z}.

Table 2.3: Vehicle parameters for "Big Sedan" model in CarSim

Parameter	Description	Value	Unit
m_R	Rolling mass	1527	kg
m_{NR}	Non-rolling mass	180	kg
a, b	Distance from axles to vehicle CG	1.033, 1.657	m
h_{CG}	CG height above the ground	0.54	m
h	Distance from sprung mass CG to the roll axis	0.40	m
I_{zz}	Vehicle yaw moment of inertia about z axis	3200	kg·m^2
I_{xz}	Sprung mass product of inertia about roll and yaw axes	20	kg·m^2
I_{xxs}	Sprung mass roll moment of inertia about the roll axis	850	kg·m^2
K_s	Total suspension roll stiffness	70160	N·m/rad
D_s	Total suspension roll damping	6500	N·m·s/rad

C_f	Front axle cornering stiffness	137130	N/rad
C_r	Rear axle cornering stiffness	117670	N/rad

The parameters and operating conditions for the simulation are specified as follows. The two colliding vehicles are assumed to have the same vehicle parameters summarized in Table 2.3, which are extracted from the "big sedan" nonlinear model in CarSim software. In this section, unless otherwise specified, remaining essential parameters are fixed at their nominal values: forward speed (v_{1x} = 40 mph or 17.88 m/s), initial lateral clearance (ΔY = 0.8 m), steering wheel rate (k_δ = 260 deg/s), coefficient of restitution (e = 0.45), road adhesion coefficient (μ_R = 0.8), and coefficient of tangential interaction (μ = 0.12). Furthermore, the collision locations on vehicle bodies are assumed on the front fender (x_2 = 0.8 m ahead of front axle) and the rear fender (x_1 = 0.9 m behind rear axle).

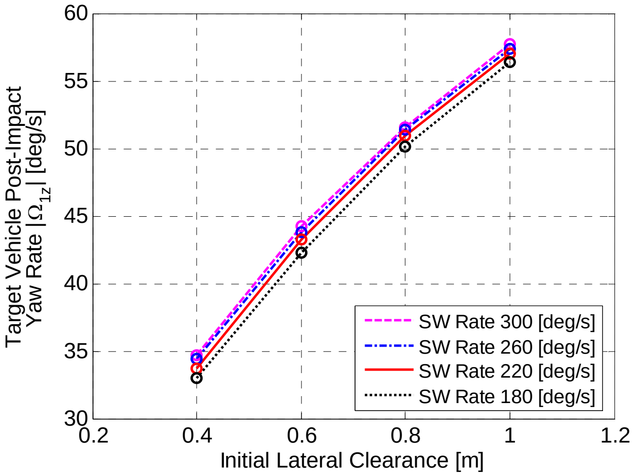

Figure 2.13: Influences of initial lateral clearance and steering rate on PIT's effectiveness

Figure 2.13 shows the influences of the initial lateral clearance and the steering wheel rate on the post-impact yaw rate of the target vehicle, with four levels in each dimension. The figure indicates that other things being equal (e may decline with increasing relative velocity in actual situations), a realistically large initial lateral clearance is favorable for the PIT maneuver. The reason arises from the fact that given more lateral margin, the pursuer can develop a higher pre-impact yaw rate, and through the collision, more angular momentum will be transmitted to the target vehicle. Obviously, this initial lateral clearance has to be technically feasible to perform a PIT maneuver. In addition, a higher steering angular velocity leads to more effective results, but the benefits are marginal when the steering velocity is already sufficiently high.

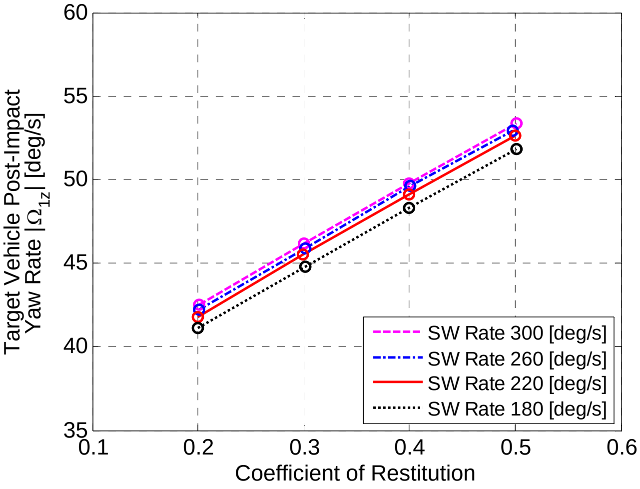

Figure 2.14: Influences of coeff. of restitution and steering rate on PIT's effectiveness

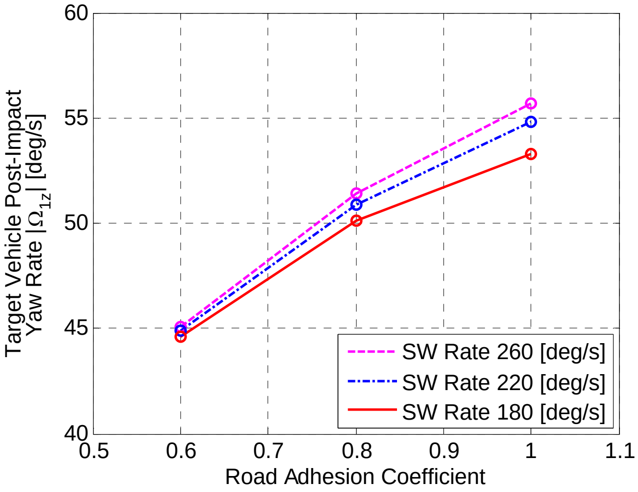

Figure 2.15: Influences of road adhesion and steering rate on PIT's effectiveness

The influences of the coefficient of restitution and the steering wheel rate on the post-impact yaw rate of the target are shown in Figure 2.14. The coefficient of restitution has a strong influence on the PIT results: a higher restitution indicates less energy lost in the collision and more energy imparted to the target, hence more substantial post-impact yaw motions. However, this is not a parameter that can be directly adjusted by the pursuer. It depends on body materials, surface geometry, relative velocities, among other factors. It is preferred that the striking area of the pursuing vehicle is composed of less deformable material and structure. In addition, the influence of road adhesion condition is illustrated in Figure 2.15. Other things being equal, it is shown that roads with better adhesion conditions are conducive to the execution of a PIT maneuver.

2.8 Summary

Vehicle collision problems have been studied in diverse disciplines. The focus of this study is on the characterization of changes in vehicle kinematic states due to light impacts, including translational velocities, yaw rate, and roll rate. The proposed vehicle impact model extends the traditional momentum-conservation approach by incorporating tire forces and sprung mass roll motion. Numerical results demonstrate improved accuracy in predicting post-impact vehicle states. The proposed approach provides an efficient and reasonably accurate way to characterize vehicle motions immediately after an impact. The developed collision model is useful for the prediction of post-impact vehicle motions and the development of enhanced vehicle safety systems. The computation results from this approach sets the initial conditions for the post-impact stability control problem.

As an application, the modeling approach is used in the analysis of the PIT maneuver, a pursuit-ending approach used by the law enforcement. The influencing factors for the execution of the maneuver are explored. It is demonstrated with simulations that a reasonably large lateral clearance and sufficiently fast pre-impact steering action are in favor of an effective PIT maneuver. In addition, the influences of road adhesion and the coefficient of restitution are also revealed with numerical examples.

Chapter 3

Crash Sensing and Validation

3.1 Introduction to Crash Sensing

Before the active control system can do anything to stabilize the vehicle after a crash, the crash has to be detected with vehicle sensors. The topic of crash sensing is a critical issue in the deployment decision of air bags [59, 60]. In order to make judgment on whether and when to inflate the air bag, certain physical variables (such as accelerations and pressures) are constantly monitored and processed. An on-board processor receives vehicle deceleration and other measured signals. The raw signals are first sampled at a certain frequency and filtered through a low-pass filter. Typically, if the filtered deceleration signal exceeds a certain threshold, a crash discrimination algorithm is called upon to decide whether and when to fire air bags.

The key of crash sensing consists in the decision-making part inside the microprocessor of the restraint control system. According to Chan [61], a crash sensing algorithm should meet the following characteristics:

(1) Discriminative: able to reliably differentiate the circumstances of deployment and non-deployment. False alarms are not only annoying to users, but also present great potential hazards.

(2) Predictive: able to assess crash severity at an early stage of a crash, rather than wait until the crash is fully developed. An earlier decision often results in earlier intervention of safety systems and less adverse consequences.

(3) Real-time: feasible to be executed sufficiently fast. The crash sensing, signal processing, and decision-making process should not be computationally intensive. The whole process should react instantaneously upon the received signal in a limited window.

The characteristics of crash data are dependent on many factors, such as crash type, vehicle type, relative velocity, relative weights, and so on. Among them, the most dominating factors are the vehicle structural properties and the manner of collision. Potential variables that can be directly measured for crash sensing include acceleration, pressure, acoustic levels, and stress propagation. Some sensors rely on the direct measurement of physical variables, such as accelerometers for frontal collisions and pressure sensors for side impacts [62]. Others derive information from the measured signals with the help of digital signal processing. The usage of acceleration signal is common among electronic crash sensors, in which filtering, differentiation, and integration schemes are performed within on-board electronic circuitry.

In the event of a crash, the on-board computer processes the sampled variables and decides whether and when air bags should be deployed. Inside the crash sensing algorithms, metrics indicating the severity of a crash are evaluated on the basis of measured and derived variables. Then the metrics are compared with their thresholds, which are calibrated for targeted applications. If the metrics rise beyond their thresholds, a flag will be triggered to fire the inflators inside the air bag assembly.

For the deployment of frontal air bags, the suggested metrics include [63]:

(1) Crash-force-related metrics, such as the change of deceleration (jerk) and the summation of the absolute value of deceleration change;

(2) Crash-energy-related metrics, such as kinetic energy per unit mass, change of velocity, and the summation of the deceleration squared;

(3) Combined metrics, such as power per unit mass and power rate per unit mass.

A number of crash sensing algorithms have been developed with the aid of these metrics. The essential logic and reasoning of some algorithms are briefly outlined and tabulated in [61]. The study of these algorithms targeted for the deployment of frontal air bags provides much insight into the crash sensing design for PISC purposes.

3.2 Crash Sensing Criteria for PISC System

Despite apparently similar functions of the crash sensing in air bag deployment and PISC activation, significant differences exist for the two applications.

First of all, the majority of crash sensing algorithms for air bags rely on vehicle longitudinal acceleration and its derivatives, whereas vehicle lateral acceleration (or lateral velocity) and yaw rate are of interest to post-impact stability control. Secondly, the decision to inflate the air bag is not reversible. Once the inflation command is given, there is no turning back, even if it turns out to be a false alarm. However, in the case of PISC, vehicle states are still subject to monitoring after the activation. If it is later determined to be a false alarm caused by noises, applied braking pressure can be released immediately sometimes without drivers' awareness, thus the operation of PISC is more flexible. Finally, air bags are designed to cushion vehicle occupants in relatively severe frontal and side impacts, whereas PISC intervenes even when the crash is mild (but enough to cause substantial lateral velocity and yaw rate).

For this study, the crash sensing criteria are structured as follows. Suppose through sampling and filtering circuits, measured signals are digitized into sequences at discrete intervals (a sampling time of 0.01 s is assumed). Yaw rate (ω_z) and lateral acceleration (a_y) signals are chosen for the decision-making of PISC activation. As soon as three continuous large inter-sample changes in yaw rate and lateral acceleration are registered, whose changes are beyond the range of drivers' manual operation, it is determined that the vehicle is subject to intense yaw and lateral motion, and warrants the intervention of the PISC system. In pseudo-code, the PISC activation criteria can be formulated as:

```
IF { $\left|\omega_z(j)-\omega_z(j-1)\right| \ge \Delta\omega_z$ AND
    $\left|\omega_z(j-1)-\omega_z(j-2)\right| \ge \Delta\omega_z$ AND
    $\left|\omega_z(j-2)-\omega_z(j-3)\right| \ge \Delta\omega_z$ AND
    $\mathrm{sgn}\left[\omega_z(j)-\omega_z(j-1)\right]=\mathrm{sgn}\left[\omega_z(j-1)-\omega_z(j-2)\right]=\mathrm{sgn}\left[\omega_z(j-2)-\omega_z(j-3)\right]$ }
AND
  { $\left|a_y(j)-a_y(j-1)\right| \ge \Delta a_y$ AND
```

$$\left|a_y(j-1)-a_y(j-2)\right| \geq \Delta a_y \text{ AND}$$

$$\left|a_y(j-2)-a_y(j-3)\right| \geq \Delta a_y \text{ AND}$$

$$\operatorname{sgn}\left[a_y(j)-a_y(j-1)\right]=\operatorname{sgn}\left[a_y(j-1)-a_y(j-2)\right]=\operatorname{sgn}\left[a_y(j-2)-a_y(j-3)\right] \}$$

THEN {Activate PISC}

The sensing thresholds for the gradients of yaw rate and lateral acceleration are $\Delta\omega_z$ = 3 deg/s and Δa_y = 0.1 g between samples, respectively, and the crash sensing results are shown in Figure 3.1. The simulated crash scenarios are as follows. The pre-impact vehicle positions are similar to what is depicted in Figure 2.7. The impact location is assumed to be at the bumper centers of both vehicles. Both vehicles are of the "Baseline Big SUV" configuration with parameters shown in Table 2.1. Before the crash, the target vehicle is traveling straight at 29 m/s, whereas the incidence angle (θ_2) and the pre-impact velocity (v_{2x}) of the bullet vehicle vary between 15 and 30 degree, as well as 32 and 35 m/s, respectively. The activation decisions in response to the crashes are show in the left subplot of Figure 3.1, and the crash consequences, in terms of post-impact yaw rate of the target vehicle, are presented in the right subplot.

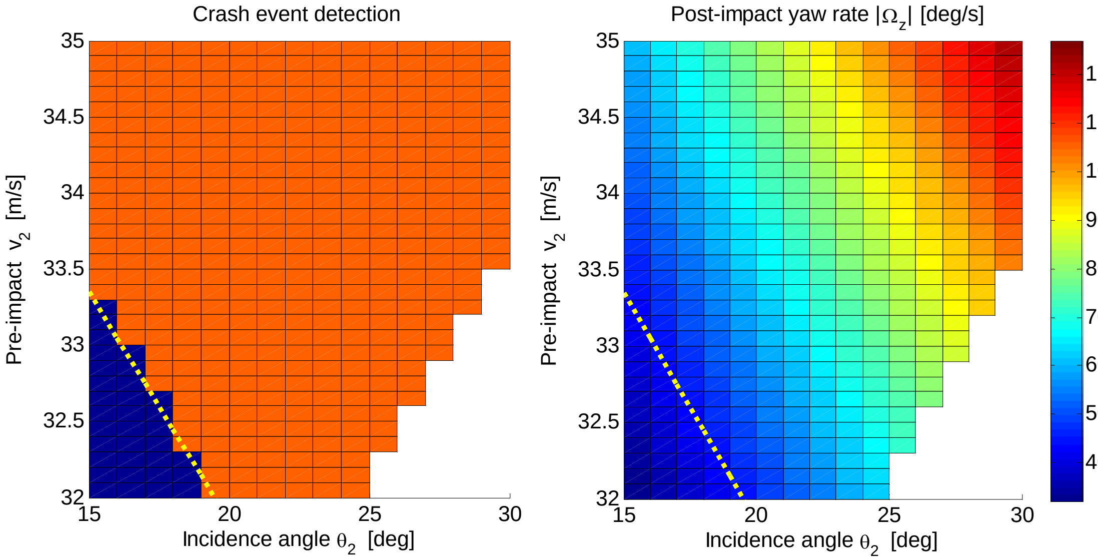

Figure 3.1: Crash sensing results in a matrix of angled rear-end crashes

In the left subplot, the light color denotes the region where PISC is commanded to activate, and the dark color denotes the region where the crash sensing criteria are not met. A dotted line demarcates the two regions approximately, and it is copied onto the right subplot and roughly corresponds to a post-impact yaw rate of 45 deg/s. For practical applications, the threshold settings require further refinement to ensure reliability and robustness against sensor noises.

The fulfillment of the criteria indicates that a possible crash event is detected. However, to verify that this cannot be a false alarm, further corroboration work is indispensable, which will be discussed in the next section.

3.3 Crash Impulse Estimation and Validation

The crash sensing criteria proposed in the previous section ensures that an activation flag will be raised if a large gradient in yaw rate and lateral acceleration is picked up by the sensing algorithm. However, in practice, a significant change in successive samples of yaw rate or lateral acceleration does not necessarily lead to the conclusion that a crash is occurring, since this event may also be caused by sensor defects or noises. In order to eliminate the possibility of improper PISC activation, the apparent crash event needs to be validated by continuously monitoring key kinematic variables.

The general steps of the crash sensing and validation procedure is envisioned as in Figure 3.2. Key vehicle kinematic states are continuously sampled or estimated (in the case of v_y). The first diamond-shaped decision block in Figure 3.2 represents the crash sensing criteria used in Section 3.2. If satisfied, a possible crash event is detected and an activation flag is given to PISC. In order to validate that it is really a crash rather than an accidental aberration in sensors, the onset, severity, as well as location of the impulse need to be estimated. The estimated collision impulse will be used to predict future vehicle responses by extrapolation. If the prediction agrees with the actual measurement afterwards (represented by the second diamond-shaped block), the crash event is deemed valid and the PISC system stays in operation. Otherwise, it is determined to be a false alarm and the PISC will be de-activated. Since the prediction horizon in this case is intended to be of an extremely short duration (e.g., 50 ms or five sampling intervals), false activation of PISC will not result in substantial undesired vehicle motions.

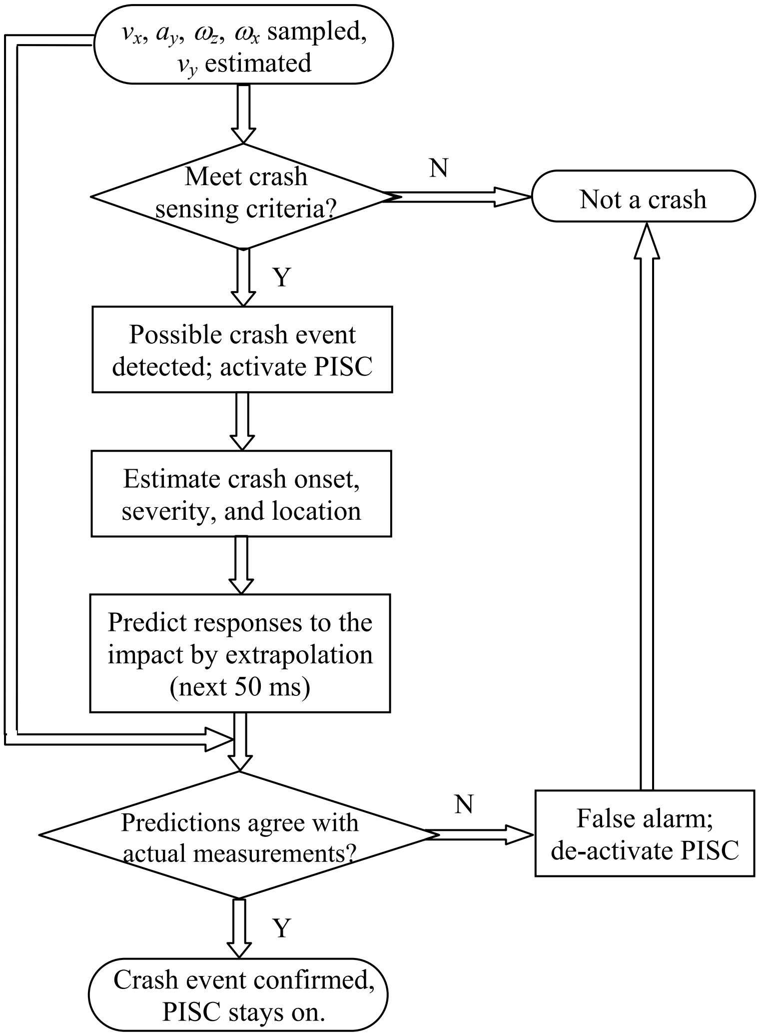

Figure 3.2: Flow chart of the crash sensing and validation procedure

One critical step in the procedure above is to estimate the magnitude and the location of the collision impulse, given accessible vehicle states and a limited set of nominal vehicle parameters. In this study, a model-based estimation scheme is applied to infer the components of the impulse (P_x, P_y) and its location (x_A, y_A). Equations (2.14) - (2.16) in Section 2.4 provide the computational basis and are regrouped below. If the slip angles of front/rear axles become so large that tire lateral forces reach adhesion limit, corresponding terms will be replaced.

$$P_x = M_1 \cdot \left(V_{1x} - v_{1x}\right) - M_1 \frac{\Delta t}{2}\left(V_{1y}\Omega_{1z} + v_{1y}\omega_{1z}\right) \qquad (3.1.)$$

$$P_y = M_1 \cdot \left(V_{1y} - v_{1y}\right) + M_1 \frac{\Delta \mathrm{t}}{2}\left(V_{1x}\Omega_{1z} + v_{1x}\omega_{1z}\right) - m_{R1}h_1 \cdot \left(\Omega_{1x} - \omega_{1x}\right) + \frac{\Delta \mathrm{t}}{2} C_{f1}\left(\frac{V_{1y} + a_1\Omega_{1z}}{V_{1x}} - \frac{v_{1y} + a_1\omega_{1z}}{v_{1x}}\right) + \frac{\Delta \mathrm{t}}{2} C_{r1}\left(\frac{V_{1y} - b_1\Omega_{1z}}{V_{1x}} - \frac{v_{1y} - b_1\omega_{1z}}{v_{1x}}\right) \tag{3.2.}$$

$$P_y x_A - P_x y_A = I_{zz1}\left(\Omega_{1z} - \omega_{1z}\right) + I_{xz1}\left(\Omega_{1x} - \omega_{1x}\right) + \frac{\Delta \mathrm{t}}{2} a_1 C_{f1}\left(\frac{V_{1y} + a_1\Omega_{1z}}{V_{1x}} - \frac{v_{1y} + a_1\omega_{1z}}{v_{1x}}\right) - \frac{\Delta \mathrm{t}}{2} b_1 C_{r1}\left(\frac{V_{1y} - b_1\Omega_{1z}}{V_{1x}} - \frac{v_{1y} - b_1\omega_{1z}}{v_{1x}}\right) \tag{3.3.}$$

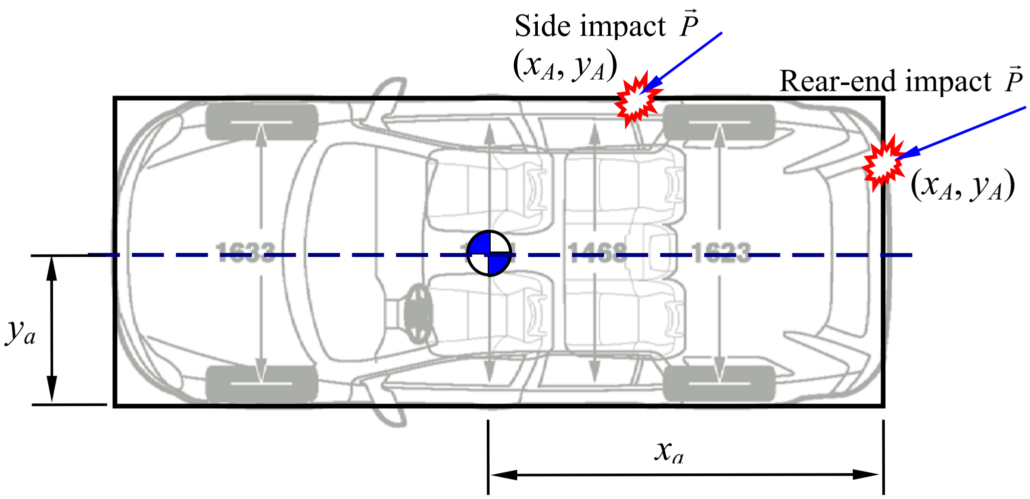

Figure 3.3: Impact locations on vehicle periphery in light collisions

Given vehicle states and parameters on the right hand side of Eqs. (3.1.)-(3.3.), the remaining obstacle is how to solve for four unknowns with only three equations. Actually a pivotal relationship is hidden in the possible impact locations as shown in Figure 3.3. Since the target of this investigation is light collisions without substantial vehicle dimensional changes, the location of the impact is assumed to fall on the vehicle periphery highlighted by the solid rectangle. Two nominal vehicle dimensions are indicated in Figure 3.3 as well: x_a for the distance between CG and the rear bumper, and y_a for half vehicle width. In the case of either a side impact or a rear-end impact, the impact location is restricted on a straight line, and cannot be an arbitrary position inside the vehicle. Consequently, when solving Eq. (3.3.) for x_A and y_A, two cases (side and rear-end impact assumptions) will be dealt with simultaneously. Only the geometrically realistic answers will be accepted. For instance, if a rear-end impact occurs, x_A is assumed to be equal to x_a, and the obtained y_A should fall into a reasonable range, such as [-1.0, 1.0] meter. If not true (e.g. calculated y_A = 1.9 m), the original assumption of a rear-end impact is probably wrong. The same reasoning applies to the case of a side impact.

At each sampling time, after (P_x, P_y) and (x_A, y_A) are estimated, predictions of (P_x, P_y) at a future time step can be made. A linear extrapolation will be used, because impulses are simply time integration of collision forces, and during the brief interval of an on-going crash, impulses are monotonically changing values. A short prediction horizon (e.g. 50 ms) will be employed. Based on the difference between the estimated current impulses and the predicted impulses, the magnitude of collision forces within the short prediction horizon can be derived. Then the four-DOF vehicle dynamics model presented in Section 2.3 can be used to make projections on vehicle kinematic states at the end of prediction window, which will be compared with measurements afterwards to check their agreement. If their trends are consistent, the previously detected crash event is validated and the alarm is true positive, PISC should stay on.

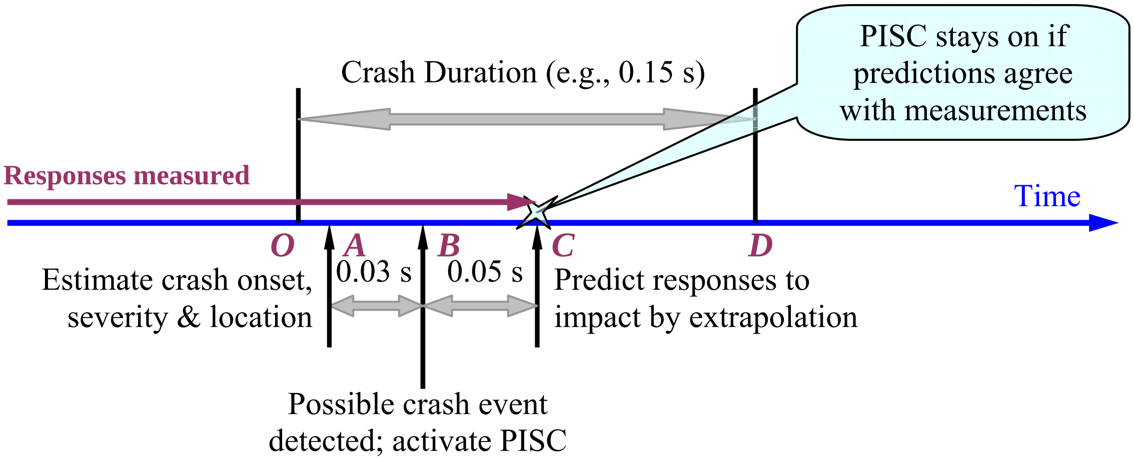

Figure 3.4: Temporal representation of the crash validation steps

Figure 3.4 is an alternative temporal representation of the flow chart in Figure 3.2. The actual duration of the crash is from “O” to “D.” This crash is presumably detected at “B” by meeting the criteria in Section 3.2. The estimated crash onset is positioned at “A” since three sampling steps are used in the sensing criteria. Then the crash severity and location as well as the predicted vehicle responses at a future time “C” are computed, which is five samples downstream from the current time step. When the actual time course reaches point “C,” measured yaw rate and lateral velocity are compared with their predicted versions. If there is an agreement, the crash event detected at "B" is validated. Otherwise, PISC should be de-activated.

3.4 Simulation Results for Crash Sensing

The effectiveness of the complete crash sensing and validation procedure is evaluated with simulation studies. The simulated collision has the same settings as the rear-end impact illustrated in Figure 2.7 of Section 2.6. The impact location of the target vehicle is 0.1 m to the left of its rear bumper center. The big SUV model has nominal dimensions x_a = -2.65 m and y_a = 0.88 m.

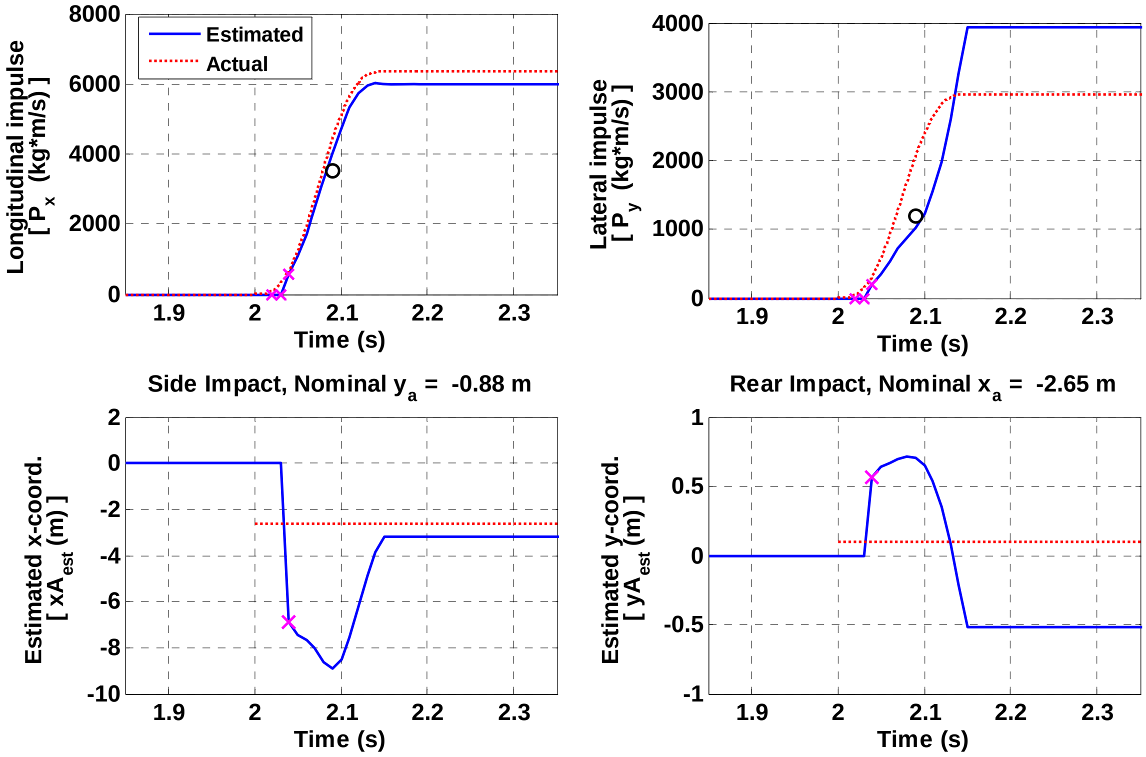

Figure 3.5: Estimation results of impulse magnitude and location

Figure 3.5 presents the results of crash impulse estimation for the target vehicle. Vehicle responses during the crash can be found in Figure 2.8. The crash starts at 2.0 s and lasts 0.15 s. However, this crash is not sensed until 2.04 s, which is marked by the crosses in Figure 3.5. Then the onset of the crash is estimated at 2.01 s and the estimation of (P_x, P_y) and (x_A, y_A) is set in motion (represented by solid lines). Through linear extrapolation, the predicted P_x and P_y at the future time instant 2.09 s can be obtained (marked with empty dots). The prediction values are reasonably close to the actual values on the dotted lines. As far as the estimation of x_A and y_A is concerned, the side-impact-assumption will lead to an unlikely value of $x_A \approx$ -7.0 m, which is impossible for an average SUV. Therefore, a rear-end impact is concluded and the estimate of y_A is approximately 0.55 m.

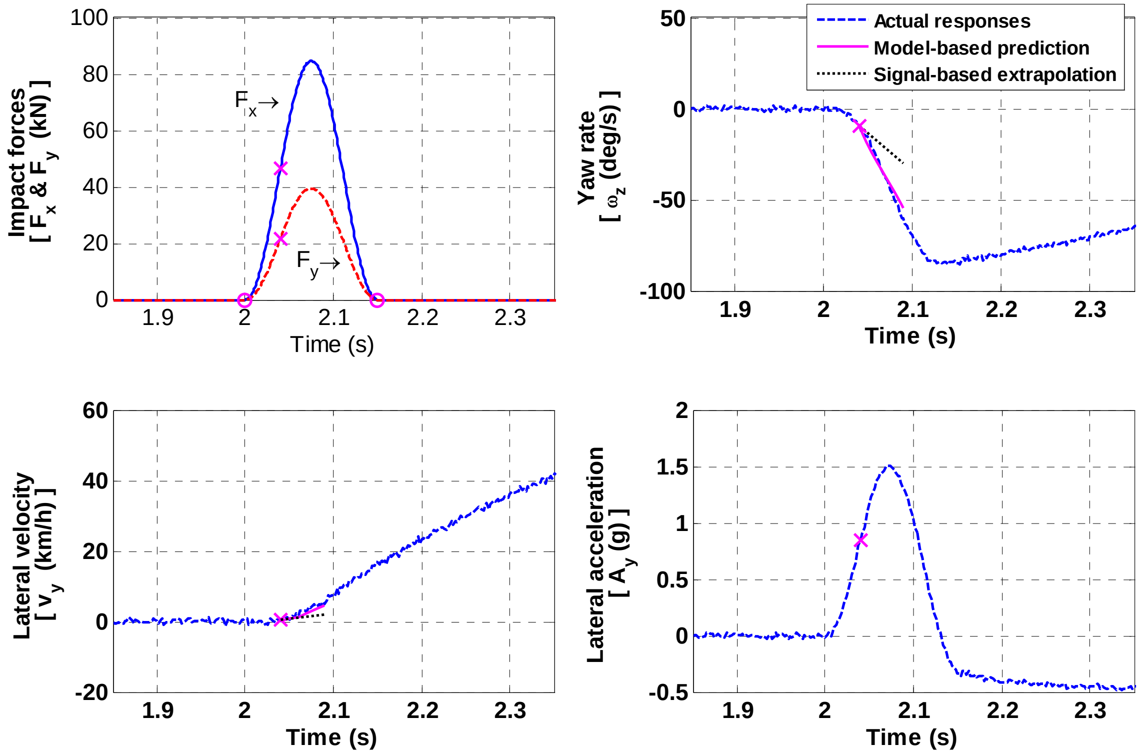

Figure 3.6: Comparison of actual and predicted vehicle responses

Figure 3.6 contrasts the actual vehicle responses with the model-based predictions and a signal-based extrapolation. Since the lateral acceleration is directly related to the external forces applied and the impact forces only last a fraction of a second, the lateral acceleration plot shows an impulsive pattern. In contrast, the yaw rate and the lateral velocity are the results of integrated linear and angular accelerations, so they show an accumulative pattern, which makes them amenable to extrapolations.

The instant when the crash event (2.04 s) is detected is marked with crosses in all subplots of Figure 3.6. Measured vehicle responses are shown in dashed lines. The measurements are corrupted with Gaussian noises, with standard deviations of 0.1 m/s^2

for the accelerometer and 0.5 deg/s for the yaw rate gyro sensor. The model-based predictions of yaw rate and lateral velocity, which are computed with the predicted impulse and a nominal four-DOF vehicle model, are plotted with solid lines. The signal-based extrapolations are simply the linearly extrapolated results from yaw rate and lateral velocity at three latest sampling times. It is evident that the model-based prediction outperforms the signal-based extrapolation, and the trend of the former approach is consistent with that of the actual measurements. For instance, the predicted yaw rate at the end of the horizon is -54.3 deg/s, whereas the actual yaw rate at this instant is -60.3 deg/s. It should be kept in mind this 10% discrepancy is based on a series of approximations and estimations. In particular, it is unlikely that this increasing trend is purely caused by sensor malfunction or noises. Therefore, the detected crash is positively confirmed.

3.5 Summary

For the post-impact stability control system to operate, it has to be activated at the proper moment and should not be triggered by faulty measurements or sensor noises. A crash sensing and validation scheme is proposed in this chapter to address this issue.

The crash sensing criteria are based on the monitoring of continuous large variations in sampled yaw rate or lateral acceleration. If the criteria are met, the PISC will be activated but the sensed crash event still awaits further verification. The vehicle dynamics model formulated in Chapter 2 is modified to make estimations on the impact magnitude and location, which are in turn used to predict vehicle responses at future time steps. Finally the predicted vehicle kinematic states are compared with actual measurements to check consistency.

The model-based impact estimation and response prediction approach ensures that PISC will not be active for a prolonged time simply due to sensor malfunctions or noises. With the activation part of the PISC system being resolved, the control part of the system will be discussed in detail in the next chapter.

Chapter 4

Controller Algorithms for the PISC System

4.1 Overview

After the consequences of crashes have been estimated and the crash sensing and validation schemes have been developed, the post-impact control problem is approached as a regulation problem to attenuate the significant initial states to much smaller levels.

Before formulating the post-impact control problem, the following general assumptions are made. First of all, it is assumed that the entire event occurs on a straight road, and the two vehicles involved do not come into contact with other vehicles or obstacles. Furthermore, for the proposed post-impact stability control system to function effectively, the braking and steering systems are assumed to function normally despite the collision. Finally, on-board sensors and estimation schemes can still provide quality measurements and estimated variables. Concerns over sensor malfunctions as well as estimation biases are left to future work.

This chapter proposes and verifies the design of a post-impact control system based on differential braking and active steering schemes. The objective of post-impact stability control is to automatically attenuate slip angle, yaw rate, and roll rate as soon as an impact is detected, and to make vehicle motions more manageable if the driver starts to take actions. The development of the controller will be based on a 3-DOF planar vehicle model, and the controller is assumed to have access to necessary vehicle states. Challenges facing the actual implementation of this controller are the estimation of vehicle states, such as slip angles and tire normal forces, and an accurate tire model for coupled longitudinal and lateral forces. Furthermore, the arbitration and coordination among the PISC system operation, existing ESC systems, and the driver's reactions also needs to be addressed.

In order to evaluate the effectiveness of the proposed control system, the following performance variables should be taken into account: forward speed reduction, lateral displacement, and yaw rate/lateral velocity attenuation. A driver’s natural response after a collision may be to slow the vehicle down and stop safely. Obviously, occupants are at elevated risks when the vehicle velocity is higher, especially after directional stability was lost. On the other hand, if the speed reduction is too drastic, the vehicle may run the risk of being rear-ended by trailing vehicles. Therefore, speed reduction after an impact should be managed in a controlled way. Besides velocity, lateral displacement is a major factor in deciding whether the vehicle will be involved in a secondary lane departure accident. It is preferable to constrain vehicle lateral position within its original lane boundaries. However, this constraint could severely limit the feasible range that the PISC system can cope with. For instance, given a typical velocity of 65 mph (29 m/s) on highways and the nominal lane width of 3.65 m, a mild angled rear-end collision such as the one used in Section 2.6 can displace the target vehicle from its own lane within one second. In particular, the control problem is compounded with physical limitations of tires as well as computation and actuation delays. In the discussion below, a post-impact lateral displacement within two-lane width will be accepted. Finally, the heading angle of the vehicle must be limited as well. In general, a diverging heading angle indicates that the yaw rate is not well contained. When the heading angle reaches 90°, the vehicle is perpendicular to the desired travel direction and exposes its flank to approaching traffic. When the peak heading angle is larger than 90°, vehicle stability cannot be recovered simply via selective braking and active steering.

The rest of this chapter is organized as follows. The PISC system has a hierarchical structure, and an upper-level controller for braking and steering commands is derived in Section 4.2, which generates a desired stabilizing yaw moment and a desired front axle steering angle. The implementation of this desired virtual yaw moment by means of differential braking and the allocation of braking forces is addressed in Section 4.3. A lower-level controller for wheel longitudinal slip is discussed in Section 4.4. Then a complete PISC system is built in Simulink and interfaced with the vehicle dynamics model in CarSim. The system architecture, along with PISC system activation and de-activation logic, is detailed in Section 4.5. Section 4.6 provides simulation results to validate the effectiveness of the proposed active safety system in an angled rear-end collision. A comprehensive comparison of control approaches, including full ABS braking, ESC system, and PISC system, is preformed in Section 4.7 in terms of their capability to reject impulsive disturbances and stabilize subsequent vehicle motions. Finally, conclusions and perspectives for the next phase are presented in Section 4.8.

4.2 Derivation of the PISC Controller

The post-impact stability controller is developed on the basis of a planar two-track 3-DOF vehicle model illustrated in Figure 4.1, without the presence of external impact forces. It is straightforward to obtain vehicle equations of motion for longitudinal, lateral, and yaw dynamics.

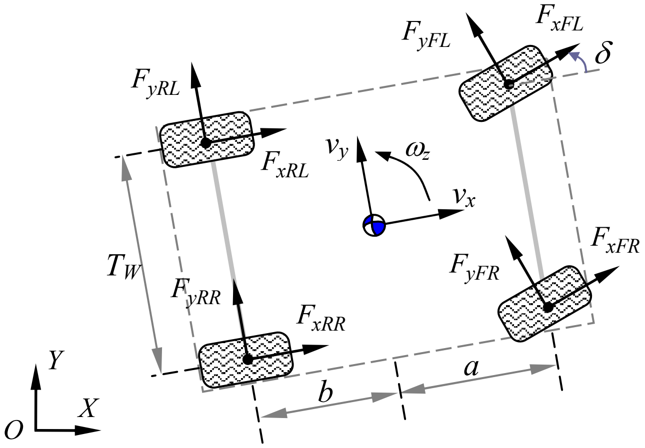

Figure 4.1: A planar view of the 3-DOF vehicle model

$$M \cdot (\dot{v}_x - v_y\omega_z) = \left(F_{xFL} + F_{xFR}\right)\cos\delta - \left(F_{yFL} + F_{yFR}\right)\sin\delta + \left(F_{xRL} + F_{xRR}\right) \tag{4.1}$$

$$M \cdot (\dot{v}_y + v_x\omega_z) = \left(F_{xFL} + F_{xFR}\right)\sin\delta + \left(F_{yFL} + F_{yFR}\right)\cos\delta + \left(F_{yRL} + F_{yRR}\right) \tag{4.2}$$

$$\begin{aligned} I_{zz}\dot{\omega}_z &= a \cdot \left(F_{xFL} + F_{xFR}\right)\sin\delta + a \cdot \left(F_{yFL} + F_{yFR}\right)\cos\delta - b \cdot \left(F_{yRL} + F_{yRR}\right) \\ &\quad + \frac{T_W}{2} \cdot \left[\left(F_{xFR} - F_{xFL}\right)\cos\delta - \left(F_{yFR} - F_{yFL}\right)\sin\delta\right] + \frac{T_W}{2} \cdot \left(F_{xRR} - F_{xRL}\right) \end{aligned} \tag{4.3}$$

If the front steering angle δ is reasonably small, small-angle assumptions apply to the trigonometric functions, and the lateral and yaw dynamics equations of the vehicle are reduced to

$$M \cdot (\dot{v}_y + v_x \omega_z) = \left(F_{xFL} + F_{xFR}\right)\delta + \left(F_{yFL} + F_{yFR} + F_{yRL} + F_{yRR}\right) \tag{4.4}$$

$$\begin{gathered} I_{zz}\dot{\omega}_z = a \cdot \left(F_{yFL} + F_{yFR}\right) - b \cdot \left(F_{yRL} + F_{yRR}\right) + a \cdot \left(F_{xFL} + F_{xFR}\right)\delta + \\ \frac{T_W}{2} \cdot \left[\left(F_{xFR} - F_{xFL}\right) + \left(F_{xRR} - F_{xRL}\right)\right] - \frac{T_W}{2} \cdot \left(F_{yFR} - F_{yFL}\right)\delta \end{gathered} \tag{4.5}$$

When tire slip angles are small (e.g., lower than 7°), tire lateral forces can be related to the cornering stiffness [50] and computed with

$$F_{yf} = F_{yFL} + F_{yFR} = C_f \left(\delta - \frac{v_y + a\omega_z}{v_x} \right) \tag{4.6}$$

$$F_{yr} = F_{yRL} + F_{yRR} = C_r \left(- \frac{v_y - b\omega_z}{v_x} \right) \tag{4.7}$$

The primary objective of the control system is to mitigate intense lateral/yaw and associated roll motions after the impact. Equations (4.4) and (4.5) are used for controller development and the two system states (sideslip velocity and yaw rate) are denoted as

$$\begin{cases} x_1 = v_y \\ x_2 = \omega_z \end{cases} \tag{4.8}$$

Two possible control inputs to the system are the yaw moment realized through differential braking forces and the front steering angle.

$$u_1 = \frac{T_W}{2} \cdot \left(F_{xFR} - F_{xFL}\right) + \frac{T_W}{2} \cdot \left(F_{xRR} - F_{xRL}\right) \tag{4.9}$$

$$u_2 = \delta \tag{4.10}$$

The design of the PISC system controller is based on the multiple sliding surface control approach [64] for its nonlinear nature and tolerance of model uncertainties. Since the control objective is to mitigate post-impact sideslip velocity and yaw rate, a sliding surface is first defined with respect to the lateral velocity.

$$S_1 \triangleq x_1 - x_{1d} \tag{4.11}$$

where the desired lateral velocity $x_{1d} = 0$. To make the surface attractive, one enforces

$$\dot{S}_1 = -k_1 S_1, \tag{4.12}$$

where k_1 is a positive convergence rate. Substitute vehicle lateral dynamics into Eq. (4.12) and one obtains

$$\omega_z = \frac{\left(F_{yFL} + F_{yFR}\right) + \left(F_{yRL} + F_{yRR}\right)}{Mv_x} + \frac{\left(F_{xFL} + F_{xFR}\right)}{Mv_x}\delta + \frac{k_1 v_y}{v_x} \tag{4.13}$$

Replacing the unknowns with their estimated versions yields the yaw rate command (i.e., a synthetic input)

$$\overline{x}_2 = \frac{\left(\hat{F}_{yFL} + \hat{F}_{yFR}\right) + \left(\hat{F}_{yRL} + \hat{F}_{yRR}\right)}{Mv_x} + \frac{\left(\hat{F}_{xFL} + \hat{F}_{xFR}\right)}{Mv_x}\delta + \frac{k_1 v_y}{v_x} \tag{4.14}$$

To avoid directly differentiating tire forces, the yaw rate command $\overline{x}_2$ is filtered by a first-order lag to generate the desired yaw rate x_{2d},

$$\tau \cdot \dot{x}_{2d} + x_{2d} = \overline{x}_2 , \tag{4.15}$$

where the time constant τ is a design parameter.

A second sliding surface is then defined for yaw rate convergence,

$$S_2 \triangleq x_2 - x_{2d} \tag{4.16}$$

Similarly, to make the surface attractive, one imposes

$$\dot{S}_2 = -k_2 S_2 \text{, or } \dot{x}_2 - \dot{x}_{2d} = -k_2\left(x_2 - x_{2d}\right) \tag{4.17}$$

where k_2 is also a positive parameter controlling the convergence rate. The vehicle yaw dynamics can be reformulated as

$$\begin{aligned} \dot{\omega}_z = {} & \frac{a}{I_{zz}} \cdot \left(F_{yFL} + F_{yFR}\right) - \frac{b}{I_{zz}} \cdot \left(F_{yRL} + F_{yRR}\right) + \\ & \frac{1}{I_{zz}} u_1 + \frac{a \cdot \left(F_{xFL} + F_{xFR}\right) - \frac{T_W}{2} \cdot \left(F_{yFR} - F_{yFL}\right)}{I_{zz}} u_2 \end{aligned} \tag{4.18}$$

When tire slip angles are sufficiently small, this formulation can be approximated with

$$\begin{aligned} \dot{\omega}_z = {} & \frac{bC_r - aC_f}{I_{zz} v_x} v_y - \frac{a^2 C_f + b^2 C_r}{I_{zz} v_x} \omega_z + \\ & \frac{1}{I_{zz}} u_1 + \frac{aC_f + a \cdot \left(F_{xFL} + F_{xFR}\right) - \frac{T_W}{2} \cdot \left(F_{yFR} - F_{yFL}\right)}{I_{zz}} u_2 \end{aligned} \tag{4.19}$$

After substitutions, the desired yaw moment and steering angle are given by

$$\begin{aligned} u_{1d} = & -a\cdot\left(\hat{F}_{yFL}+\hat{F}_{yFR}\right)+b\cdot\left(\hat{F}_{yRL}+\hat{F}_{yRR}\right)- \\ & \left[a\cdot\left(\hat{F}_{xFL}+\hat{F}_{xFR}\right)-\frac{T_W}{2}\cdot\left(\hat{F}_{yFR}-\hat{F}_{yFL}\right)\right]u_2+I_{zz}\left[\dot{x}_{2d}-k_2\left(x_2-x_{2d}\right)\right] \end{aligned} \tag{4.20}$$

$$\begin{aligned} u_{2d} = & \frac{I_{zz}}{aC_f+a\cdot\left(\hat{F}_{xFL}+\hat{F}_{xFR}\right)-\frac{T_W}{2}\cdot\left(\hat{F}_{yFR}-\hat{F}_{yFL}\right)}\times \\ & \left[-\left(\frac{bC_r-aC_f}{I_{zz}v_x}v_y-\frac{a^2C_f+b^2C_r}{I_{zz}v_x}\omega_z+\frac{1}{I_{zz}}\hat{u}_1\right)+\dot{x}_{2d}-k_2\left(x_2-x_{2d}\right)\right] \end{aligned} \tag{4.21}$$

The stability analysis of the closed-loop system follows the procedure outlined in Yip's dissertation [65] and detailed procedures can be found in Appendix B.

The control commands in Eqs. (4.20) and (4.21) require measurements of forward speed, yaw rate and current steering angle, as well as the estimation of lateral velocity. A much more challenging requirement is the knowledge of tire longitudinal and lateral forces. In this idealized controller, it is assumed that a reliable estimator of tire forces is readily available. It provides estimated tire forces with excellent accuracy. Therefore, although the developed controller is not yet ready for practical implementation, the design provides performance boundaries that the PISC system can achieve. The development of tire force estimator is presented in Appendix C.

The commands u_{1d} and u_{2d} generated by the PISC controller need to be further translated into actuator signals, in other words, braking pressures at wheel cylinders and steering wheel angle. For active steering angle, a linear relationship exists between the steering wheel angle and the front axle steering angle by ignoring steering compliances,

$$\delta_{SW} = G_{SR}\times\delta \tag{4.22}$$

where G_{SR} is the reduction ratio of the steering gearbox. In addition, a saturation limit is imposed on δ (within ±15°), and a rate limit is imposed on δ_{SW} (< 540°/s).

The realization of the yaw moment command u_{1d} through differential braking forces warrants further discussion, which will be addressed in depth in the next section.

4.3 Strategy of Differential Braking

A differential braking system can apply individual braking pressures at the four wheels, so that the vehicle can be maneuvered even without drivers' steering inputs. Given uniform adhesion and normal loading conditions, a counter-clockwise yaw moment is generated when the braking pressures on the left wheels are higher than those on the right wheels. Conversely, a clockwise yaw moment is generated when the braking pressures on the right wheels are higher than their left counterparts.

The actual yaw moment generated by braking forces is given by Eq. (4.9), which can be substantially different from the command value dictated by Eq. (4.20), because the actual braking forces developed between tires and the ground are heavily influenced by tire normal loads, adhesion conditions, the presence of tire cornering forces, and wheel longitudinal slips. In addition, since there are two actuators in this case (one front and one rear wheel), the differential braking function is actually under-determined. Theoretically, a time-varying problem can be formulated to find the optimal allocation of the braking forces, so that the difference between the command and the actual yaw moment is minimized while subject to tire physical limitations.

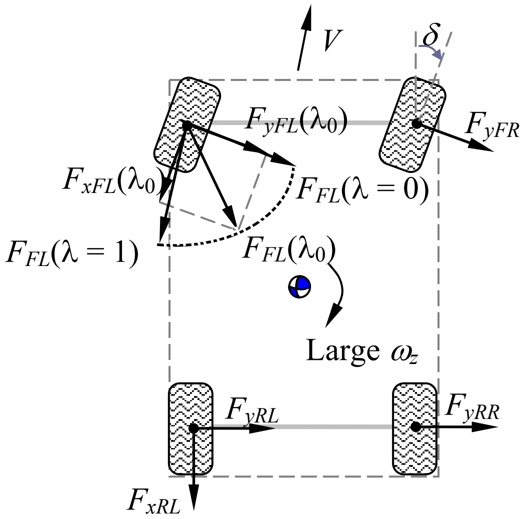

Figure 4.2: The influence of differential braking on the total yaw moment

A closer investigation of the influence of differential braking on the overall yaw moment is illustrated in Figure 4.2. The envisioned scenario is as follows. The vehicle is veering towards the right and has a large instantaneous clockwise yaw rate. In order to attenuate this yaw motion, a counter-clockwise yaw moment is desired. In other words, the outside (in this case, left side) wheels should be braked to create a stabilizing effect. However, different levels of braking may produce vastly different results. Three levels of braking on the front outside wheel are sketched for the front left wheel: $\lambda = 0$, λ_0, and 1, approximately corresponding to no braking, partial braking, and wheel lock-up, respectively. Limited by the tire friction ellipse, in each case the resultant tire force falls on the border of the ellipse. Nevertheless, they generate significantly different effects on the total yaw moment after the resultant forces are decomposed into longitudinal and lateral forces. For the front outside wheel, its lateral force is in favor of further yaw motion and needs to be minimized, whereas its braking force is against the yaw motion and should be maximized. Evidently, the case when $\lambda = 1$ is the optimal situation for the front left wheel in Figure 4.2. As far as the rear outside (in this case, rear left) wheel is concerned, both its braking and cornering forces are conducive to generating a stabilizing yaw moment. In theory, an optimal wheel slip can be resolved at each instant to maximize this yaw moment, as long as the adhesion characteristics and normal load of the tire are well known. Evidently, the computational load and the requirements on modeling accuracy will be higher.

Based on this analysis, instead of solving a time-varying optimization problem, a strategy of brake force allocation is pursued as follows. The braking side depends on the sign of the yaw moment command dictated by Eq. (4.20), with a positive sign corresponding to the left side. Then the particular braking pressures are determined by

$$u_{1d} = \frac{T_W}{2}\left(G_{bF} \cdot P_{bF} + G_{bR} \cdot P_{bR}\right) \tag{4.23}$$

where G_{bF}, G_{bR} are linearized gains from wheel cylinder pressure in bar to braking force in N. The braking pressures on the front and rear axles can either be equal or follow a proportioning rule. In the rest of this work, it is assumed that a fixed 0.35 proportioning ratio exists between them:

$$P_{bR} = 0.35 \times P_{bF} \tag{4.24}$$

If the desired yaw moment u_{1d} is small enough to be well tracked by the actual value in Eq. (4.9), the braking pressures are computed with Eq. (4.23). If the braking pressures requested by u_{1d} are too large, the front outside wheel is allowed to be locked up (λ = 1) as explained before, and the rear outside wheel is subject to a wheel-slip control mode. A desired wheel slip (λ_d = 0.2) is used in this work so that substantial braking and cornering forces are maintained.

This lock-up-and-slip-control strategy can be regarded as a practical solution to the original optimal braking force allocation problem, which otherwise needs to be solved at higher computational cost and is limited by modeling accuracy. This strategy is justified by the analysis above and apt for practical implementation. The wheel-slip control algorithm employed in this work will be covered in the next section.

4.4 Sliding Mode Wheel-Slip Control

Wheel-slip control, especially the antilock braking system (ABS) has evolved from something novel to something normal, and become an integral part of the chassis control system on vehicles nowadays. Typically, ABS adjusts the pressure in brake hydraulic lines to control wheel slip and prevent lock-up. In this way, maximum braking performance can be achieved and steering ability can be maintained. Furthermore, the capability to independently and actively control the longitudinal slip of each wheel provides the necessary actuation for the implementation of other advanced vehicle control systems, such as electronic stability control and roll stability control.

ABS systems have been deployed on vehicles for decades. Various wheel-slip control strategies have been proposed in academia and industry, and successfully implemented on vehicle models of diverse configurations. Some popular ABS control strategies including fuzzy learning/logic controller [66, 67] and sliding mode controller [68, 69, 70] are proposed in the literature. Because wheel-slip control is not the focus of this study, and ABS control algorithms on actual vehicle models are proprietary to automotive companies, a wheel-slip controller designed on the basis of sliding mode control theory is developed in this section. Sliding mode control has been successfully applied to a variety of applications in recent years; the wheel-slip controller to be described next is mainly based on the derivation in Bang *et al*. [70].

A quarter-car model (Figure 4.3) is adequate to illustrate the ABS controller development. The simplified longitudinal dynamics and wheel rotational dynamics are represented by the following equations.

$$F_x = M\dot{V}_x \tag{4.25}$$

$$I_w\dot{\omega} = T_b - F_x \cdot R_w \tag{4.26}$$

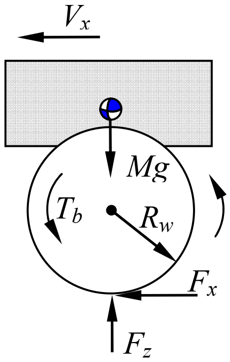

Figure 4.3: A quarter-car model for the derivation of the wheel-slip controller

Tire rolling resistance is ignored in Eq. (4.26), and the torque T_b is the combined effect of traction and braking. During braking, the tire longitudinal wheel slip is defined as

$$\lambda = \frac{V_x - R_w\omega}{V_x} = 1 - \frac{R_w\omega}{V_x}\,. \tag{4.27}$$

Taking the derivative of the wheel slip with respect to time and make proper substitutions, the dynamics of the wheel slip becomes

$$\dot{\lambda} = f - \frac{R_w}{V_x I_w}T_b,\ \text{where}\ f = \frac{(1-\lambda)\dot{V}_x + \left(R_w^2/I_w\right)F_x}{V_x} \tag{4.28}$$

In Eq. (4.28), the term f is a function of vehicle speed, wheel angular velocity, and friction force. If the errors on vehicle velocity and wheel angular velocity from sensors are sufficiently small, the error in estimating f mainly arises from the estimated friction force $\hat{F}_x$. If this estimation error is bounded, the error in the nonlinear function f is constrained by a known quantity $\bar{F}$:

$$\left|f - \hat{f}\right| = \left|\frac{R_w^2}{V_x I_w}\left(F_x - \hat{F}_x\right)\right| \le \bar{F} \tag{4.29}$$

According to the slide mode control theory [71], the total control input is composed of an equivalent control component and a switching control component. The equivalent control component can be interpreted as a control that makes the system states stay on a desired sliding surface, and the switching control component ensures that the trajectory of system states will eventually reach the desired sliding surface.

Given a desired wheel slip λ_d, which can be either a constant or a function of time, the sliding surface (tracking error) is defined as

$$S = \lambda - \lambda_d \tag{4.30}$$

Suppose the system states have already met the sliding conditions, then

$$\dot{S} = 0 \Rightarrow f - \frac{R_w}{V_x I_w} T_b - \dot{\lambda}_d = 0 \tag{4.31}$$

Thus the equivalent control term can be derived:

$$\hat{T}_b = \frac{V_x I_w}{R_w}\left(\hat{f} - \dot{\lambda}_d\right) = \frac{I_w(1-\lambda)\dot{V}_x}{R_w} + R_w \hat{F}_x - \frac{V_x I_w}{R_w}\dot{\lambda}_d \tag{4.32}$$

The role of the switching control is to drive the system states to the sliding surface regardless of uncertainty on the model. With a signum function term being added to $\hat{T}_b$, the total control torque is formulated as

$$T_b = \hat{T}_b + K\,\mathrm{sgn}(S) \tag{4.33}$$

The control gain K must be chosen so that it guarantees the sliding condition. Define a Lyapunov function composed of tracking error,

$$V_{Lyap} = \frac{1}{2}S^2 \tag{4.34}$$

take its derivative, and $\dot{V}_{Lyap}$ is negative definite if $K = \frac{V_x I_w}{R_w}\left(\bar{F} + \eta\right)$. Plug in K and it can be shown that

$$S \cdot \dot{S} = S\left(f - \hat{f}\right) - \frac{R_w}{V_x I_w} K|S| \le -\eta|S| \tag{4.35}$$

where η is a design parameter that determines the convergence rate towards the sliding surface. In order to suppress the chattering problem inherent to the sliding control [71], the signum function is replaced with a saturation function and the desired brake torque becomes

$$T_b = \frac{I_w(1-\lambda)\dot{V}_x}{R_w} + R_w\hat{F}_x - \frac{V_x I_w}{R_w}\dot{\lambda}_d + K \cdot \mathrm{sat}\left(\frac{\lambda - \lambda_d}{\varphi}\right) \tag{4.36}$$

where the boundary layer thickness φ is also a design parameter. For actual implementation, the desired torque has to be converted into a brake pressure command. A straightforward proportional relationship is assumed:

$$P_b = \frac{T_b}{G_b} \tag{4.37}$$

where G_b is the linearized gain from cylinder pressure in bar to brake torque in Nm. The final command of the wheel cylinder pressure will be limited within a realistic range of hydraulic system specifications, for instance, between 0 and 120 bar.

In order to generate realistic braking responses, a hydraulic braking module with practical performance is used. The pressure buildup behavior of the nonlinear braking model can be approximated by a first-order time lag, a time-delay, and a rate limiter.

$$\frac{P_{deliver}}{P_{cmd}} = \frac{e^{-T_d s}}{T_L s + 1}, \; \dot{P}_{deliver} \le \mathrm{RateLim} \tag{4.38}$$

The results of approximation are shown in Figure 4.4. For the front axle, the fitting parameters are $T_d = 0.06$ s, $T_L = 0.12$ s, RateLim = 230 bar/s; for the rear axle, the fitting parameters are $T_d = 0.02$ s, $T_L = 0.05$ s, RateLim = 750 bar/s.

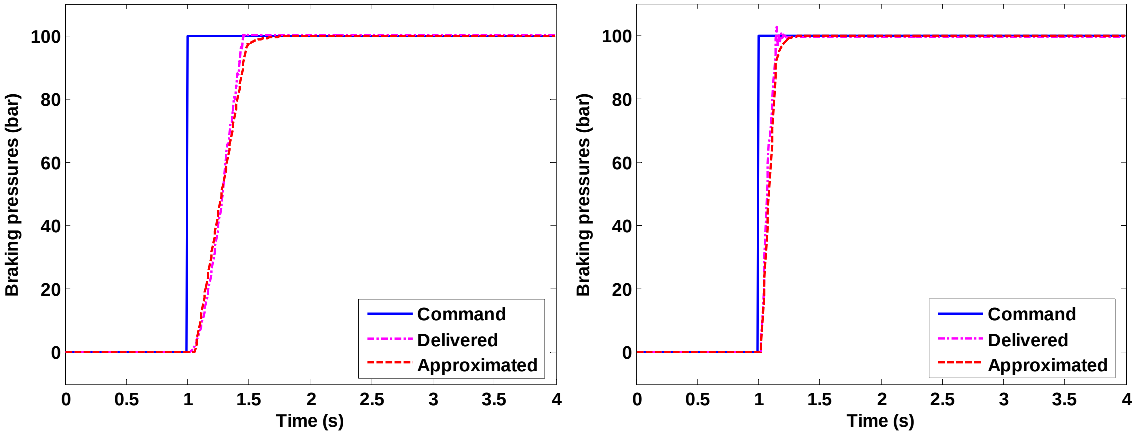

Figure 4.4: Characterization of the hydraulic braking systems for front (left) and rear (right) axles

4.5 Control System Architecture

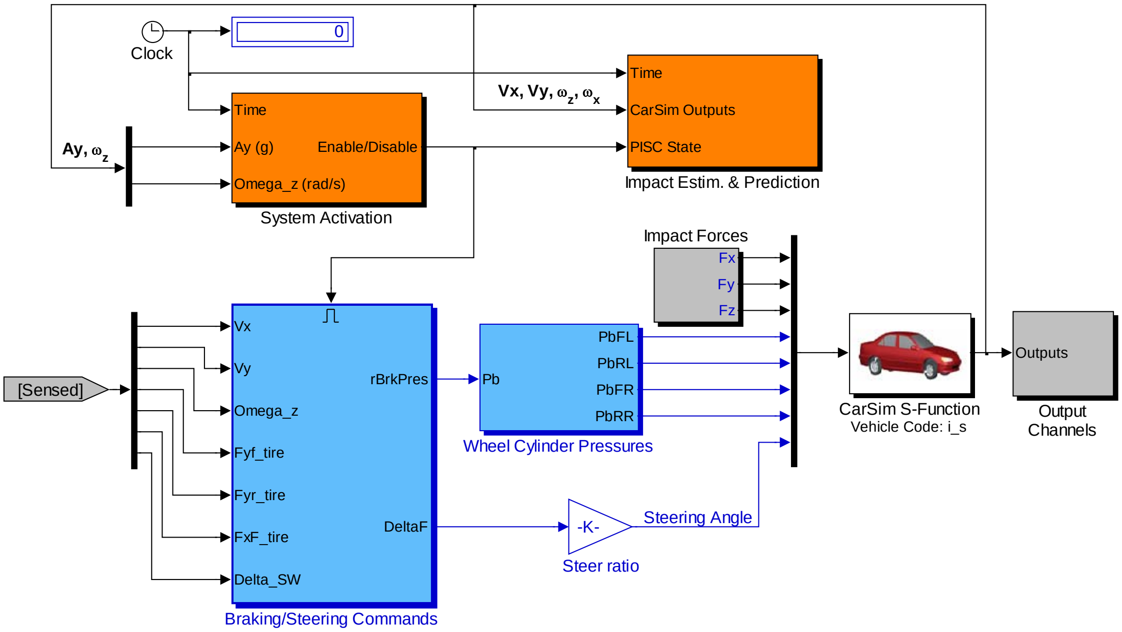

Figure 4.5: Block diagram of the PISC system

The overall structure conceptualized for this PISC system is modularized. It consists of four major subsystems (Figure 4.5): system activation/de-activation, impact estimation & prediction, the generation of braking/steering commands, and the designation of wheel cylinder pressures. The vehicle dynamics model in the form of a CarSim S-function takes external impact forces, four wheel cylinder pressures, as well as active steering angle as inputs, and outputs an array of variables for analysis and visualization.

The subsystem for the differential braking/steering control mechanisms is a Simulink implementation for the PISC controller detailed in Section 4.2 and the wheel-slip control algorithm discussed in Section 4.4. It generates raw braking pressure commands and a front wheel steering angle based on measured and estimated vehicle states. Under normal circumstances, it is in stand-by mode. It is activated only when an impact is detected. The “enable/disable” flag signal is provided by the block “System Activation.”

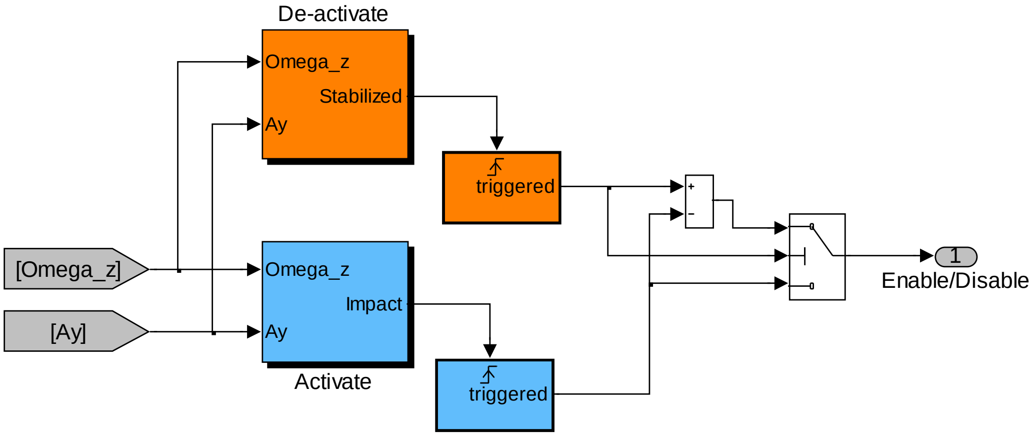

Figure 4.6: PISC system enable/disable logic

Essentially there are two parts inside the “System Activation” block (Figure 4.6). When an impact is detected through substantial changes in yaw rate and lateral acceleration, an enabling flag signal is generated (refer to Section 3.2). When the post-impact vehicle states fall below preset thresholds, a disabling flag signal is generated to pass control authority to the regular ESC/RSC systems.

The status of the “Enable/Disable” signal is also fed into the block “Impact Estim. & Prediction,” a Matlab implementation of the crash validation scheme in Section 3.3. If the sensed crash event is confirmed, the value of the enabling flag will not be altered. However, if the scheme determines that the apparent crash event is actually a false alarm, a global variable representing the status of the enabling flag will be reset to zero and the PISC will be forcibly de-activated.

If the crash is correctly detected and the PISC controller is activated, the control authority needs to transition back to ESC at the proper moment. When post-impact driver steering is not present, the PISC system will keep attenuating post-impact vehicle motions and be de-activated until certain stabilization criteria are met. The criteria are the measurement of three progressively decreasing, and sufficiently small samples in both yaw rate and lateral acceleration. The thresholds for yaw rate and lateral acceleration are 15 deg/s and 0.3 g, respectively. These threshold settings are chosen to make the transition to ESC take-over smooth because vehicle motion has settled down to a manageable range for the driver.

If the driver starts post-impact steering after certain perception and reaction time has elapsed, ESC braking commands should have priority over PISC commands, because the driver may want to steer clear of obstacles or follow a specific trajectory. Since PISC has been operating before the driver initiates reactions, it is easier for ESC to track drivers' desire yaw rate and limit vehicle sideslip angle given mitigated levels of vehicle yaw and lateral motions.

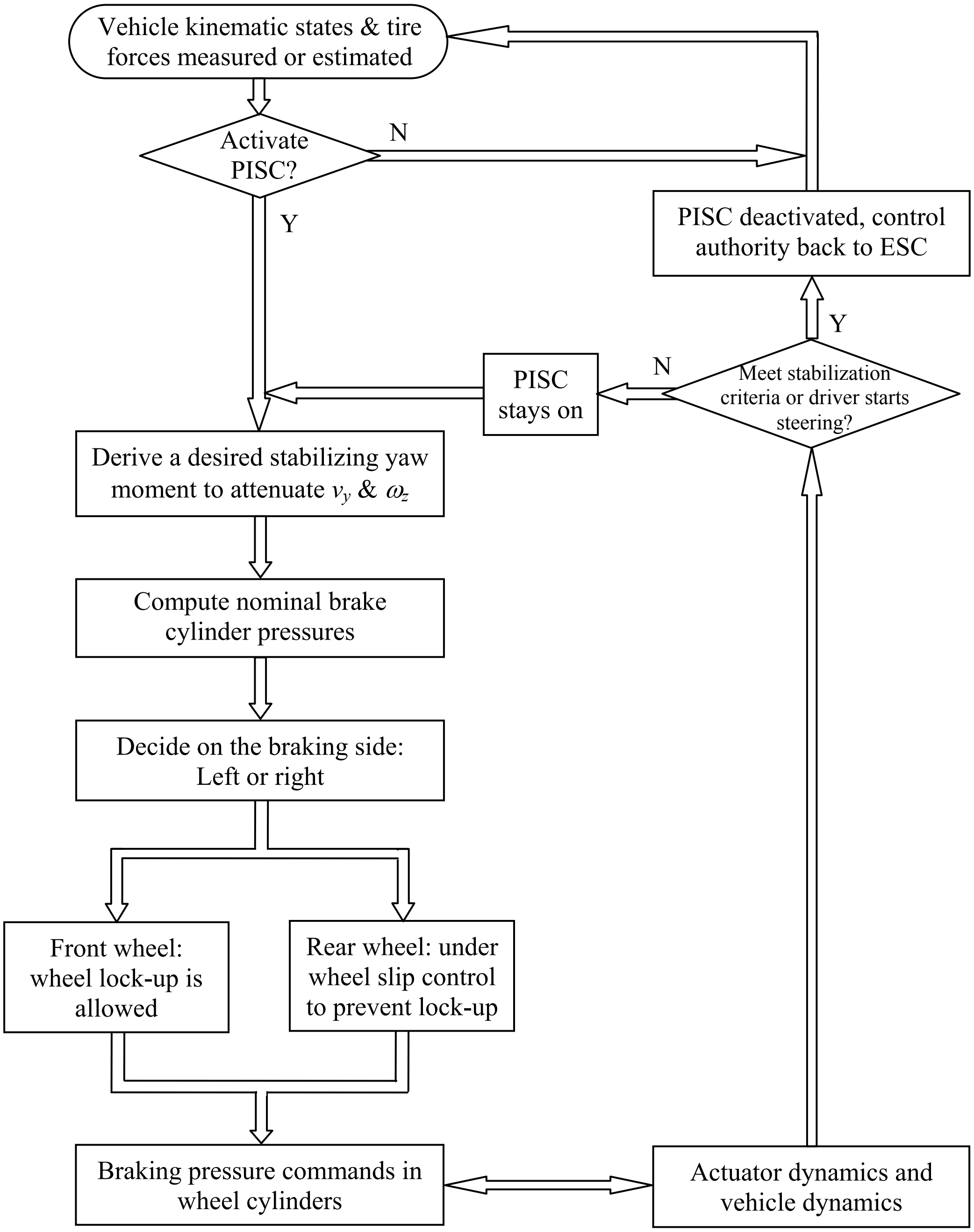

Figure 4.7: Flow chart of the overall PISC system

Inside the block “Wheel Cylinder Pressures” of Figure 4.5, braking pressures at four wheels are finalized. At each time instant, only the wheels on one side (left or right) are braked. The choice of braking side is contingent on the sign of the desired yaw moment. As for the level of braking, the pressure on the front wheel is given by Eq. (4.23) and the pressure on the rear wheel is the lesser of those computed by Eqs. (4.23) and (4.37). The wheel cylinder pressures on the non-braking side are zero. Ultimately, these four braking pressure commands, along with the desired active steering angle given by Eq. (4.22), are fed to the vehicle dynamics model in CarSim.

Figure 4.7 summarizes the operation of the proposed PISC system. The diamond-shaped block on the left corresponds to the decision-making procedure detailed in Figure 3.2 of Chapter 3. Each rectangle block represents a major operation on the relevant signals.

4.6 Simulation Results of Vehicle Regulation

To evaluate the effectiveness of the proposed PISC system, simulations are performed to compare vehicle motions with various post-impact safety countermeasures.

The simulated collision has the same layout as the one illustrated in Figure 2.7. Both the target (Vehicle 1) and bullet (Vehicle 2) vehicles are traveling along their own longitudinal axes when the collision occurs, with v_{1x} = 29 m/s (104 km/h, or 65 mph), $v_{2x'}$ = 33.5 m/s (120 km/h, or 75 mph), and their initial lateral velocities, yaw rates, and roll rates are all zero. The target vehicle is aligned with the road tangent, whereas the bullet vehicle has an orientation angle θ_2 = 25°. At the instant of crash, the impact location of the bullet vehicle is at the center of its front bumper, while the impact location of the target vehicle is 0.1 m to the left of its rear bumper center. The coefficient of restitution is assumed 0.20 for this rear-end crash. It is further assumed that no lateral impulse is generated on the bullet vehicle. The road is straight and its adhesion condition is homogeneous with μ_R = 0.70.

The responses of the target vehicle to the impact forces have previously been shown in Figure 2.8. Without the intervention of automatic control systems or by the driver, the peak post-impact yaw rate can reach −89°/s, and the vehicle develops a substantial lateral velocity. In fact, it takes a mere 0.9 s for the vehicle CG to cross the right lane boundary, and the vehicle keeps spinning and skidding until its kinetic energy is consumed by ground resistance forces.

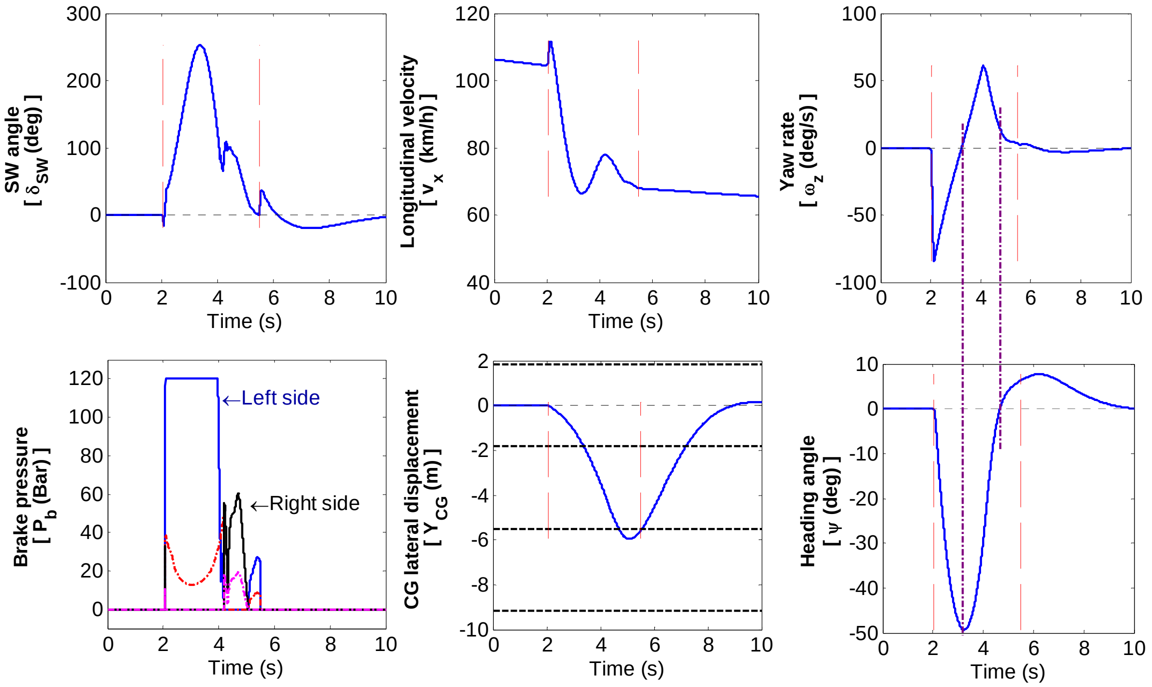

Figure 4.8: Inputs and outputs of the target vehicle with the PISC system (Part 1)

When the target vehicle is equipped with the PISC system, time responses of key inputs and outputs are shown for the complete collision and post-impact stabilizing process in Figure 4.8 and Figure 4.9. The collision triggers the crash sensing algorithm and the PISC system is activated within the time interval from 2.05 s to 5.48 s, which is delineated by vertical dashed lines in the subplots. It is further assumed that the driver takes over the control authority as soon as the PISC system is de-activated, because the yaw rate and lateral acceleration of the vehicle have been mitigated to levels that a normal driver can handle easily. The driver model smoothly steers the vehicle back to its original course, and eventually yaw rate, lateral velocity, lateral displacement, and heading angle all converge to zero.

In Figure 4.8, the two subplots on the left side present the steering angle and braking pressure inputs determined by the control system. Since the vehicle is veering fast towards the right side after the impact, a significant positive steering angle is commanded to turn the front wheels to the left. The braking pressure profiles have three distinct phases, that is, left−right−left, and then the braking control ends. The control system properly allocates brake pressures to either side, and there is no overlapping in brake pressure profiles. The maximum pressure of the wheel cylinders is set at 120 bar.

The histories of the CG longitudinal velocity and CG lateral displacement are shown in the middle column in Figure 4.8. The longitudinal velocity experiences an abrupt jump to 31.1 m/s (112 km/h) caused by the collision. When the PISC system is de-activated, the velocity has fallen to 18.9 m/s (68 km/h) due to braking. The peak CG lateral displacement is -5.96 m; in other words, the vehicle has shifted two lanes over (the horizontal dashed lines in this subplot represent lane boundaries). In general, lane departures pose significant safety threat to surrounding traffic. However, the sharp lateral deviation in this post-impact scenario is partly due to the intensity of the collision, and partly due to the primary control objective of attenuating yaw rate and lateral velocity. It will be shown later in this section that compared with post-impact control via four-wheel-braking, the PISC system may achieve better overall performance at the cost of a slightly larger lateral deviation.

The two subplots in the right column of Figure 4.8 show the evolution of yaw rate and heading angle throughout the collision and post-impact control process. There are two vertices in the yaw rate responses. The first and negative one is caused by the collision itself, whereas the positive vertex (60.8°/s) occurs because one of the control objectives is to realign the vehicle with its original course. The peak heading angle is -49.3°, considerably smaller than the uncontrolled case where the vehicle could spin more than 360° before it stops. Two vertical dashed lines are drawn to relate these two plots, corresponding to the moments when the heading angle reaches its peak, and crosses zero for the first time.

Additional vehicle responses are plotted in Figure 4.9. Its left column presents the tire adhesion ratios ($\sqrt{F_x^2 + F_y^2} \big/ F_z$) of the four wheels, with the left wheels on top. In both subplots, the curves are fairly flat during the interval between 2 s and 4 s, and their values are close to the nominal road adhesion coefficient of 0.7, indicating that tires' adhesion capacity has been fully used. Since the front left (FL) wheel is allowed to lock up and has substantial slip angles during the interval, its resultant planar tire forces result in a lower adhesion ratio (around 0.5).

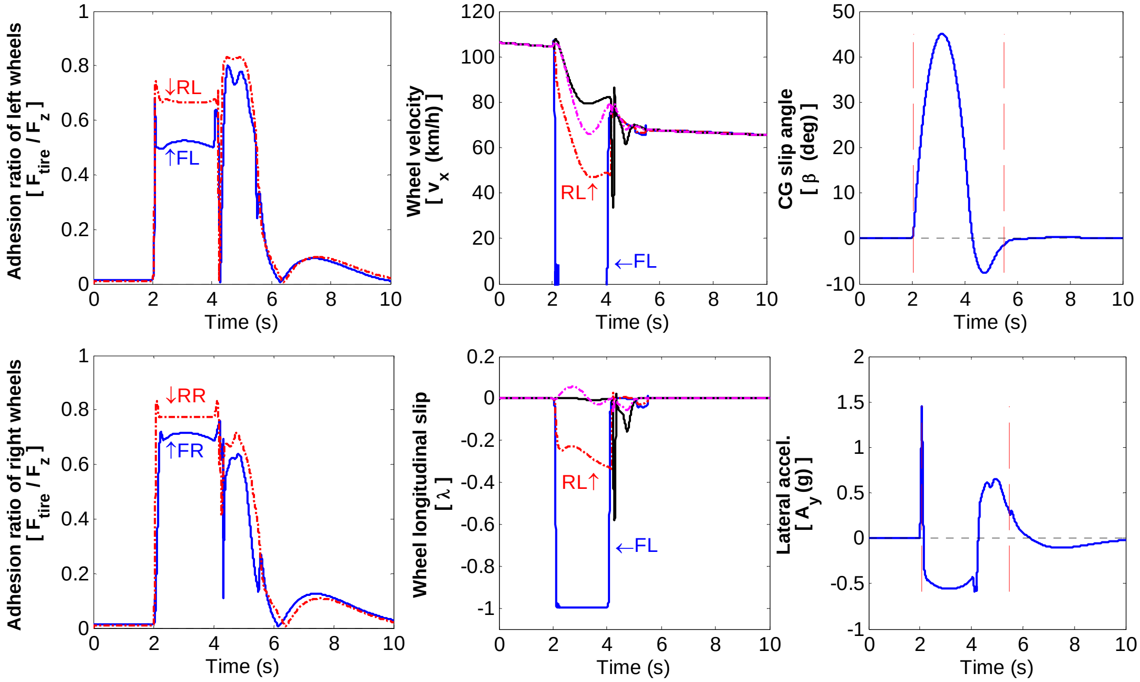

Figure 4.9: Inputs and outputs of the target vehicle with the PISC system (Part 2)

The middle column of Figure 4.9 shows the rotational velocities of four wheels (converted to linear units by multiplying with the tire radius) and their longitudinal slips. The lock-up of the front left (FL) wheel is noticeable, and there is no lock-up of any other wheels. The wheel slip of the rear left (RL) wheel is regulated around 0.2 during the first braking phase, consistent with the strategy discussed in Section 4.3.

The right column of Figure 4.9 displays the sideslip angle and the lateral acceleration at CG. The peak sideslip angle (45°) far exceeds the range encountered in daily driving, and will be highly challenging for an average driver. The initial collision causes a positive spike in lateral acceleration. Afterwards the target vehicle veers strongly to the right side and develops a substantial negative lateral acceleration. Eventually the PISC system attenuates the yaw rate and lateral velocity, and both the sideslip angle and the lateral acceleration decay to zero.

It should be pointed out that in this simulated event, the two colliding vehicles have the same specifications and the vertical component of the impact force is assumed negligible. No critical situation arises in vehicle's roll motion, thus the roll rate and roll angle of the sprung mass are not presented. Post-impact roll mitigation also belongs to the envisioned post-impact safety countermeasures, which may be addressed expressly in a future study.

For better appreciation of the effects of the PISC system, Figure 4.10 shows a comparison of vehicle trajectories. In particular, this figure presents the displacement and heading angle information for four vehicles subject to the same impact inputs, but with different post-impact control approaches. The vehicle positions at one second and three seconds after the impact are marked with "∗" and "×" symbols respectively. In each scenario, the space between two horizontal dashed lines represents one traffic lane (3.65 meter in width).

The controller for the case of "Differential Braking + Active Steering" has been discussed in detail earlier in this chapter. The case of "Differential Braking Only" is based on the same derivation as in the first one, only different in that the active steering part is disabled. In the case of "Full Braking, No Steering," identical braking pressure commands are applied to all four wheels (further modulated by an ABS controller after brake proportioning) starting from 0.5 s after the onset of the impact. The last case, "No Braking, No Steering," simulates the situation when no driver intervention or activation of automatic control systems is involved.

The first two cases in Figure 4.10 demonstrate the benefits of post-impact control systems. In both cases, although the vehicle deviates to the second neighboring lane, vehicle yaw stability is well controlled. The control system attenuates intense post-impact motions, and ultimately the vehicle proceeds along its original course. In the two cases at the bottom, vehicle stability is lost, which is indicated by a final heading angle of more than 300°. Although the "Full Braking, No Steering" control results in a peak lateral deviation slightly lower than the other three, this loss of yaw stability makes it an undesired option. The worst situation of these four occurs when there is no control at all. The vehicle spins strongly and skids to right edge of the road before it stops.

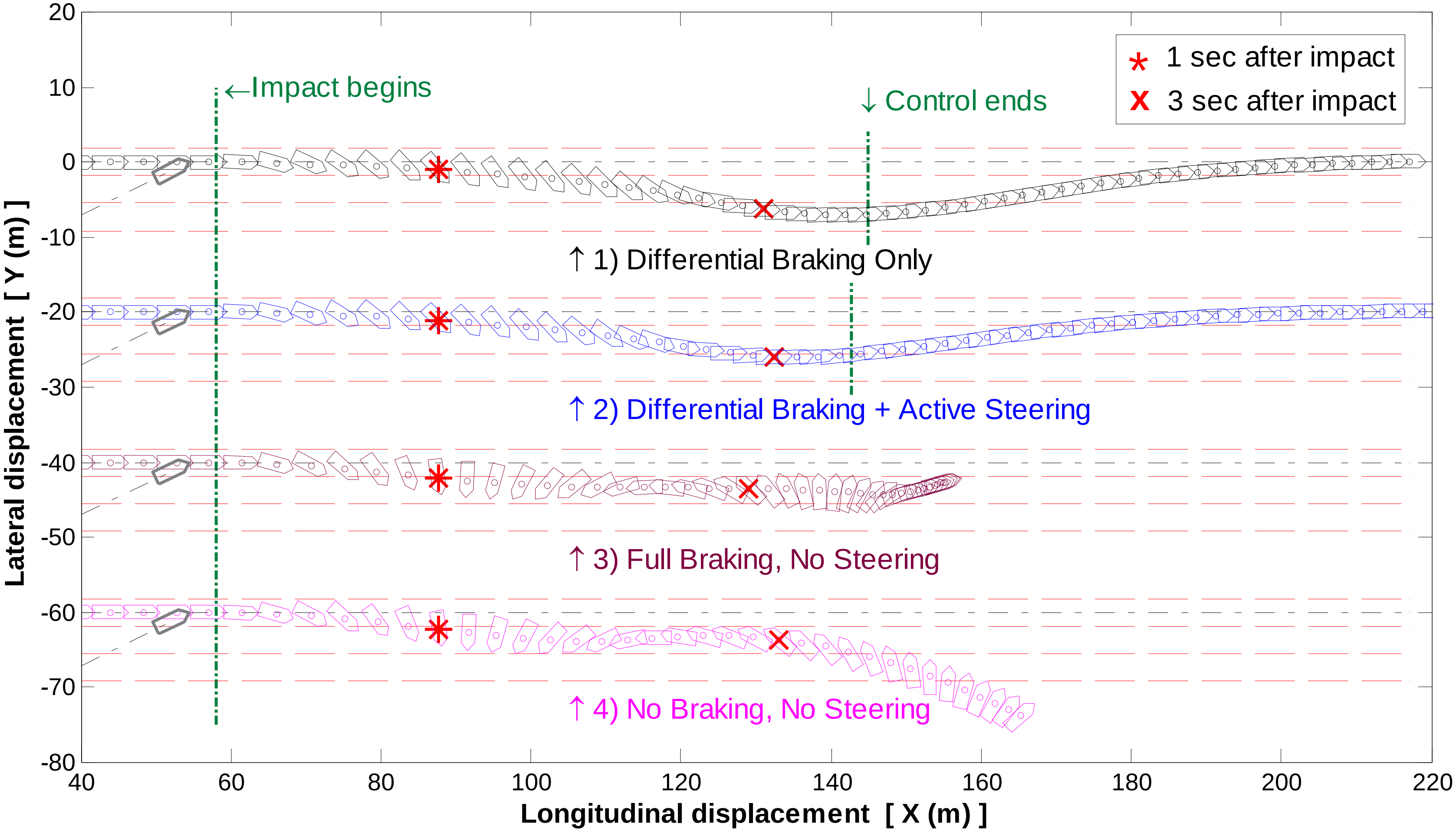

Figure 4.10: Comparison of vehicle trajectories to the same impact input with various control approaches

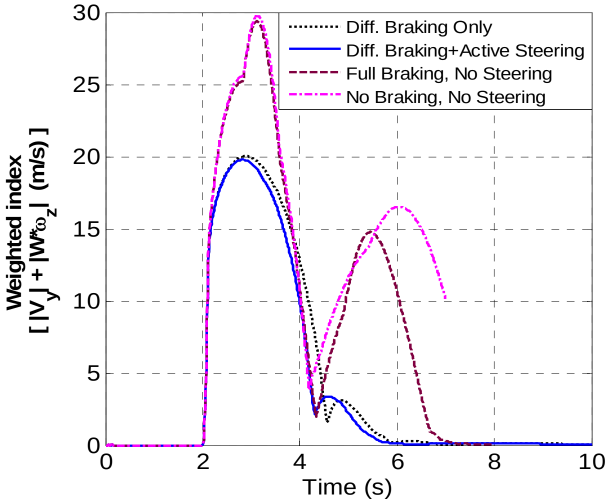

Figure 4.11: Comparison of post-impact countermeasures in terms of a weighted index

The four cases are evaluated in Figure 4.11 in terms of a weighted index for lateral/yaw stability. Since the vehicle is supposed to travel along a straight road, the desired lateral velocity and yaw rate are zero. A performance index *J* is defined below as the sum of the absolute values of lateral velocity and the weighted yaw rate.

$$J = \left|v_y\right| + \left|W \times \omega_z\right| \tag{4.39}$$

The weight *W* in Eq. (4.39) is used to penalize instantaneous yaw rate and convert its unit into m/s. The choice of the weight is based on the steady-state cornering behavior of a linearized lateral/yaw vehicle model as below. It can be proven that the steady-state relationship between lateral velocity and yaw rate is a function of longitudinal velocity, if vehicle parameters are specified. The parameters are listed in Table 2.1.

$$W\left(v_x\right) = \left.\frac{v_y}{\omega_z}\right|_{ss} = b - a\frac{Mv_x^2}{LC_r} \tag{4.40}$$

Figure 4.11 confirms that the “Diff. Braking + Active Steering” control achieves the best performance. The perturbation by impact forces inflates the performance index *J* in all cases. The PISC system manages to damp it down to an insignificant level within three seconds, whereas *J* remains high in the full-braking and uncontrolled cases even four seconds after the impact. In the full-braking case, although eventually the index *J* decays to zero, the attenuation of lateral velocity and yaw rate is actually a by-product of the reduction of vehicle velocity, rather than the direct consequences of stability control.

4.7 Effectiveness Comparison of ESC and PISC System

4.7.1 Assessment of the ESC System

The simulations to assess the capability of the ESC system used in this work are performed with a nonlinear multibody full vehicle model in veDYNA software package [72]. The vehicle model is built on a big SUV, with modeling details for tire, suspension, steering, braking, among other subsystems. The key parameters are summarized in Table 4.1. The ESC module is not developed in this work, but adopted from a previous research study conducted at the Ford Motor Company. The original ESC algorithm is tuned for this SUV model.

Table 4.1: Vehicle parameters for the simulated SUV model

Parameter	Description	Value	Unit
M	Total vehicle mass	2221	kg
m_R	Rolling mass	2001	kg
m_{NR}	Non-rolling mass	220	kg
a, b	Distance from axles to vehicle CG	1.329, 1.528	m
L	Wheelbase	2.857	m
h_{CG}	CG height above the ground	0.71	m
h	Distance from sprung mass CG to the roll axis	0.342	m
I_{zz}	Vehicle yaw moment of inertia about z axis	4536	kg·m^2
I_{xz}	Sprung mass product of inertia about roll and yaw axes	9	kg·m^2
I_{xxs}	Sprung mass roll moment of inertia about the roll axis	1214	kg·m^2
K_s	Total suspension roll stiffness	82527	N·m/rad
D_s	Total suspension roll damping	4880	N·m·s/rad
C_f	Front axle cornering stiffness	192193	N/rad
C_r	Rear axle cornering stiffness	212560	N/rad

The capability of the ESC system is assessed with three calibration maneuvers: fishhook, double lane change, and split-μ braking. The purpose is to contrast the handling performances of the vehicle under ESC-activated and ESC-deactivated circumstances, and to demonstrate the usefulness of the ESC module. Figure 4.12 contrasts vehicle responses in a fishhook maneuver starting from an initial velocity of 88 km/h (24.4 m/s).

The steering input induces a peak lateral acceleration at approximately 1g for both vehicles on a high-μ road. The vehicle with activated ESC successfully accomplishes the test. Its trajectory depicts a nice "hook" shape, and the slip angle is well contained. The application of braking pressures is additionally shown in Figure 4.13. Significant single-side braking can be observed, and the peak braking pressure can reach 75 bar. On the other hand, the vehicle with de-activated ESC fails to finish the maneuver. It develops substantial slip angle and eventually spins out.

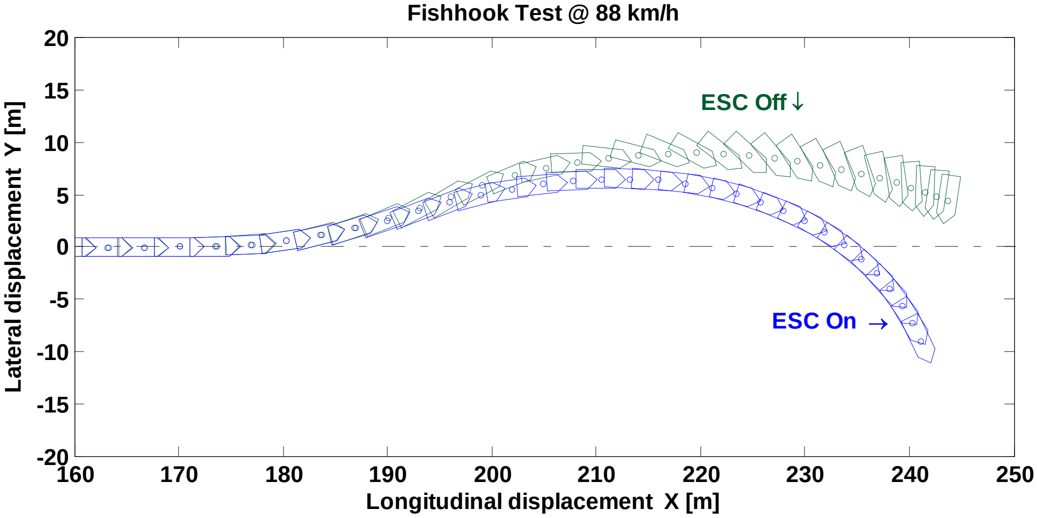

Figure 4.12: Comparison of vehicle trajectories in a fishhook maneuver at v_x = 88 km/h

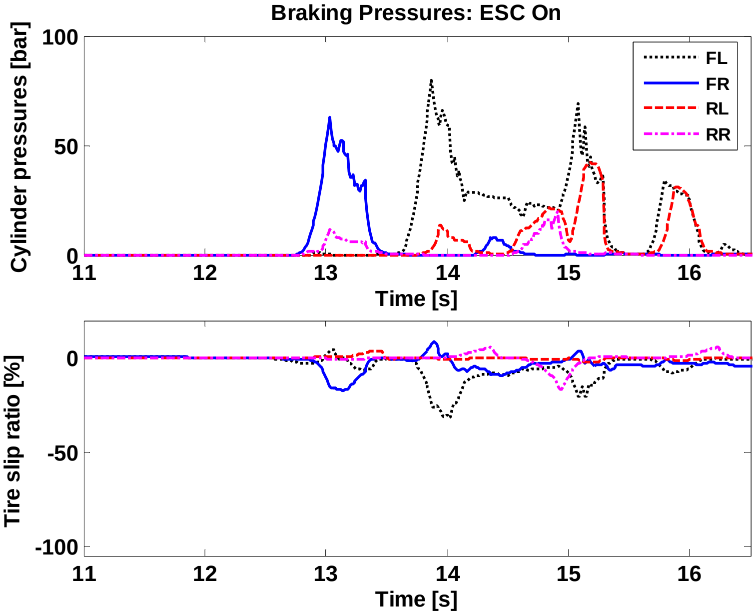

Figure 4.13: Application of braking pressures by ESC in a fishhook maneuver

The second test is a double lane change maneuver with the same vehicle model and ESC module. The vehicle trajectories are contrasted in Figure 4.14. Both vehicle start from an initial velocity of 120 km/h (33.3 m/s), and intend to finish the task under the directional control of a well-tuned driver model. The vehicle with activated ESC successfully accomplishes the maneuver and returns to its original lane without much deviation throughout the maneuver. The application of braking pressures is additionally shown in Figure 4.15. Significant single-side braking can be observed, and its correction of understeer and oversteer tendencies can be further analyzed. On the other hand, the vehicle with de-activated ESC fails to finish the maneuver. It cannot proceed in the designated lane and eventually spins out.

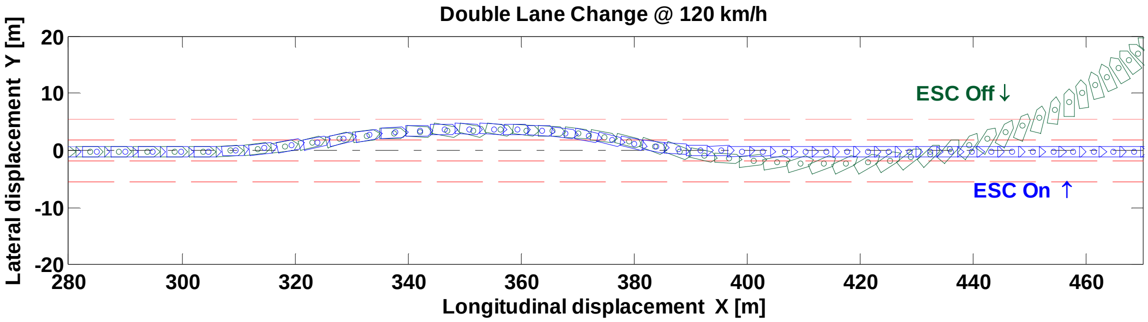

Figure 4.14: Vehicle trajectories in a double lane change maneuver at $v_x = 120$ km/h

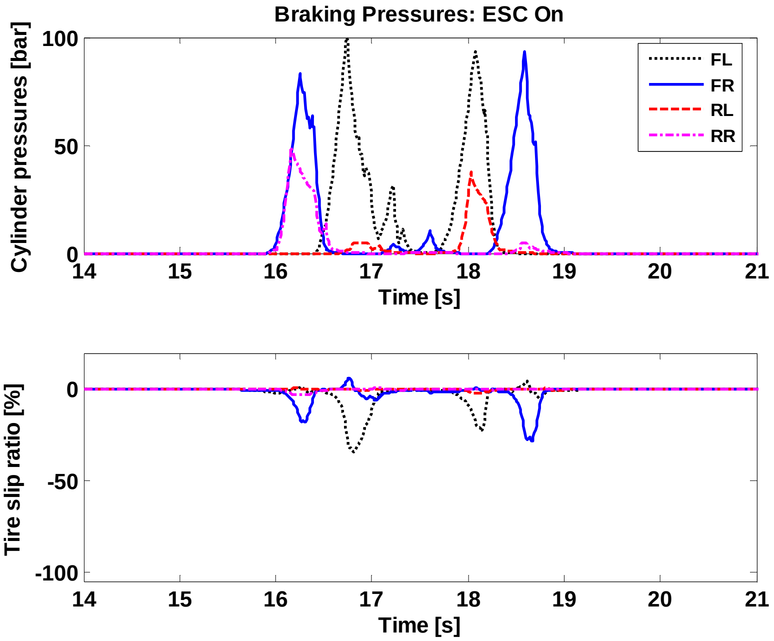

Figure 4.15: Application of braking pressures by ESC in a double lane change maneuver

The third test is a split-μ braking maneuver with the same vehicle model. The vehicle trajectories are contrasted in Figure 4.16. Both vehicle start from an initial velocity of 85 km/h (23.6 m/s) and brake with a deceleration of 2 m/s^2 on a road surface with uneven adhesion levels. The right wheels are on a high-adhesion surface ($\mu = 0.9$) all along, whereas the left half changes from high-μ to low-μ ($\mu = 0.45$) surface, indicated by the grey area in Figure 4.16. In order to highlight the intervention of ESC, no driver steering is allowed in this test. The vehicle with activated ESC successfully rejects the yaw motion induced by the uneven distribution of braking forces. Despite the lateral deviations, the vehicle can keep traveling forward without residual yaw rate or slip angle. The application of braking pressures is additionally shown in Figure 4.17. Significant single-side braking can be observed, as ESC seeks to modulate braking pressures given the deceleration request. On the other hand, the vehicle with de-activated ESC fails to finish the maneuver. It rotates quickly towards the high-μ side and easily spins out.

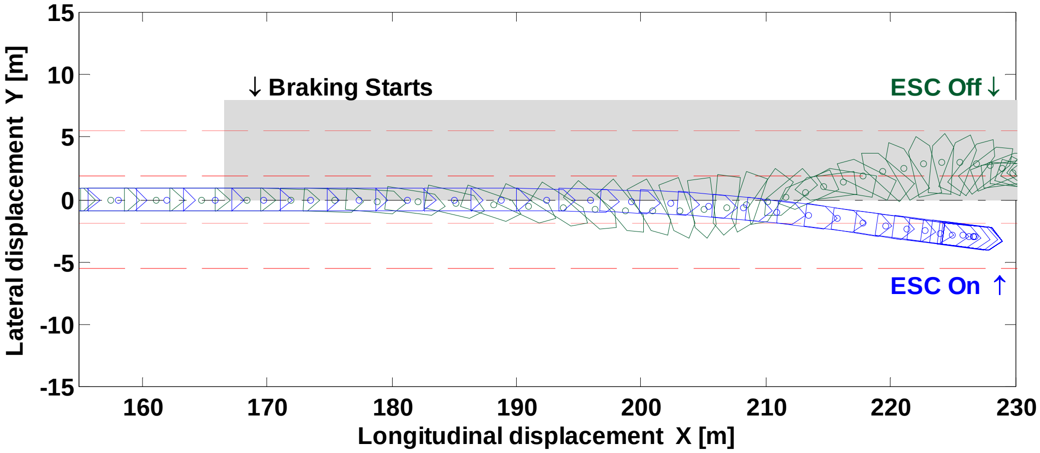

Figure 4.16: Comparison of vehicle trajectories in a split-μ braking maneuver

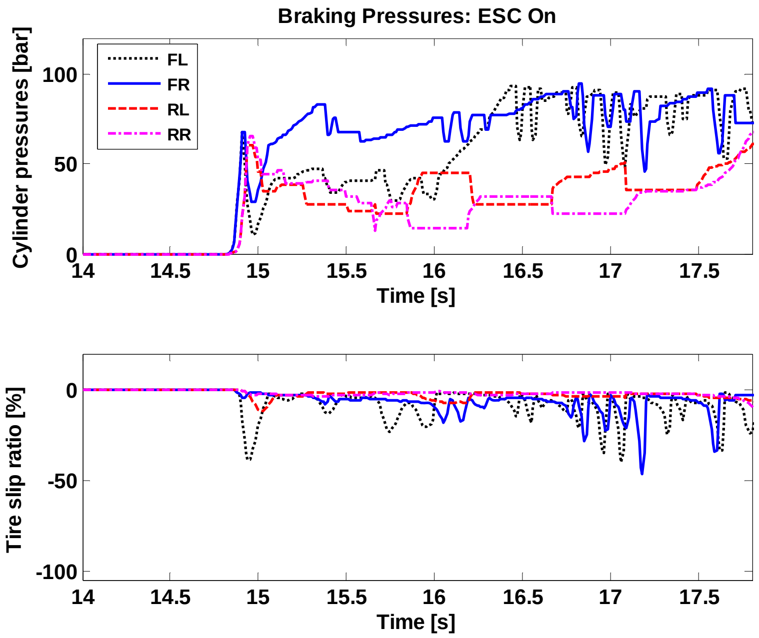

Figure 4.17: Application of braking pressures by ESC in a double lane change maneuver

4.7.2 Comparison of Post-Impact Stabilization Effects

In a larger context, the effectiveness of the PISC system is evaluated with a matrix of collision conditions and contrasted with the effectiveness of other control approaches, such as ESC system and full braking approach. The simulation scenario is illustrated in Figure 4.18. Originally the vehicle was traveling along its longitudinal directions with v_x = 30 m/s on a road surface with $\mu = 0.8$; its initial lateral velocity, yaw rate, and roll rate were all zero. Then it was subject to an impulsive disturbance applied to its rear bumper, intended to mimic an angled rear-end collision without involving much detail about the striking vehicle. The impulsive force lasts 0.15 s and has a triangular profile with a fixed peak magnitude of $3\times Mg$. The incidence angle of the external impulse and the impact point on the rear bumper are varied: the angle (θ_2) ranges from 0° to 40°, and the collision offset (y_1) ranges from -1.0 m to 1.0 m. The simulations are performed in veDYNA software package with a nonlinear multibody full vehicle model with key parameters shown in Table 4.1.

The absolute values of the struck vehicle's post-impact yaw rate are presented in Figure 4.19. They range from zero (when the impact force passes through vehicle CG) to an extreme value above 120°/s. The intermediate values cover a wide spectrum of collision severities.

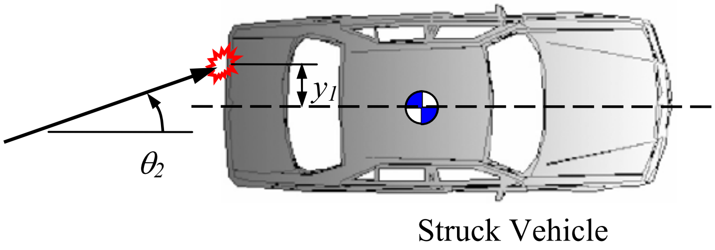

Figure 4.18: Vehicle subject to an external impulsive disturbance

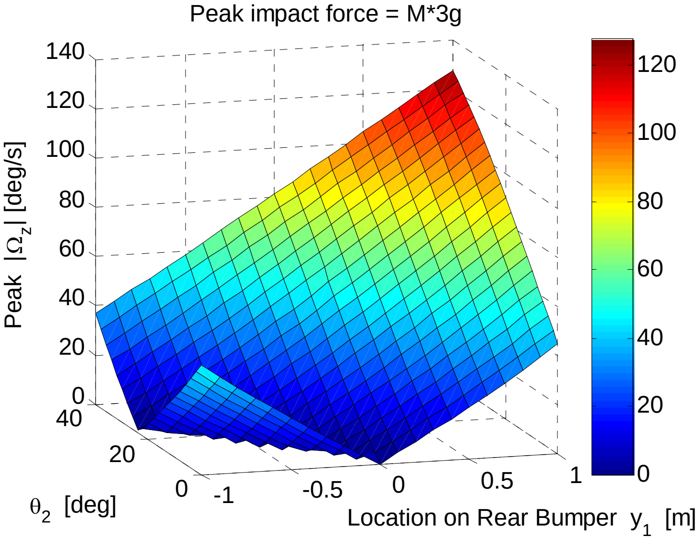

Figure 4.19: Vehicle yaw rate at the end of impact for angled rear-end crashes

Given the collision input levels indicated by Figure 4.19, various control approaches are applied to reject the influence of the disturbance and to stabilize the vehicle. Figure 4.20 compares the vehicle responses under four control approaches: no control, full braking with ABS, ESC, and PISC. The impulse input has an angle $\theta_2 = 36°$ and the collision offset y_1= -0.6 m. The resulting post-impact yaw rate has a moderate value of $|\Omega_z| = 45°/s$. Without the application of any braking or steering, the vehicle keeps spinning with a lateral acceleration of roughly 0.8g and develops a diverging slip angle before it stops. With the full ABS braking approach, the vehicle velocity is substantially reduced, and the slip angle of the vehicle is reasonably contained. The yaw rate eventually converges, although at a slower pace than the other two active control approaches. The delivered braking cylinder pressures are shown in the left column of Figure 4.21. It can be seen that the ABS controller strives to keep the slip ratios under 20%, despite some intermittent pressure spikes.

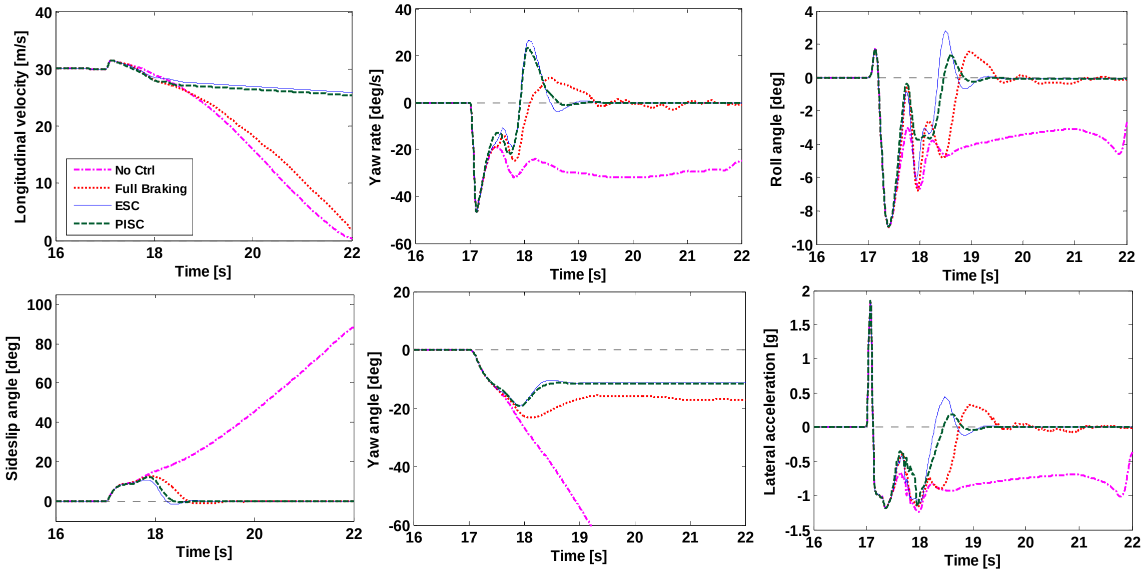

Figure 4.20: Comparison of vehicle responses after a impact with $\theta_2 = 36°$, y_1= -0.6 m

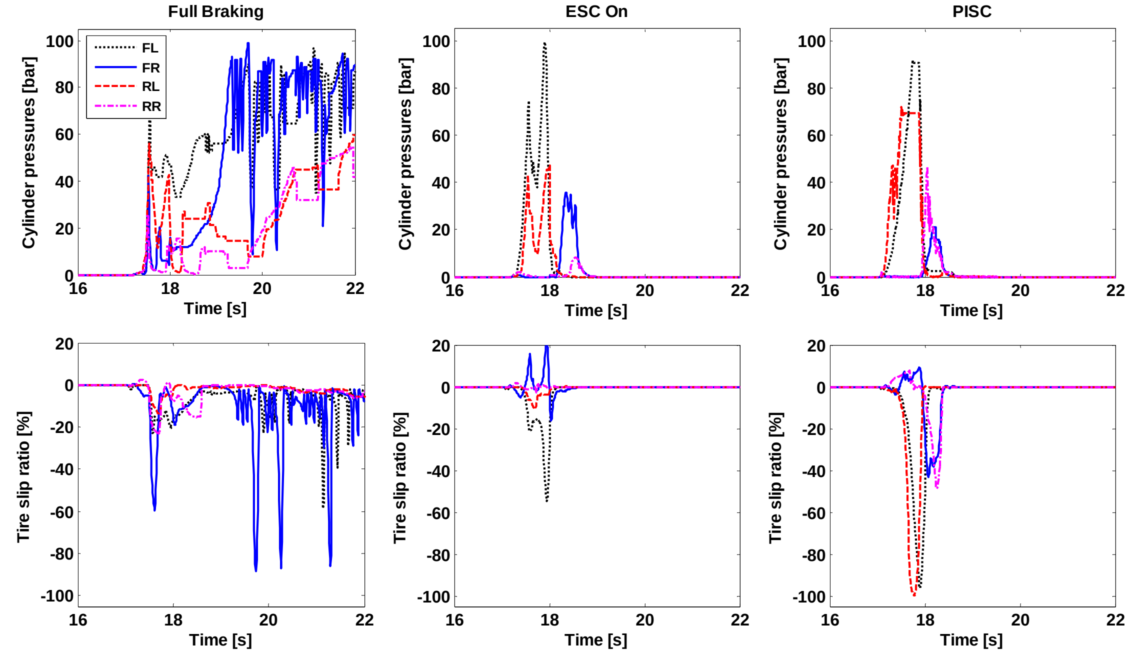

Figure 4.21: Comparison of braking pressures after a impact with $\theta_2 = 36°$, y_1= -0.6 m

With the ESC system activated, it immediately applies substantial braking pressures to the left wheels, and makes pressure adjustment in a later phase (the middle column in Figure 4.21). ESC intervention occurs automatically without driver-initiated braking and steering. As a result, the intense vehicle slip angle and yaw rate are quickly damped down, and the directional stability of the vehicle is recovered, despite a residual non-zero heading angle after the control actions are finished. For the vehicle under PISC control, similar vehicle responses is observed in Figure 4.20 as those for the case of ESC. The mitigations of slip angle and yaw rate occur almost at the same pace for the two vehicles. The braking pressure profiles for PISC system can be found in the right column of Figure 4.21. The pressure application phase and the total duration of system intervention are quite close to those in the middle column.

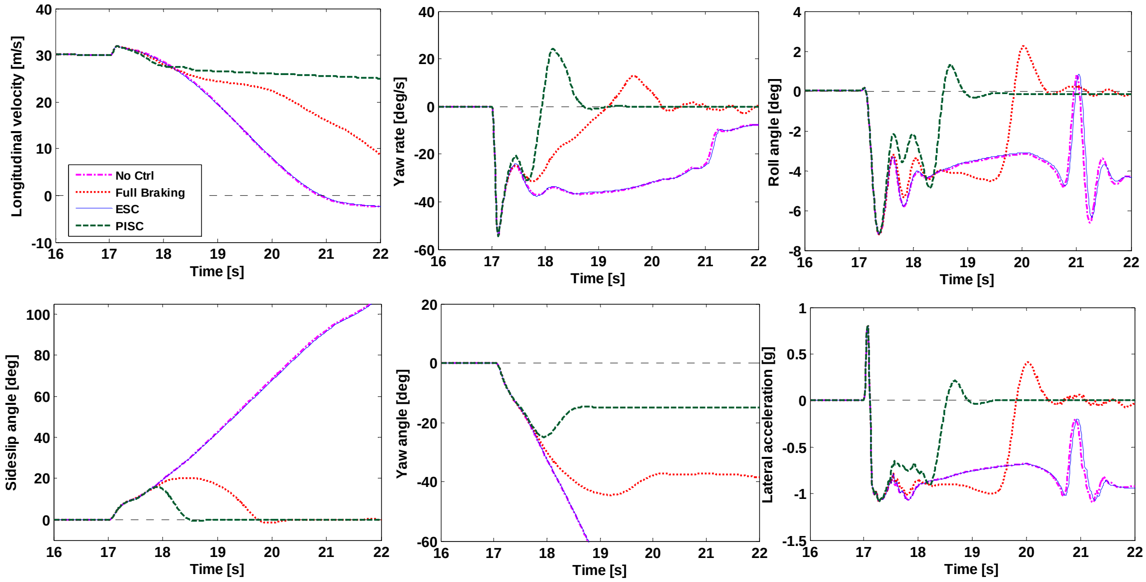

Figure 4.22: Comparison of vehicle responses after a impact with $\theta_2 = 8°$, y_1= 0.8 m

A second comparison of the effectiveness of various control approaches is shown in Figure 4.22, for which the impulse input has a different incidence angle $\theta_2 = 8°$ and a different collision offset y_1= 0.8 m from the example above. The resulting post-impact yaw rate has a more severe value of $|\Omega_z|$ = 55°/s. Again the vehicle responses are compared under four control approaches: no control, full braking with ABS, ESC, and PISC. Without the application of any braking or steering, the vehicle keeps spinning with a lateral acceleration of roughly 0.8g and develops a diverging slip angle before it stops.

With the full ABS braking approach, the vehicle longitudinal velocity reduces as intended. The slip angle can reach 20° and stays at elevated levels for a while, but eventually it converges to zero and the vehicle does not lose directional stability. The braking cylinder pressures are shown in the left column of Figure 4.23. It can be seen the slip ratios are kept under 20% by the ABS controller when the vehicle velocity is high.

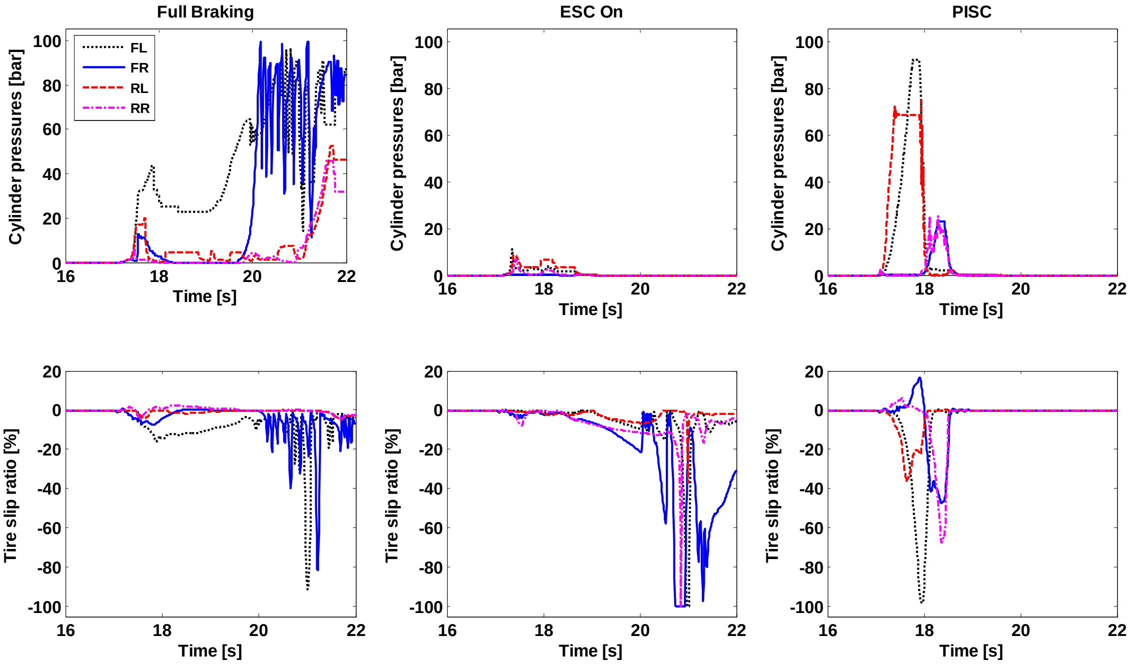

Figure 4.23: Comparison of braking pressures after a impact with $\theta_2 = 8°$, $y_1 = 0.8$ m

The handling of this case by the ESC system is quite different from the previous case. The middle column of Figure 4.23 shows ESC barely intervenes despite the severity of the impact. The reason for minimal ESC actions is: ESC is primarily designed to follow driver's intent and to limit vehicle sideslip angles. However, if the rates of change of key signals (e.g., yaw rate, lateral acceleration) exceed certain gradient thresholds due to the impact, ESC decides that these drastic gradients could not be caused by drivers' normal steering actions, and opts not to intervene in spite of the significant deviations from the desired values. Consequently, when the collision consequences are severe beyond the designed scope for ESC to cope with, ESC tends to stand by without mediating actively.

For the vehicle under PISC control, since PISC is designed specifically to detect and tackle the impulsive disturbance, timely and significant braking intervention is applied, as in the right column of Figure 4.23. As a result of the generated correcting yaw moment, the vehicle quickly mitigates the yaw rate and sideslip velocity induced by the impact and recovers stability (Figure 4.22). In practical situations, the driver may start to steer before the PISC intervention is completely finished. It is anticipated that due to the prompt suppression of post-impact yaw rate and slip angle by PISC, it will be considerably easier for the driver to maneuver the vehicle than the case without PISC intervention.

The evaluation results for the target vehicle over the test matrix are summarized as 3-dimensional surface plots in Figure 4.24, Figure 4.25, and Figure 4.26, which correspond to four-wheel full braking control (with ABS), ESC control, and PISC differential braking control, respectively. In each control scenario, two metrics are used for evaluation. The first metric is the minimum absolute yaw rate within one second after the impact. The choice of "one second" has both subjectivity and practical implications. After a collision, it takes time for the driver to perceive the incident and initiate reactions. During these short intervals without human intervention, automatic systems may attenuate a portion of impact-induced vehicle motions, so that when the driver starts to respond, the vehicle is more manageable. In many impacts, especially those with lower severity, an automatic stabilization control system can effectively mitigate the yaw rate, so that within one second after the impact, the yaw rate has crossed the zero, which means the heading angle has stopped building up and starts to decline. In these cases the first metric is simply zero.

The second metric $\Omega_Z\%$ is the mitigation percentage of the yaw rate within one second after the impact, which is defined in Eq. (4.41) and has a scale of 0 to 100. It indicates in percentage how much yaw rate remains to be dealt with after one second of the impact. Obviously, the lower the values is, the less demanding the task is if the driver takes over from this instant. For easier comparison, uniform axis limits are used in the related subplots.

$$\boldsymbol{\Omega}_z\% = \frac{\min\left(\left|\boldsymbol{\Omega}_z\right|_{t\in[t_0+0.1,\, t_0+1]}\right|\right)}{\max\left(\left|\boldsymbol{\Omega}_z\right|\right)} \times 100\% \tag{4.41}$$

Figure 4.24 shows the computation results with post-impact four-wheel braking control (with ABS). Two examples were given in the left columns of Figure 4.21 and

Figure 4.23. Distinct yaw motion mitigation effects can be observed for less severe situations, especially when the incidence angle θ_2 is relatively small. However, in those extreme cases, the yaw rate mitigation effects is limited, with residual yaw rate values higher than 90%.

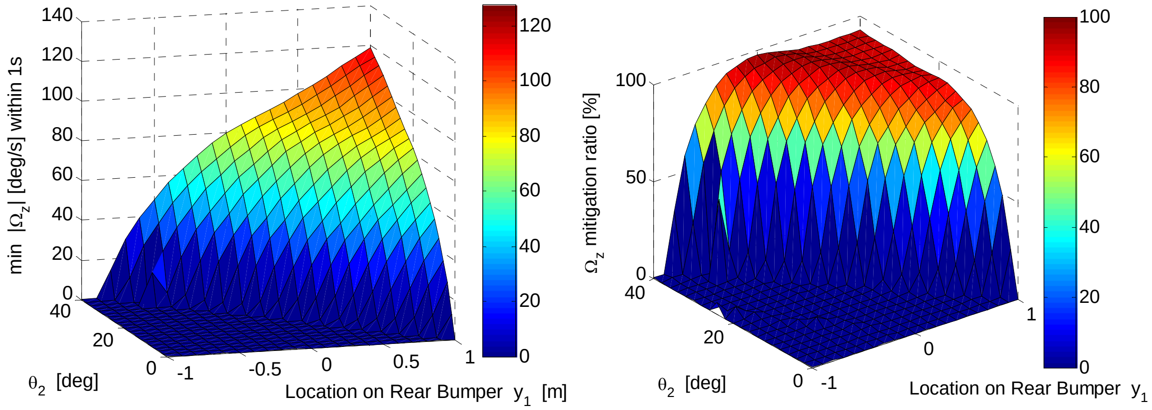

Figure 4.24: Performance evaluation with 4-wheel braking control: minimum yaw rate (left) and yaw rate mitigation ratio (right) within 1 s after impact

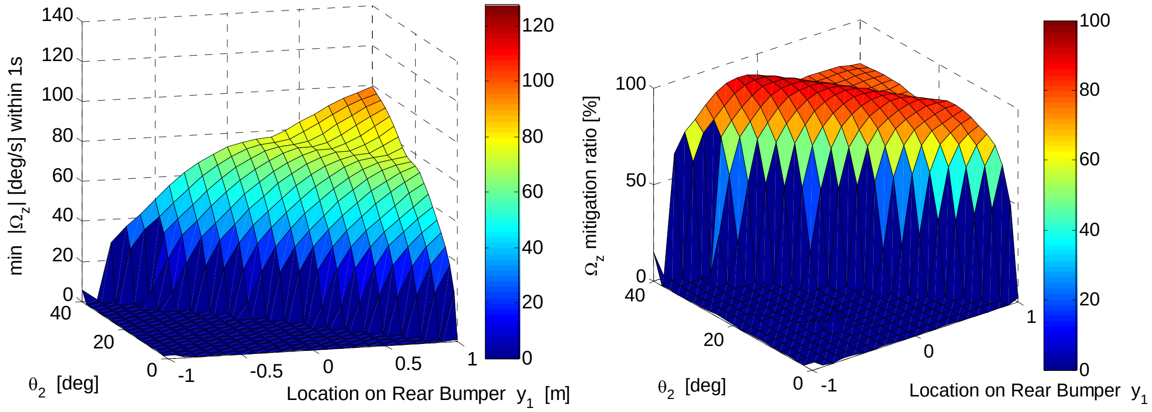

Figure 4.25: Performance evaluation with ESC system: minimum yaw rate (left) and yaw rate mitigation ratio (right) within 1 s after impact

Figure 4.25 presents the same set of evaluation results for the vehicle under ESC control. Two examples of ESC intervention were given in the middle columns of Figure 4.21 and Figure 4.23. For the impacts with relatively small incidence angles θ_2, ESC is very effective in attenuating the yaw rate as expected. However, in those cases, although the mitigation effects of ESC is better than those of full braking (for instance, the worst residual yaw rate reduces from 120°/s to 100°/s), the overall performance is inadequate, with a large portion of the residual yaw rate ratio higher than 50%. One important reason has been exemplified by the middle column of Figure 4.23. When there is an abrupt change of vehicle states exceeding humanly possible thresholds, ESC may conclude that it is due to sensor malfunction or massive sensor noises, and decides not to follow driver-desired yaw rate. As a result, ESC may choose to stand by or intervene only minimally when stronger action is needed.

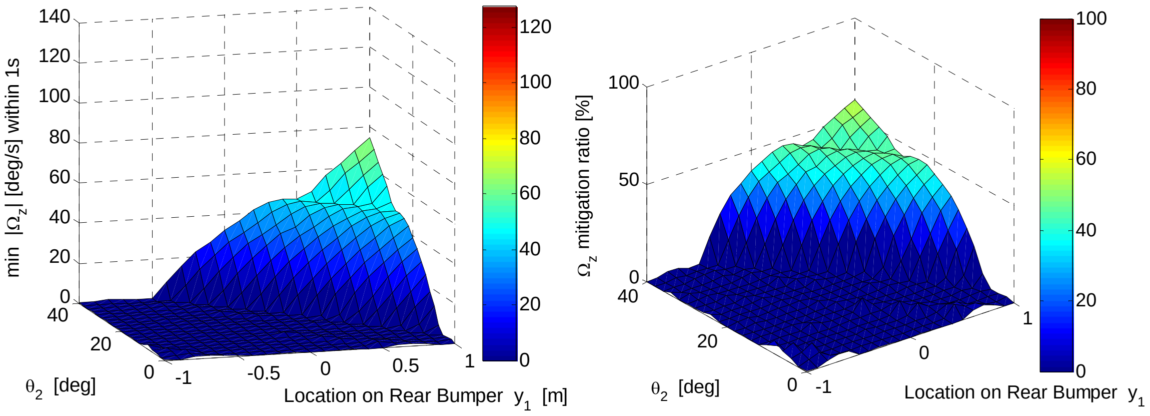

Figure 4.26: Performance evaluation with PISC system: minimum yaw rate (left) and yaw rate mitigation ratio (right) within 1 s after impact

Figure 4.26 presents the two metrics for the cases with PISC system. Two examples of PISC operation were given in the right columns of Figure 4.21 and Figure 4.23. The left subplot of Figure 4.26 shows that after impact the yaw rate can be effectively attenuated. Even in the most extreme case, the peak value has decreased to 78°/s. In the right plot, for most impact cases simulated, the residual yaw rate reduces by more than 50%, a ratio much more significant than in the previous two control approaches. In other words, PISC can reject the impulsive disturbance and attenuate the induced vehicle yaw motion more effectively, thus reduces the risk of secondary accidents due to loss-of-control caused by the primary collision event.

In summary, judging from Figure 4.24 to Figure 4.26, the performance of post-impact stability control compares favorably with those of full-braking and baseline ESC system. The benefits of PISC to mitigate undesired post-impact vehicle motions are clearly demonstrated, and Figure 4.26 quantifies the performance improvement for a subset of the targeted collision scenarios.

4.7.3 Vehicle Stability Analysis on Phase Plane

The phase plane analysis can provide additional insight into the vehicle handling stability even with a simplified bicycle model [73, 74]. Assuming that the longitudinal velocity of the vehicle is held constant, the equations of motion for vehicle's lateral and yaw dynamics can be obtained by applying Newton's second law of motion to the bicycle model.

$$M(\dot{v}_y + v_x\omega_z) = F_{yf} + F_{yr} \tag{4.42}$$

$$I_{zz}\dot{\omega}_z = aF_{yf} - bF_{yr} \tag{4.43}$$

The behavior of this dynamic system is characterized by the two states v_y and ω_z. Suppose this simplified vehicle model was originally traveling straight, and then was subject to an external impulsive disturbance, which displaced vehicle states from the origin on the phase plane to certain nonzero values. Figure 4.27 and Figure 4.28 show the migration of vehicle states on the phase plane from the post-impact status and onwards.

The vehicle model is based on a generic sedan with M = 1500 kg, I_{zz} = 3000 kgm^2, a = 1.2 m, and b = 1.3 m. The lateral tire forces F_{yf} and F_{yr} are nonlinear functions of the slip angles at the front and rear axles, and are modeled with the pure-slip Magic Formula model. The vehicle is moving on a road surface with a uniform low adhesion level. The steering angle is fixed at zero and there is no active braking throughout the maneuver.

Two scenarios are shown in Figure 4.27 and Figure 4.28 for two longitudinal velocities: v_x = 15 m/s and 30 m/s, respectively. Both figures indicate that if the severity of the disturbance is limited, the vehicle is able to stabilize itself, which is demonstrated by the converging trajectories inside the region enclosed by the dashed lines. However, if the disturbance is sufficiently strong, the vehicle states diverge further and the digression of slip angles indicates the loss of vehicle stability. Another obvious observation from Figure 4.27 and Figure 4.28 is: as vehicle velocity increases, the region of convergence shrinks.

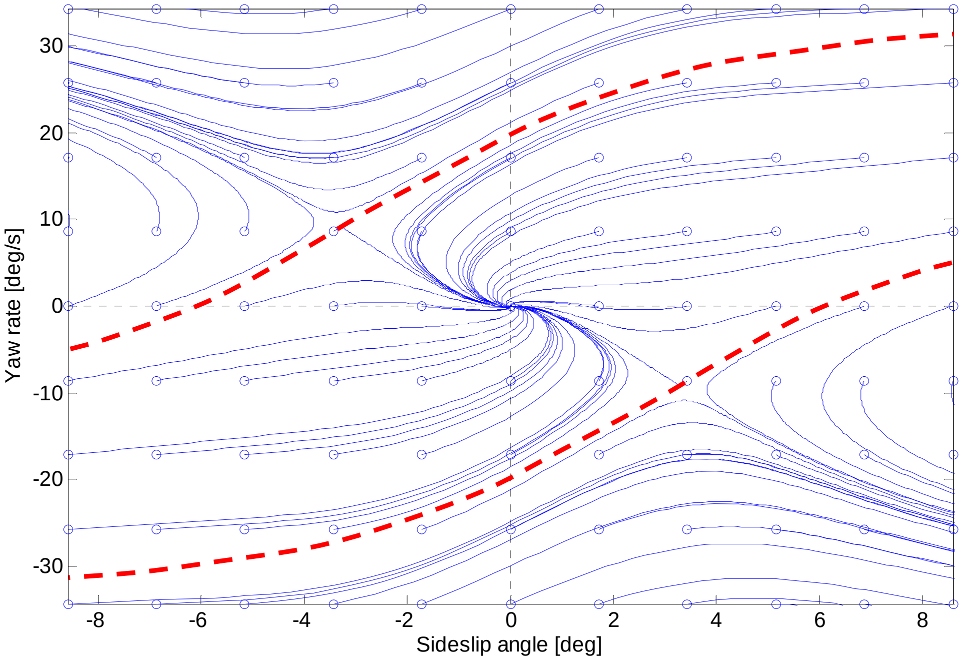

Figure 4.27: Vehicle state trajectories on phase plane after displaced by disturbances (v_x = 15 m/s)

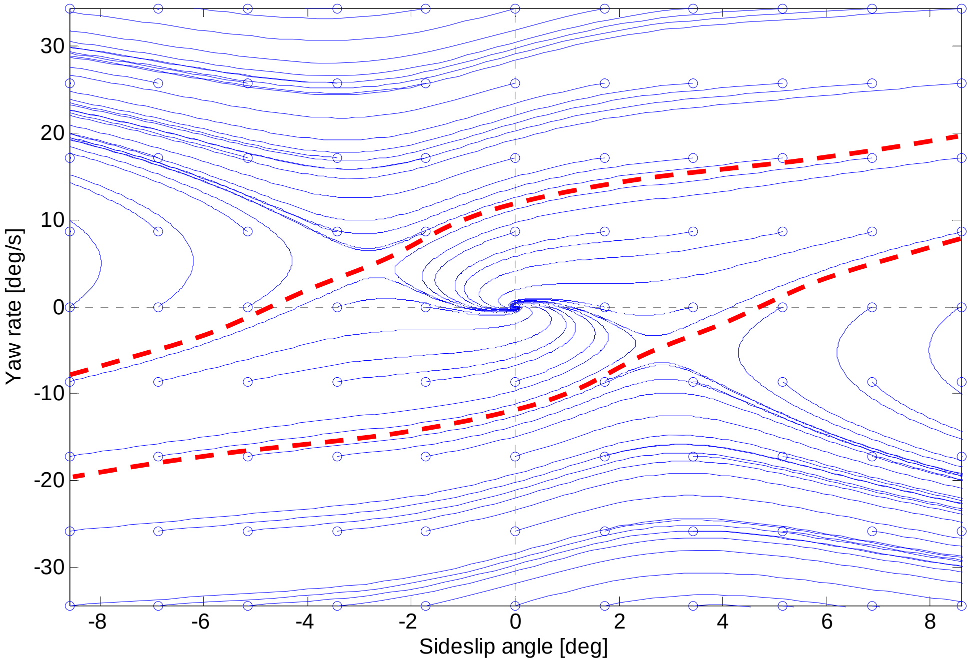

Figure 4.28: Vehicle state trajectories on phase plane after displaced by disturbances (v_x = 30 m/s)

As an extension to the previous comparison of ESC versus PISC, phase plane analysis provides an alternative way to quantify and contrast their effectiveness to reject disturbance and stabilize the vehicle. The simulation tests have the same setting as illustrated in Figure 4.18. The vehicle model, pre-impact conditions, as well as the way in which the impulses are applied have been detailed in Section 4.7.2. It should be kept in mind that in order to highlight the effects of the active control systems, no driver-initiated braking and steering is commanded to the vehicle.

Figure 4.29 conveys the information regarding vehicle stability in a different way based on the results presented in Figure 4.25 and Figure 4.26. In both subplots of Figure 4.29, each dot or cross on the phase plane represents the post-impact status in one simulation, and phase trajectories stemming from those dots are not shown to avoid clutters. As a result of the batch of angled rear-end impulses to the struck vehicle, the post-impact states are distributed in a band on the phase plane (instead of the whole plane). Depending on whether the following assessment criteria are met, a dot or a cross will be associated with that particular state: within 1 sec after the collision, vehicle's heading angle $|\psi| \leq 55°$, roll angle $|\phi| \leq 10°$, and lateral displacement $|y_{CG}| \leq 1.25\times$lane width. In both subplots for ESC and PISC, a demarcating line can be drawn to separate the sets of dots and crosses. In the top subplot for ESC, the line roughly corresponds to 45°/s in post-impact yaw rate, whereas the line is moved to about 89°/s yaw rate for the PISC system in the bottom subplot. In terms of the imposed assessment criteria, the range of effective intervention has been considerably extended, which testifies to the improved directional stability delivered by the PISC system quantitatively. Although only one pre-impact velocity and rear-end collision scenario are employed in this investigation, it is expected that the enhanced stabilization effects of the PISC system can be obtained at other speeds and in other collision types such as side impacts to the rear corner.

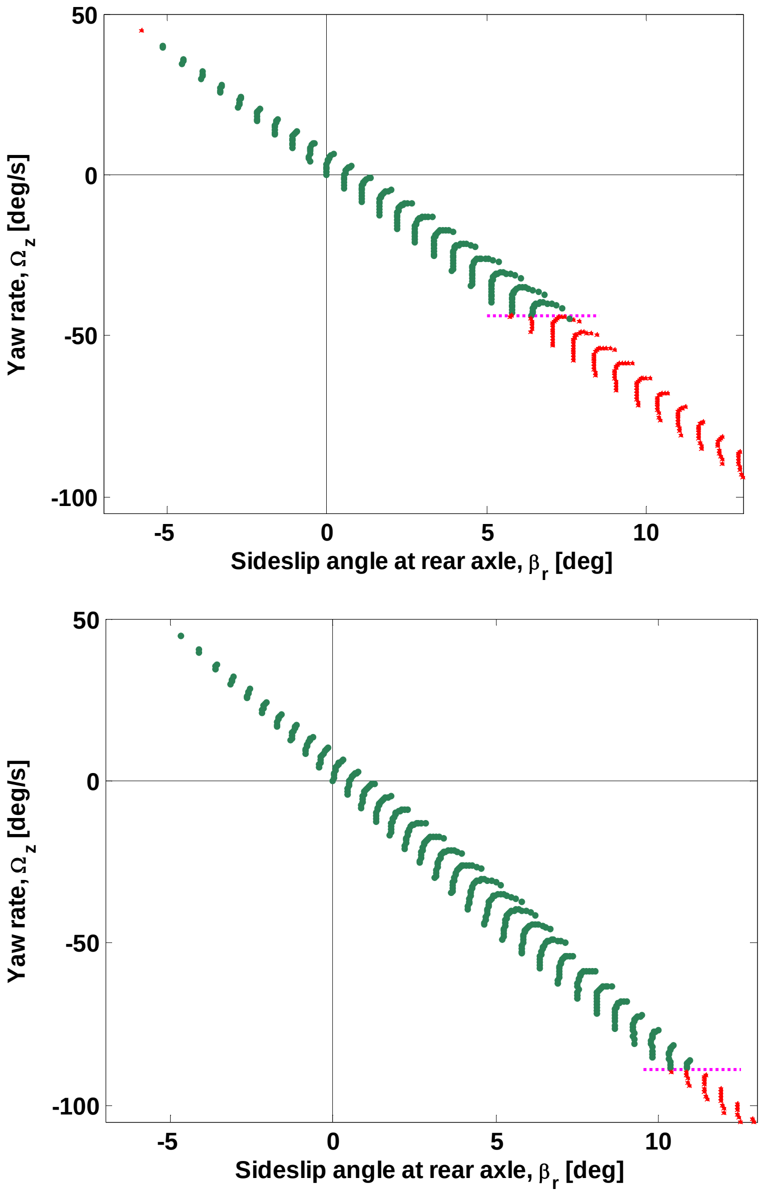

Figure 4.29: Characterization of control effectiveness with ESC (top) and PISC (bottom) on the phase plane

4.8 Summary

This chapter integrates various subsystems to stabilize intense post-impact vehicle motions via differential braking and active steering actions. The controller, which is based on the multiple sliding surface control approach, along with a crash sensing and validation procedure and wheel-slip control strategy, constitutes the essential modules of a PISC system. Its validity is verified in a representative collision event. Intense post-impact vehicle motions can be adequately mitigated so that vehicle stability is effectively recovered. Even if active steering feature is not equipped, differential braking mechanism alone can work successfully without much sacrifice in performance. More comprehensive evaluations of this control system demonstrate its benefits in terms of yaw rate mitigation and sideslip limitation.

Because both ESC and PISC systems are designed to assist drivers, instead of overtaking drivers' role, the effects of three control strategies (full braking, ESC, and PISC) are compared in terms of their capability to mitigate vehicles' undesired sideslip and yaw motions within a short interval (1 second is chosen) after crash occurs. Before the driver perceives the incident and initiates reactions, PISC has effectively attenuated a large portion of impact-induced intense vehicle motions, so that when the driver starts to respond, the vehicle becomes more manageable. The performances of full braking, ESC, and PISC are compared quantitatively in terms of their effectiveness within this critical short time interval, and PISC stands out by achieving outcomes that are more favorable.

In spite of the demonstrated effectiveness of PISC in rejecting external impulsive disturbances to the vehicle body and recovering vehicle stability, it has to be kept in mind that the targeted collision scenarios are still a limited subset of possible types of vehicle crashes. For instance, PISC systems are not designed for head-on collisions, because the vehicles involved may keep in contact with each other and their post-impact motions do not allow sufficient space to actively maneuver the vehicles.

In addition, the PISC system targets at destabilizing collisions within certain magnitude ranges. If the collision is unlikely to lead to a loss of directional stability (e.g. in a direct rear-end crash), or the induced yaw/sideslip motion may well be coped with by the driver with the assistance of ESC, PISC does not need to intervene. An example of the PISC intervention boundary was shown in the top subplot of Figure 4.29 at a forward velocity of 30 m/s. The boundary determined there can be regarded as the lower threshold for PISC to be activated. Extensive calibration work is required to determine the entire lower threshold for various forward velocities as well as directions of collision impulses.

Furthermore, PISC is not expected to deal with collisions of extreme severities, for instance, when airbags are deployed, or the struck vehicle spins out immediately due to enormous post-impact yaw rate. The acceleration level for airbag deployment is not a single uniform value and depends on multiple factors, but its firing status can be retrieved from the restraint control module and used for PISC activation decision. Under the circumstances of airbag deployment or extreme impact-induced yaw rate (as in the bottom subplot of Figure 4.29), the automatic application of maximum braking with ABS may be a preferred approach in terms of post-impact active safety. These scenarios constitute the upper threshold for PISC operation.

When the collision consequences fall into the intended operation range of the PISC system, the controller designed in this chapter demonstrated its capability to cope with vehicle stabilization on the yaw plane. However, if there are more performance variables under consideration, such as longitudinal speed reduction and rollover mitigation, the controller development becomes more complicated and less efficient. Because one needs to design separate sliding surfaces for each performance variable and enforces convergence, it inevitably leads to sluggish control responses and less coordinated operation. The control scheme developed in the next chapter proposes an approach to maneuver vehicle motions in a more systematic and coordinated way.

Chapter 5

MPC-Based Supervisory Control and Constrained Optimal Tire Force Allocation for Enhanced Vehicle Handling and Stability

5.1 Introduction

The multiple sliding surface control approach in Section 4.2 can be extended to include the attenuation of vehicle's roll motion explicitly. For this purpose, one needs to design three successive sliding surfaces for the control input M_z to be derived. The development of the controller can be based on a lateral-yaw-roll vehicle model similar to the one in Section 2.3 by excluding the impulsive inputs. However, since the three sliding surfaces are related in a cascading manner, the final control input cannot be synthesized until the feedback information propagates through each step. As a result, the vehicle responses may be sluggish, and cannot immediately mitigate post-impact sprung mass roll motions. In addition, controlled reduction of vehicle longitudinal velocity may be necessary in some cases when obstacles are present.

In order to achieve a better balance among the attenuation objectives of sideslip angle, yaw rate, roll angle as well as speed-reduction, it is desired to design the control scheme in a more integrated way, so that vehicle's post-impact motion can be coped with from a global perspective, and the control priority of translational, yaw or roll motions can be shifted accordingly.

5.1.1 Vehicle Handling Control with Multiple Actuators

Significant advances in automotive active safety have taken place in the past couple of decades [75]. Active steering, selective braking, and drive-by-wire systems, as well as active differentials are being deployed on new vehicle models by various automotive manufacturers, and the recent surge of interest in hybrid electric vehicles accelerates this trend. As more active control systems are installed on vehicles, it becomes necessary to control vehicle motions in a unified and coordinated manner. Since X-by-wire systems enable independent manipulation of steering, braking, and traction on individual wheels, they greatly increase the flexibility and capability in vehicle dynamics controls. However, they also present potential overlapping or conflict in control authorities, because tire forces are the eventual agents to affect vehicle motion. Given the interdependencies among these active systems and tire force generation, a major challenge is to find a systematic method to distribute the tire forces in a unified and optimal way, so that the available actuation resources can be better utilized and the overall control objectives can be achieved.

The concept of direct yaw-moment control (DYC) was proposed in [76], where the vehicle motion is controlled by yaw moment generated from the differential distribution of the tire longitudinal forces. It demonstrated significant benefits for improving vehicle performance in near-limit operating regions. Peng and Hu [77] concentrated on the optimal distribution of tire forces to deliver maximum longitudinal acceleration or deceleration while cornering successfully. The longitudinal and lateral forces of the tires were solved by constrained nonlinear programming and assumed available when requested. Hattori *et al*. [78, 79] proposed a vehicle dynamics management (VDM) concept to control the forces of individual wheels. They used a feedforward control to compute the desired longitudinal and lateral forces and yaw moment of the vehicle. A nonlinear optimal distribution method was used to distribute the desired forces and the moment of the vehicle to longitudinal and lateral forces on each wheel. Mokhiamar and Abe [80] also proposed an integrated vehicle dynamics control algorithm for 4-wheel-distributed steering and 4-wheel-distributed traction/braking systems, which minimizes the squared sum of workloads of the four wheels. However, the tire ellipse constraints were not considered, so the algorithm does not guarantee that the desired tire forces of all wheels are within adhesion limits.

5.1.2 Proposed Hierarchical Control System for Vehicle Handling

To control vehicle motions with coordinated actuations, it is crucial to determine proper tire forces on each wheel to achieve control objectives in an optimal way. The challenge here is that the longitudinal and lateral tire forces cannot be arbitrarily assigned due to the coupling and the physical constraints on tire forces. To decide how much force should be generated at each wheel under various driving circumstances, it is necessary to adopt a model-based approach.

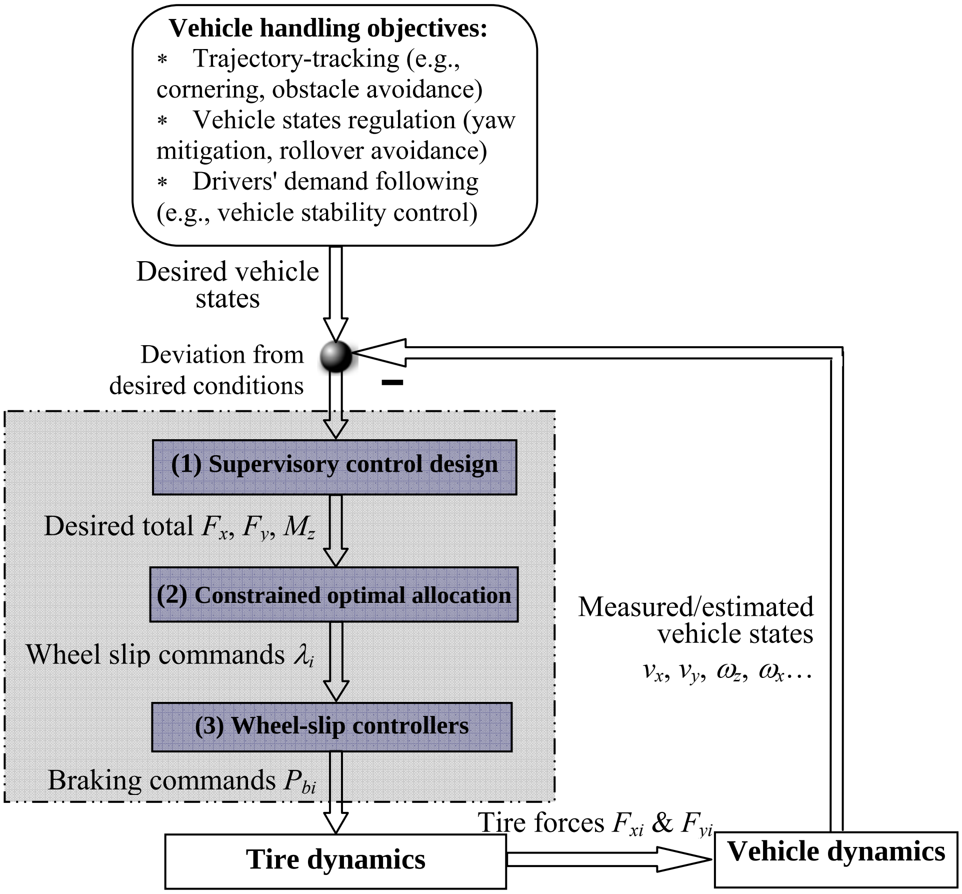

Figure 5.1: Hierarchical framework for vehicle handling control

The proposed control design procedure is illustrated in the flow chart shown in Figure 5.1. Regardless of the objectives of handling tasks, the desired values of vehicle states are first compared with their measurements or estimated versions. Then, in response to the state errors, a supervisory controller at the first stage determines the desired control efforts, namely, the desired total longitudinal and lateral forces and yaw moment. These forces and moment are requested to achieve handling control objectives without violating vehicle dynamic constraints (mainly from the tires). The adopted control scheme is based on the Model Predictive Control (MPC) methodology, because it handles multivariable and constrained nonlinear problems naturally. In the second stage, an optimal control allocator maps the total control demand onto individual actuators, in other words, slip ratios and slip angles on individual wheels. In the last stage, controllers at the actuator level manipulate physical variables to achieve the desired values dictated at the second stage, e.g., wheel cylinder braking pressures, traction torque, and steering angles. Finally, tire forces generated affect vehicle motion and the resulting vehicle states are fed back to the supervisory controller to close the loop.

The supervisory controller specifies the total forces and moments acting on the vehicle, so that certain handling or maneuvering performance characteristics can be accomplished. The desired resultant forces and moment need to be allocated appropriately to individual wheels. This design procedure is philosophically similar to feedback linearization and backstepping method in nonlinear control theory. A virtual control is first composed to reduce the original nonlinear system to a more amenable linear system. Then actual controls are determined subsequently so that the virtual control can be realized.

Some engineering systems, such as ground vehicles, aircrafts, and marine vessels, are analogous in that they are redundantly actuated. Here the system actuation redundancy means the number of actuators is greater than the number of system controlled outputs. In aerospace control, multiple effectors are used to produce the net torque acting on the vehicle, and govern its motion. In marine applications, to perform dynamic positioning of vessels, a set of thrusters is used to produce translational forces and yaw moment, in order to keep the vessel in place with the heading in the desired direction. To avoid conflict, improve performance, and ensure reliability, these actuators need to be employed in a unified and optimal way subject to their constraints.

The control allocation problem has been studied in the aerospace [81, 82] and marine [83, 84] industries. Control allocation for automotive vehicles was studied in [78, 85, 86]. In [78] a nonlinear optimization method was used to distribute the desired force and moment among the tire forces by resolving the magnitude and orientation angle of the force vectors on four tire contact patches. In [85] the quadratic programming technique was used and accompanied with a linear quadratic regulator to track a desired yaw rate trajectory while minimizing sideslip. Differential braking force at the rear and front tires and the steering angle of the front tires were used as control inputs. In [86] a coordinated vehicle dynamics control (CVDC) system was presented. Sliding mode control theory was first applied to derive a higher-level controller for total desired tire forces. Then a computationally efficient accelerated fixed-point (AFP) method is proposed to solve the constrained control allocation problem for individual tire forces. Individual tire slip and slip angles are selected as the control variables to resolve the inherent tire force nonlinear constraints.

In this chapter, it is decided to control vehicle motions via changing the slip ratio and slip angle of each tire directly, rather than the longitudinal and lateral tire forces. The reasons are twofold. First of all, slip ratios and slip angles are directly manipulated. Even in the case of tire force allocation, the desired forces need to materialize through braking pressures or steering angles. Secondly, the physical constraints on slip ratios and slip angles are more straightforward to resolve than on individual tire's forces.

The design of the three-stage controllers is conceptually independent from each other. With this modularized structure of the control system, vehicle motion controller design can be decoupled from control allocation. In addition, weighting factors can be assigned to prioritize the state variables and control inputs. For instance, longitudinal velocity and longitudinal tire force are important in an obstacle avoidance maneuver, but may not be critical in vehicle lateral stabilization. The weights can be adjusted according to specific situations.

In summary, by partitioning the control system into three stages (i.e. virtual inputs generation, control allocation, and actuator command tracking), a high degree of modularization is allowed. The generation of the virtual effort is targeted at meeting the overall motion control objectives. The control allocation scheme seeks to fulfill the virtual control effort within physical limits and commands desired slip ratios and slip angles to underlying actuator controllers. This modularized structure provides a flexible and integrated strategy for vehicle dynamics control design.

5.2 Model Predictive Supervisory Control

5.2.1 Introduction to Model Predictive Control

Model Predictive Control [87] is chosen as the design approach for the supervisory controller in this chapter. MPC is a multivariable control scheme that has been in practical use in the process control industries (for instance, power plants and petroleum refineries) since the 1980s. Since the last decade, MPC technology has been applied in a wide variety of fields, including food processing, automotive, and aerospace engineering [88, 89]. In MPC, plant models are used to predict the responses (i.e. outputs) of a dynamical system under inputs. The model predictive controller uses the models and current measurements to determine optimal future control inputs that minimize a cost function over the prediction horizon, while accommodating state and/or input constraints.

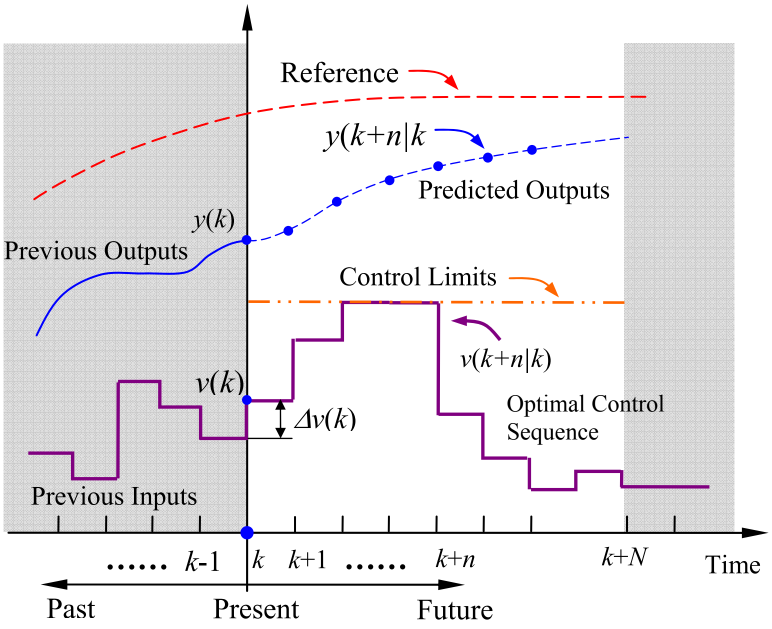

Figure 5.2: Model predictive control approach

As illustrated in Figure 5.2, at any time step k the plant states are sampled and a cost-minimizing control sequence is derived for a future time horizon: $[k,\ k + N]$.

Typically, the online computation scheme explores state trajectories that emanate from the current states to find a cost-minimizing control sequence $v(k+n|k)$ over the horizon. Only the first step of the control sequence is applied to the plant. In the next time step, the states are sampled again and the computations are repeated with the updated states. The prediction horizon keeps moving forward, and for this reason MPC is commonly referred as receding horizon control [90].

The success of Model Predictive Control in industrial applications is attributed to its advantages in several aspects. First, it naturally handles multivariable control problems. Secondly, it incorporates constraints on control inputs and states in a structured way, and can operate close to the constraint boundaries to achieve better performance. Thirdly, MPC scheme can be interpreted as simultaneous synthesis of feedback and feedforward controls. The feedback part is achieved by utilizing measured/estimated states and outputs, and the feedforward part is achieved by the prediction of the future outputs and their comparison with the reference.

Rawlings [91] provides a comprehensive introductory tutorial regarding theoretical and practical issues associated with MPC approach. A treatment of sufficient stability conditions can be found in the survey paper of Mayne [92]. Much academic research has been conducted to find efficient methods of numerical solution of MPC, to understand the stability properties of its local optimization, and in general to improve the MPC method [93]. Despite the fact many real processes are nonlinear, linear MPC approaches are used in the majority of applications with the feedback mechanism of the MPC compensating for prediction errors due to model mismatch. Unconstrained linear MPC relies on a series of direct matrix algebra calculations that are fast and robust. Constrained linear MPC is solved by using appropriate numerical solvers, such as a quadratic programming (QP) solver, because the optimal control of the quadratic cost function may be infeasible due to the constraints [94, 95].

MPC has recently gained popularity in the automotive control community. Typically a vehicle model is built, and control objectives and constraints on control inputs are converted into quadratic programming structure. Successful applications in automotive systems can be found in traction control [96], active steering control [97], lateral stabilization [98], emergency lane change [99, 100], and rollover prevention [101].

In this work, a linear parameter-varying vehicle model will be used, and the total tire forces and the yaw moment will be chosen as the control inputs at this level. After these virtual control efforts are determined by the MPC scheme, they will be further allocated to individual wheels so that physical control commands can be generated.

5.2.2 Vehicle Modeling for Supervisory Control Design

It is essential to develop a dynamic model that describes the vehicle motion with sufficient accuracy, and possesses a structure suitable for the MPC controller design, because modeling complexity and computational load are both crucial factors for the optimization.

The yaw plane vehicle dynamics is shown in Figure 5.3 with eight planar tire force components. The relationships between these tire forces and the three resultant generalized forces are:

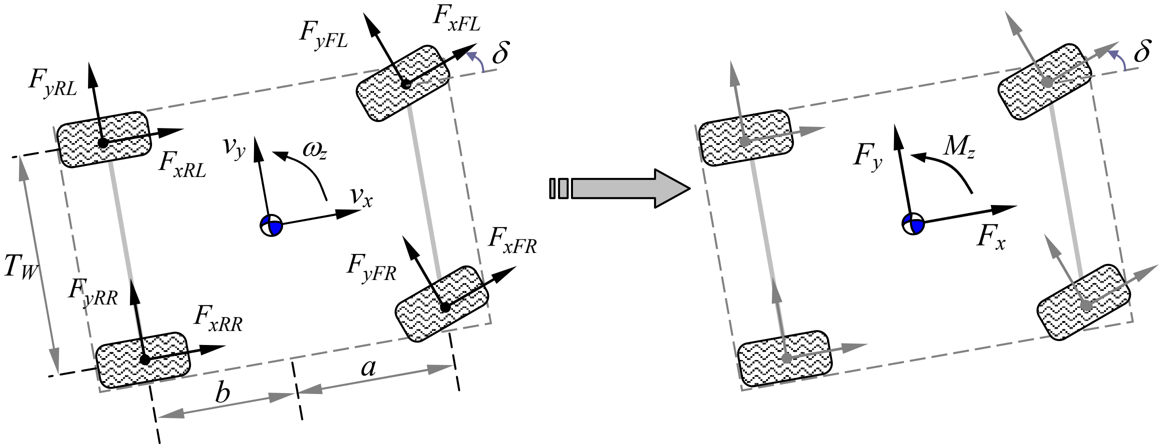

Figure 5.3: Individual tire forces and resultant total ground forces and the yaw moment

$$\begin{aligned} F_x = {} & F_{xFL}\cos\delta_{FL} - F_{yFL}\sin\delta_{FL} + F_{xFR}\cos\delta_{FR} - F_{yFR}\sin\delta_{FR} + \\ & F_{xRL}\cos\delta_{RL} - F_{yRL}\sin\delta_{RL} + F_{xRR}\cos\delta_{RR} - F_{yRR}\sin\delta_{RR} \end{aligned} \tag{5.1}$$

$$\begin{aligned} F_y = {} & F_{xFL}\sin\delta_{FL} + F_{yFL}\cos\delta_{FL} + F_{xFR}\sin\delta_{FR} + F_{yFR}\cos\delta_{FR} + \\ & F_{xRL}\sin\delta_{RL} + F_{yRL}\cos\delta_{RL} + F_{xRR}\sin\delta_{RR} + F_{yRR}\cos\delta_{RR} \end{aligned} \tag{5.2}$$

$$\begin{aligned} M_z = &\frac{T_w}{2}\left(-F_{xFL}\cos\delta_{FL} + F_{yFL}\sin\delta_{FL} - F_{xRL}\cos\delta_{RL} + F_{yRL}\sin\delta_{RL}\right) + \\ &\frac{T_w}{2}\left(F_{xFR}\cos\delta_{FR} - F_{yFR}\sin\delta_{FR} + F_{xRR}\cos\delta_{RR} - F_{yRR}\sin\delta_{RR}\right) + \\ &a\cdot\left(F_{xFL}\sin\delta_{FL} + F_{yFL}\cos\delta_{FL} + F_{xFR}\sin\delta_{FR} + F_{yFR}\cos\delta_{FR}\right) - \\ &b\cdot\left(F_{xRL}\sin\delta_{RL} + F_{yRL}\cos\delta_{RL} + F_{xRR}\sin\delta_{RR} + F_{yRR}\cos\delta_{RR}\right) \end{aligned} \tag{5.3}$$

where the steering angles are denoted for the tires to keep the independent active steering option open. Other external forces acting on the vehicle body (e.g. aerodynamic forces) are ignored. Applying Newton's second law of motion to the free body diagram, the equations of motion for vehicle's lateral and yaw dynamics can be written as

$$M(\dot{v}_y + v_x\omega_z) = F_y \text{ and } I_{zz}\dot{\omega}_z = M_z \tag{5.4}$$

The system, which ignores the longitudinal dynamics, contains two states and two inputs:

$$\begin{pmatrix} \dot{v}_y \\ \dot{\omega}_z \end{pmatrix} = \begin{pmatrix} 0 & -v_x \\ 0 & 0 \end{pmatrix}\begin{pmatrix} v_y \\ \omega_z \end{pmatrix} + \begin{pmatrix} \frac{1}{M} & 0 \\ 0 & \frac{1}{I_{zz}} \end{pmatrix}\begin{pmatrix} F_y \\ M_z \end{pmatrix},\ \mathbf{x} = \begin{pmatrix} v_y \\ \omega_z \end{pmatrix} \tag{5.5}$$

It can be treated as a linear parameter-varying system

$$\dot{\mathbf{x}} = A_c\left(v_x\right)\mathbf{x} + B_c\mathbf{v}, \tag{5.6}$$

with virtual control efforts $\mathbf{v} = \begin{pmatrix} F_y & M_z \end{pmatrix}^T$. In general, the vector of generalized force should contain three components $\mathbf{v} = \begin{pmatrix} F_x & F_y & M_z \end{pmatrix}^T$. For obstacle avoidance scenarios [102], the desired total longitudinal force F_x may be specified, whereas for vehicle lateral stabilization, we are mainly concerned about the regulation/tracking of vehicle's lateral and yaw motions. In the rest of this chapter, the virtual control will consists of only F_y and M_z as in Eq. (5.5).

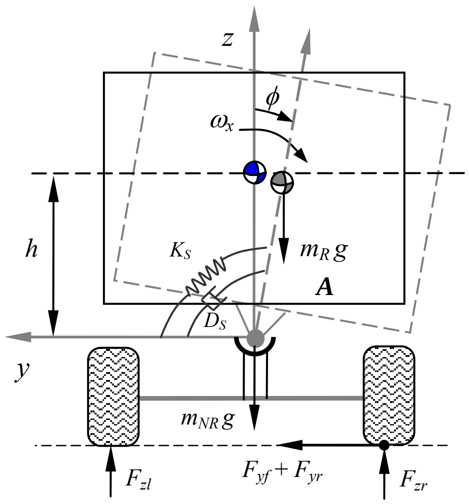

Figure 5.4: Rear view of the vehicle model with sprung mass roll motion

If the roll motion of vehicle sprung mass needs to be factored in (see Figure 5.4), the dynamic equations can be derived by treating tire forces as a whole and including the coupling between yaw and roll.

$$M(\dot{v}_y + v_x\omega_z) - m_R h\dot{\omega}_x = F_y \tag{5.7}$$

$$I_{zz}\dot{\omega}_z = M_z \tag{5.8}$$

$$I_{xxs}\dot{\omega}_x - m_R(\dot{v}_y + v_x\omega_z)h = m_R gh\phi - D_s\omega_x - K_s\phi \tag{5.9}$$

After substitutions and reductions, it can be shown that

$$\dot{v}_y = -v_x\omega_z + \frac{m_R h\left(m_R gh - K_s\right)}{m_e I_{xxs}}\phi - \frac{m_R hD_s}{m_e I_{xxs}}\omega_x + \frac{F_y}{m_e} \tag{5.10}$$

$$\dot{\omega}_x = \frac{m_R gh - K_s}{I_e}\phi - \frac{D_s}{I_e}\omega_x + \frac{m_R h}{MI_e}F_y \tag{5.11}$$

where $m_e = M - \frac{m_R^2 h^2}{I_{xxs}}$ and $I_e = I_{xxs} - \frac{m_R^2 h^2}{M}$. By adding two more states ϕ and ω_x, the model contains four state variables, and the roll dynamics can be simulated:

$$\begin{pmatrix} \dot{v}_y \\ \dot{\omega}_z \\ \dot{\phi} \\ \dot{\omega}_x \end{pmatrix} = \begin{pmatrix} 0 & -v_x & \frac{m_R h\left(m_R gh - K_s\right)}{m_e I_{xxs}} & \frac{-m_R hD_s}{m_e I_{xxs}} \\ 0 & 0 & 0 & 0 \\ 0 & 0 & 0 & 1 \\ 0 & 0 & \frac{m_R gh - K_s}{I_e} & \frac{-D_s}{I_e} \end{pmatrix} \begin{pmatrix} v_y \\ \omega_z \\ \phi \\ \omega_x \end{pmatrix} + \begin{pmatrix} \frac{1}{m_e} & 0 \\ 0 & \frac{1}{I_{zz}} \\ 0 & 0 \\ \frac{m_R h}{MI_e} & 0 \end{pmatrix} \begin{pmatrix} F_y \\ M_z \end{pmatrix}, \ \mathbf{x} = \begin{pmatrix} v_y \\ \omega_z \\ \phi \\ \omega_x \end{pmatrix} \tag{5.12}$$

5.2.3 Formulation of the Control Objective

Given a continuous-time state-space system Eqs. (5.5) or (5.12), one can discretize it to obtain the discrete model

$$\mathbf{x}_{k+1} = A\mathbf{x}_k + B\mathbf{v}_k \tag{5.13}$$

A sampling time of $T_s = 0.01$ s will be used for later computations. One can further obtain the n-step prediction model:

$$\mathbf{x}_{k+n} = A^n\mathbf{x}_k + A^{n-1}B\mathbf{v}_k + A^{n-2}B\mathbf{v}_{k+1} + \cdots + AB\mathbf{v}_{k+n-2} + B\mathbf{v}_{k+n-1} \tag{5.14}$$

Namely, the states at a future instant are dependent on the current states and the sequence of current and future inputs up to that instant. Disturbance inputs can also be included if they are predicted or estimated. The sequence of future predictions up to n-step ahead can be shown as:

$$\begin{bmatrix} \mathbf{x}_{k+1} \\ \mathbf{x}_{k+2} \\ \mathbf{x}_{k+3} \\ \vdots \\ \mathbf{x}_{k+n} \end{bmatrix} = \begin{bmatrix} A \\ A^2 \\ A^3 \\ \vdots \\ A^n \end{bmatrix} \mathbf{x}_k + \begin{bmatrix} B & 0 & 0 & \cdots & 0 \\ AB & B & 0 & \cdots & 0 \\ A^2B & AB & B & 0 & 0 \\ \vdots & \vdots & \vdots & \ddots & \vdots \\ A^{n-1}B & A^{n-2}B & \cdots & AB & B \end{bmatrix} \begin{bmatrix} \mathbf{v}_k \\ \mathbf{v}_{k+1} \\ \mathbf{v}_{k+2} \\ \vdots \\ \mathbf{v}_{k+n-1} \end{bmatrix} \tag{5.15}$$

To make the notation more compact, we stack up state vectors and control vectors by denoting $\underset{\rightarrow k}{\mathbf{x}} \equiv \begin{bmatrix} \mathbf{x}_{k+1} \\ \mathbf{x}_{k+2} \\ \vdots \end{bmatrix}$ and $\underset{\rightarrow k-1}{\mathbf{v}} \equiv \begin{bmatrix} \mathbf{v}_k \\ \mathbf{v}_{k+1} \\ \vdots \end{bmatrix}$ [103]. Consequently Eq. (5.15) can be written in a compact form by assigning symbols to the state and input matrices.

$$\underset{\rightarrow k}{\mathbf{x}} = P_x\mathbf{x}_k + H\underset{\rightarrow k-1}{\mathbf{v}} . \tag{5.16}$$

The cost function is defined as the summation of weighted state deviation sequence from reference **r** and weighted control input sequence.

$$J = \sum_{i=1}^{n_x} \mathbf{e}_{k+i}^T Q \mathbf{e}_{k+i} + \sum_{i=0}^{n_u} \mathbf{v}_{k+i}^{\mathbf{T}} R \mathbf{v}_{k+i} . \tag{5.17}$$

where $\mathbf{e}_{k+i} = \mathbf{x}_{k+i} - \mathbf{r}_{k+i}$. For regulation problems, the desired states are zero (**r** = **0**). Additionally, assume that the same horizon (N) is used for both the state prediction and the future inputs, the cost function becomes

$$J = \sum_{i=1}^{N+1} \mathbf{x}_{k+i}^T Q \mathbf{x}_{k+i} + \sum_{i=0}^{N} \mathbf{v}_{k+i}^{\mathbf{T}} R \mathbf{v}_{k+i} . \tag{5.18}$$

The control objective is to minimize this cost function J with respect to future control sequence,

$$\min_{\underset{\to}{\mathbf{v}}} J = \left(\underset{\to k}{\mathbf{x}}\right)^T \begin{bmatrix} Q & 0 & \cdots & 0 \\ 0 & Q & \cdots & 0 \\ \vdots & \vdots & \ddots & \vdots \\ 0 & \cdots & 0 & Q \end{bmatrix} \underset{\to k}{\mathbf{x}} + \left(\underset{\to k-1}{\mathbf{v}}\right)^T \begin{bmatrix} R & 0 & \cdots & 0 \\ 0 & R & \cdots & 0 \\ \vdots & \vdots & \ddots & \vdots \\ 0 & \cdots & 0 & R \end{bmatrix} \underset{\to k-1}{\mathbf{v}} . \tag{5.19}$$

After substitutions, the objective is denoted as

$$\min_{\underset{\to}{\mathbf{v}}} J = \left(P_x \mathbf{x}_k + H \underset{\to k-1}{\mathbf{v}} \right)^T \mathbf{Q} \left(P_x \mathbf{x}_k + H \underset{\to k-1}{\mathbf{v}} \right) + \left(\underset{\to k-1}{\mathbf{v}} \right)^T \mathbf{R} \left(\underset{\to k-1}{\mathbf{v}} \right) . \tag{5.20}$$

One can expand the expression and collect similar terms,

$$\min_{\underset{\to}{\mathbf{v}}} J = \underset{\to}{\mathbf{v}}^T \left(H^T \mathbf{Q} H + \mathbf{R} \right) \underset{\to}{\mathbf{v}} + 2 \underset{\to}{\mathbf{v}}^T H^T \mathbf{Q} P_x \mathbf{x}_k + \left(P_x \mathbf{x}_k \right)^T \mathbf{Q} P_x \mathbf{x}_k . \tag{5.21}$$

Since the last term on the right hand side does not contain the optimization variables, it can be dropped. More compactly, the objective is formulated in a standard quadratic form

$$\min_{\underset{\to}{\mathbf{v}}} J = \underset{\to}{\mathbf{v}}^T \mathbf{S} \underset{\to}{\mathbf{v}} + 2 \underset{\to}{\mathbf{v}}^T \mathbf{f} . \tag{5.22}$$

5.2.4 Constraint Handling

In order to generate realistic total forces and yaw moment, constraints on the magnitudes and rates of change of control signals should be considered. Suppose the control inputs are subject to upper and lower saturation limits $\underline{\mathbf{v}} \le \mathbf{v} \le \bar{\mathbf{v}}$. Impose linear inequality constraints on the whole control sequence,

$$\begin{bmatrix} \underline{\mathbf{v}} \\ \underline{\mathbf{v}} \\ \vdots \\ \underline{\mathbf{v}} \end{bmatrix} \le \begin{bmatrix} \mathbf{v}_k \\ \mathbf{v}_{k+1} \\ \vdots \\ \mathbf{v}_{k+N} \end{bmatrix} \le \begin{bmatrix} \bar{\mathbf{v}} \\ \bar{\mathbf{v}} \\ \vdots \\ \bar{\mathbf{v}} \end{bmatrix}, \text{ or } \begin{cases} \underset{\to k-1}{\mathbf{v}} \le \bar{V} \\ -\underset{\to k-1}{\mathbf{v}} \le -\underline{V} \end{cases}, \tag{5.23}$$

which can be represented in terms of a single set of linear inequalities

$$\begin{bmatrix} \mathbf{I} \\ -\mathbf{I} \end{bmatrix} \underset{\to}{\mathbf{v}} \le \begin{bmatrix} \bar{V} \\ -\underline{V} \end{bmatrix}, \tag{5.24}$$

where $\mathbf{I}$ is an identity matrix with appropriate dimensions. As for the rate limits, since $\mathbf{v}_k = \Delta \mathbf{v}_k + \mathbf{v}_{k-1}$, the relationship between control inputs sequence and control increments sequence is

$$\underset{\rightarrow k-1}{\mathbf{v}} = C_{I/\Delta}\cdot \underset{\rightarrow k-1}{\Delta\mathbf{v}} + E'\cdot \mathbf{v}_{k-1}\text{, or } \underset{\rightarrow k-1}{\Delta\mathbf{v}} = C_{\Delta}\cdot \underset{\rightarrow k-1}{\mathbf{v}} - E\cdot \mathbf{v}_{k-1}\text{,} \tag{5.25}$$

where $C_{I/\Delta} = \begin{bmatrix} I & 0 & 0 & \cdots & 0 \\ I & I & 0 & \cdots & 0 \\ I & I & I & \cdots & 0 \\ \vdots & \vdots & \vdots & \vdots & \vdots \\ I & I & I & \cdots & I \end{bmatrix}$, $E' = \begin{bmatrix} I \\ I \\ \vdots \\ I \end{bmatrix}$, $C_{\Delta} = \begin{bmatrix} I & 0 & 0 & \cdots & 0 \\ -I & I & 0 & \cdots & 0 \\ 0 & -I & I & \cdots & 0 \\ \vdots & \vdots & \ddots & \ddots & \vdots \\ 0 & 0 & 0 & \cdots & I \end{bmatrix}$, and $E = \begin{bmatrix} I \\ 0 \\ \vdots \\ 0 \end{bmatrix}$. Suppose the lower and upper limits of the control increments sequence are $\Delta\underline{V} \le \underset{\rightarrow}{\Delta\mathbf{v}} \le \Delta\overline{V}$, namely $\Delta\underline{V} \le C_{\Delta}\cdot \underset{\rightarrow}{\mathbf{v}} - E\cdot \mathbf{v}_{k-1} \le \Delta\overline{V}$. After rearrangements one obtains

$$\begin{bmatrix} C_{\Delta} \\ -C_{\Delta} \end{bmatrix} \underset{\rightarrow}{\mathbf{v}} \le \begin{bmatrix} \Delta\overline{V} + E\cdot \mathbf{v}_{k-1} \\ -\Delta\underline{V} - E\cdot \mathbf{v}_{k-1} \end{bmatrix}. \tag{5.26}$$

The MPC problem can now be cast into a standard quadratic programming form,

$$\min_{\underset{\rightarrow}{\mathbf{v}}} J = \underset{\rightarrow}{\mathbf{v}}^{T} S \underset{\rightarrow}{\mathbf{v}} + 2\underset{\rightarrow}{\mathbf{v}}^{T}\mathbf{f}\text{, subject to } Lh\,\underset{\rightarrow}{\mathbf{v}} \le Rh \tag{5.27}$$

where the matrices *Lh* and *Rh* consist of the linear constraints in Eqs. (5.24) and (5.26). The routine "`quadprog`" in the MATLAB Optimization Toolbox can be called to solve this standard problem [104]. Adjustable parameters for optimization design include weights on states (*Q*), weights on inputs (*R*), and prediction window length (*N*). By adjusting the weights on states, trade-offs among lateral, yaw or roll responses and control efforts can be manipulated.

After the optimal virtual control sequence $\underset{\rightarrow k-1}{\mathbf{v}}$ is found, only its first-step is used, namely v_k^{*}. Given road friction, tire vertical loads, and the vehicle states, the virtual controls can be attained through changing planar tire forces F_{xi} and F_{yi}, which are in turn affected by tire longitudinal slip ratios and slip angles $u = \begin{pmatrix} \lambda_{FL} & \lambda_{FR} & \lambda_{RL} & \lambda_{RR} & \alpha_{FL} & \alpha_{FR} & \alpha_{RL} & \alpha_{RR} \end{pmatrix}^{T}$. If independent braking is the only actuation mechanism, the control inputs are reduced to $u = \begin{pmatrix} \lambda_{FL} & \lambda_{FR} & \lambda_{RL} & \lambda_{RR} \end{pmatrix}^{T}$.

5.3 Control Allocation Scheme

5.3.1 Control Allocation in Automotive Applications

The same virtual control input can be produced by different combinations of actuators on a vehicle. In many cases, the number of effectors available exceeds the number of states to be controlled. For instance, both differential braking and active steering can generate a specific yaw moment to rotate the vehicle. In that sense, the vehicle is an over-actuated system. Control allocation (CA) of over-actuated systems involves generating an optimal set of actuation commands that produce the effect dictated by the virtual control input as closely as possible, while satisfying the saturation and rate constraints of the effectors and minimizing the actuator effort.

Mathematically, a control allocation algorithm solves an under-determined, typically constrained, set of equations. Given the total virtual control effort $v(t) \in \mathrm{R}^n$ requested by the supervisory stage, the allocator determines the true control input $u(t) \in \mathrm{R}^m$, where $m > n$. In other words, it solves the relationship

$$G\big(u(t)\big) = v(t), \tag{5.28}$$

where $G:\mathbb{R}^m \mapsto \mathbb{R}^n$ is the mapping from the true to the virtual control input. For the linear case, this mapping becomes

$$B \cdot u(t) = v(t), \tag{5.29}$$

where the control effectiveness matrix B is an $n \times m$ matrix with rank n. Typically the true control is also subject to upper and lower bounds $u^- \le u \le u^+$.

Practically for the vehicle handling control case, given a commanded yaw moment M_d from the supervisory controller, the goal of the control allocation module is to deliver an actual yaw moment $M \approx M_d$ by requesting the appropriate slip ratios and slip angles from each of the four wheels. Obviously there are surplus degrees of freedom in this problem formulation. In particular, it makes sense to apply slip ratios as small as possible, so the secondary objective is to find the set of feasible actual controls with the least norm.

From the discussions above, the control allocation problem can be posed as a constrained optimization problem. In some studies, solutions to the CA problem have been found with the pseudo-inverse approach [105 , 106], which can be easily implemented and computationally efficient. However, pseudo-inverse based control allocation fails to factor in actuator limitations directly and could lead to unrealistic solutions violating the physical bounds.

The control allocation problem is formulated as a linear programming (LP) problem in [107]. The LP approach minimizes a linear performance index subject to linear constraints, thus reduces the optimization problem to solving a set of linear algebraic equations iteratively. Linear inequality constraints are used to ensure that constraints on actuators are not violated. However, since the approach here does not consider the actual generation at the actuator level, it cannot be applied to the slip-allocation case. In [85] the authors used quadratic programming together with a linear quadratic regulator to track a desired yaw rate trajectory while minimizing sideslip. However, since this approach does not consider the actual generation at the actuator level either, it cannot be applied to the slip-allocation case. The control allocation problem in [108] is addressed by designing an approximation to the optimal solution based on multi-parametric nonlinear programming (mp-NLP). The proposed approach was successfully applied to a lateral stabilization maneuver. Since its optimization scheme still heavily relied on the nonlinear formulation of the tire model, it is possible to improve computational efficiency if the linearized approximation of the tire behaviour is feasible. In [86] an accelerated fixed-point (AFP) method is proposed to solve the constrained quadratic programming control allocation problem. Faster convergence rate was achieved with both linearized approximation of the tire characteristics and the computationally efficient control allocation scheme.

5.3.2 The Control Allocation Problem

The solution set of a linear control allocation problem is given by the intersection between the hyperplane $Bu = v$ and the constraints in the hypercube $u^- \le u \le u^+$. Since both of them are convex, the solution set will be convex too. Therefore, this optimization problem has three possible outcomes: (1) there are an infinite number of solutions; (2) there is one unique solution; and (3) no solution exists.

In case (1), there is an additional degree of freedom in choosing the actual control inputs while satisfying the constraints and meeting the objective. This freedom can be used to optimize secondary objectives such as minimum use of control inputs. In case (2), since there is one unique admissible control input, the task for control allocation is to find this solution. In case (3), the desired virtual control input cannot be achieved, and one cannot find a solution without violating constraints. This is accomplished by settling for a different value of v that is attainable, so that the produced control input approximates v well in some sense, for instance, the norm $\|Bu - v\|$ is minimized.

Figure 5.5 illustrates the three cases with an intuitive numerical example. For easy visualization, the dimension of the virtual control is chosen as one and that of the true controls is two. Suppose the control effectiveness matrix B is [1, 2], then the three bold lines represent various virtual control demands (2.0, 1.5, and 1.0). The three arcs are level contours in l_2-norm. The box in Figure 5.5 represents the constraints on true controls ($0.7 \le x_1 \le 1.5$ and $0.4 \le x_2 \le 1.0$). Since the problem has two optimization variables, the constraints take the shape of a rectangle. For higher dimensions, the constraint region will be a hypercube.

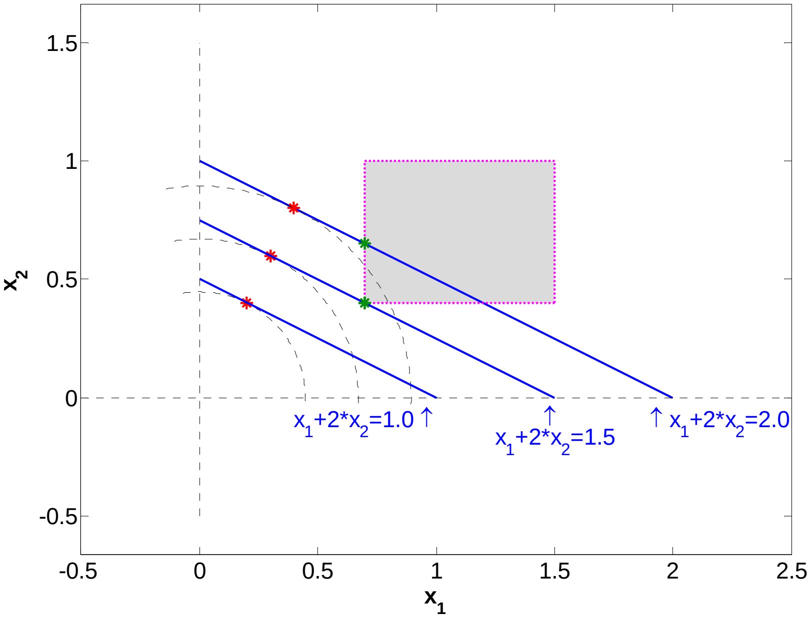

Figure 5.5: Three cases for the linear allocation problem with box constraints

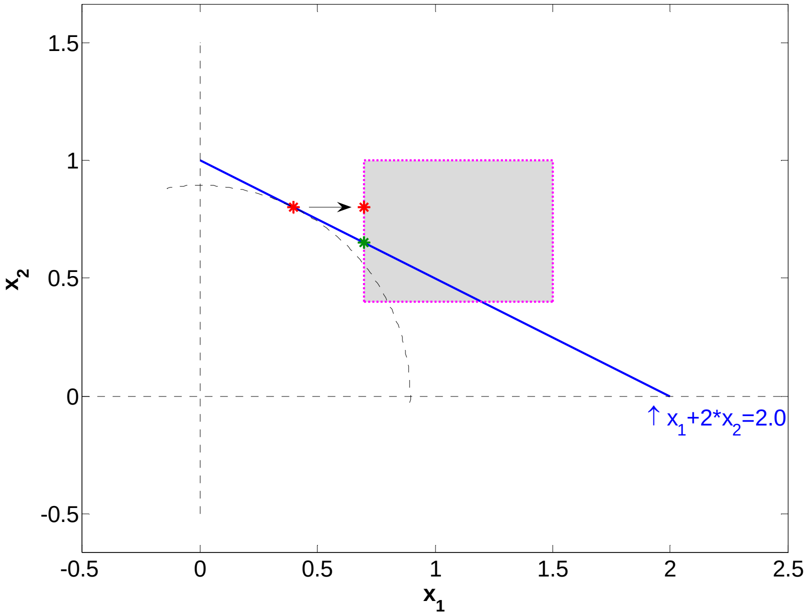

Figure 5.6: Comparison among pseudo-inverse, clipped pseudo-inverse, and constrained least-square solutions to a linear allocation problem

The virtual control demand v = 2.0 corresponds to Case (1). By performing a pseudo-inverse, it is straightforward to find the unconstrained optimal solution with the least l_2-norm: [0.4, 0.8], which is obviously outside the admissible region. The true optimal solution is [0.7, 0.65] located on the boundary.

The virtual control demand v = 1.5 corresponds to Case (2). By performing a pseudo-inverse, the unconstrained optimal solution with the least l_2-norm: [0.3, 0.6], which is inadmissible. In fact, there exists a unique feasible solution: [0.7, 0.4], and it is located on the vertex.

The virtual control demand v = 1.0 corresponds to Case (3). By performing a pseudo-inverse, the unconstrained optimal solution with the least l_2-norm: [0.2, 0.4]. No feasible solution can be found for this case. The best approximate solution is still the vertex point [0.7, 0.4].

The numerical example above also illustrates an important fact: the clipped optimal solution is not necessarily the optimal constrained solution. Figure 5.6 shows the comparison among three solutions for Case (1) mentioned above. The pseudo-inverse solution was found at [0.4, 0.8]. Since it is infeasible despite optimality, one clipped it with constraints and obtained the new solution at [0.7, 0.8], which is neither optimal nor smaller in l_2-norm. A successful allocation algorithm should be able to find the true constrained optimal solution at [0.7, 0.65].

Motivation by the example above, the control allocation is formulated as a minimal least squares (LS) problem in this work,

$$u^* = \arg\min_{u \in \Omega} \|u\| \text{ and } \Omega = \arg\min_{u^- \le u \le u^+} \left\| W_v \left(Bu - v_k^* \right) \right\|, \tag{5.30}$$

where the least 2-norm solution is chosen if $\left\| W_v \left(Bu - v_k^* \right) \right\|$ does not have a unique feasible solution. The weighting matrix W_v is used to impose appropriate weights on components in the virtual control vector to favor certain objectives. The default weighting matrix is an identity matrix with compatible dimensions.

Equality-constrained least squares problems can be solved analytically through matrix manipulations by adding a correction term to the pseudo-inverse solution [109]. The inequality-constrained least squares problems, or to be more exact, "bound-constrained LS" problem has been discussed much in literature and for various applications [110, 111]. Several classes of optimization algorithms can be applied to solve it, such as active-set method and interior-point method. In the active-set method, certain constraints are regarded as equalities while the rest are temporarily disregarded. The method adjusts this equality set in order to identify the correct active constraint set at the optimal solution [112]. In this work, the routine "`lsqlin`" in the Matlab Optimization Toolbox is used The numerical algorithm behind this routine is based on the work in [113].

In summary, the control allocation scheme can be employed to optimally distribute the desired virtual control input among available actuators, in order to achieve certain desired control objectives. Besides the capability to accommodate actuation constraints and to prioritize control targets, control allocation enables the natural reconfiguration of the control system even if actuator degradation or failure occurs, so that the best possible desired performance can still be maintained with the remaining actuators, without redesigning the control law. With the increasing number of motion actuators in future vehicle configurations, the control allocation optimization may also be useful to X-by-wire vehicles as well as electric vehicles with in-hub motors.

5.3.3 Optimal Allocation of Tire Forces

At each sampling instant t_k, $v_k^* = \begin{pmatrix} F_y & M_z \end{pmatrix}^T$ is computed by the MPC controller at the supervisory stage to accomplish vehicle handling tasks as derived in Section 5.2.4. Starting with the assumption that individual wheel braking is the only available actuating mechanism, $u_k = \begin{pmatrix} \lambda_{FL} & \lambda_{FR} & \lambda_{RL} & \lambda_{RR} \end{pmatrix}^T$ are the control inputs to be determined at this stage.

The objective of optimal allocation is to manipulate u_k so that the nonlinear mapping $v_k^* = G(\zeta, u_k)$ can be attained, where ζ refers to accessible parameters and variables, such as tire vertical loads, tire model fitting parameters, and so on. By first-order Taylor series expansion, the nonlinear function is locally approximated with an affine function at each sampling instant.

$$v_k^* = G(\zeta, u_k) \approx G(\zeta, u_{k-1}) + \left.\frac{\partial G}{\partial u}\right|_{k-1} \cdot (u_k - u_{k-1}) \tag{5.31}$$

Let $\tilde{v}_k = v_k^* - G(\zeta, u_{k-1}) + \left.\frac{\partial G}{\partial u}\right|_{k-1} \cdot u_{k-1}$ and $\mathbf{T}(\zeta, u_{k-1}) = \left.\frac{\partial G(\zeta, u)}{\partial u}\right|_{k-1}$, then Eq. (5.31) is reduced to solving for u_k so that the following linear mapping is satisfied in the least-square sense,

$$\tilde{v}_k = \mathbf{T}(\zeta, u_{k-1}) \cdot u_k \,. \tag{5.32}$$

The 3×4 Jacobian matrix is denoted by

$$\frac{\partial G(\zeta, u)}{\partial u} = \begin{pmatrix} \frac{\partial F_x}{\partial u} & \frac{\partial F_y}{\partial u} & \frac{\partial M_z}{\partial u} \end{pmatrix}^T, \tag{5.33}$$

where $\frac{\partial F_x}{\partial u} = \begin{pmatrix} \frac{\partial F_{xFL}}{\partial \lambda_{FL}} \cos\delta_{FL} - \frac{\partial F_{yFL}}{\partial \lambda_{FL}} \sin\delta_{FL}, & \frac{\partial F_{xFR}}{\partial \lambda_{FR}} \cos\delta_{FR} - \frac{\partial F_{yFR}}{\partial \lambda_{FR}} \sin\delta_{FR}, \\ \frac{\partial F_{xRL}}{\partial \lambda_{RL}} \cos\delta_{RL} - \frac{\partial F_{yRL}}{\partial \lambda_{RL}} \sin\delta_{RL}, & \frac{\partial F_{xRR}}{\partial \lambda_{RR}} \cos\delta_{RR} - \frac{\partial F_{yRR}}{\partial \lambda_{RR}} \sin\delta_{RR} \end{pmatrix}$. Both $\frac{\partial F_y}{\partial u}$ and $\frac{\partial M_z}{\partial u}$ are also 1×4 row vectors and can be derived easily, as long as all partial derivative terms $\frac{\partial F_{xi}}{\partial \lambda_i}$ and $\frac{\partial F_{yi}}{\partial \lambda_i}$ are available. A tire model has to be chosen and parameterized to serve the purpose. In this study, the Magic Formula tire model for combined longitudinal and lateral slips detailed later in Section 5.5 will be adopted.

With the necessary variables measured (such as ω_z, a_y, and δ_i) or estimated (such as v_y and F_{zi}), the entries in the Jacobian matrix can be populated. Then one can solve the optimal allocation problem as a standard constrained linear least-square problem

$$\min_{u_k} \left\| \mathbf{T} \cdot u_k - \tilde{v}_k \right\|_2^2 \text{, subject to } \underline{u} \le u_k \le \overline{u} \,. \tag{5.34}$$

In other words, this optimal allocation problem is equivalent to solving the under-determined linear equations $\mathbf{T} \cdot u_k = \tilde{v}_k$ in the least-squares sense subject to possible inequality constraints. Because the optimization problem being solved is convex, there exists a global, not necessarily unique, solution. The optimal solution with the least l_2-norm will be chosen, since excessive wheel slip ratios are not desired.

In order to include constraints on the optimization variables, first consider the saturation limits. Since individual braking is the intended actuating mechanism, $-1 \le u_i \le 0$ (i = FL, FR) applies to the front axle to allow for wheel lock-ups, and $-0.2 \le u_i \le 0$ (i = RL, RR) applies to the rear axle to prevent wheel lock-ups. If individual wheel traction control is at disposal, the upper bounds of the constraints can be extended to positive ranges. In addition, rate limits should be imposed on slip ratio commands to avoid changing instantaneously or unrealistically fast. For each component in the vector u_k,

$$\left| \frac{u_k - u_{k-1}}{\mathit{\Delta} T} \right| \le \text{RateLim} \,, \tag{5.35}$$

where $\mathit{\Delta} T = t_k - t_{k-1}$. Therefore $\underline{u} = \max\left(\text{-1 or -0.2, } -\mathit{\Delta} T \cdot \text{RateLim} + u_{k-1}\right)$ and $\overline{u} = \min\left(0,\ \mathit{\Delta} T \cdot \text{RateLim} + u_{k-1}\right)$. If different priorities are assigned to attain F_y and M_z, a diagonal matrix W_λ can be used to impose appropriate weights on them. The default weighting matrix is a 2-by-2 identity matrix. In the end, the problem becomes

$$u_k = \arg\min_{u \in \Omega} \left\| u \right\|_2^2 \text{ and } \Omega = \arg \min_{\underline{u} \le u \le \overline{u}} \left\| W_\lambda \left(\mathbf{T} \cdot u - \tilde{v}_k \right) \right\|_2^2 . \tag{5.36}$$

5.4 Modeling of Tire Forces

The forces generated at the tire-ground-contact patches are the primary source of forces to affect vehicle motions. Therefore, a good understanding of the characteristics of tire forces is critical for vehicle response simulations, tire force estimation, and controller design.

5.4.1 Tire Longitudinal Forces

Given tire vertical load and tire-ground adhesion level, when a traction or braking torque is applied to a wheel, a traction or braking force is produced at the contact patch, and wheel hub speed (v_x) does not equal wheel circumferential speed. This phenomena is called tire longitudinal slip and is commonly quantified by the slip ratio (λ), which is defined as the normalized difference between wheel hub speed and wheel circumferential speed [50]. For a tire subject to braking, the slip ratio is

$$\lambda = \frac{R_w\omega - v_x}{v_x} = \frac{R_w\omega}{v_x} - 1\,, \tag{5.37}$$

and for a tire subject to traction,

$$\lambda = \frac{R_w\omega - v_x}{R_w\omega} = 1 - \frac{v_x}{R_w\omega}\,, \tag{5.38}$$

where ω is the tire rotational speed in rad/s and R_w is the tire effective rolling radius in meter. If there is no traction or braking torque applied, the wheel rolls with $\lambda = 0$. Under braking conditions, tire circumferential speed is lower than wheel hub speed, so $\lambda < 0$, whereas under traction conditions, tire circumferential speed is higher than wheel hub speed and thus $\lambda > 0$.

Tire longitudinal forces (either traction or braking forces) vary with tire slip ratios. Figure 5.7 shows a typical relationship between slip ratios and tire longitudinal forces subject to 5900 (N) vertical load on a road surface with an adhesion coefficient of 0.75, roughly the level on a dry concrete or asphalt road. When slip ratios are small, longitudinal force is mainly created by the elastic deformation of the tire tread, and its magnitude increases with slip ratio almost linearly. If the slip (in absolute value) increases further, tire tread sliding occurs and the relationship between longitudinal forces and slip ratios becomes nonlinear. Once the longitudinal force reaches its peak value, further increase of slip ratio leads to an unstable region where the longitudinal force diminishes with increasing slip, until the wheel locks up (λ = -1) or spins completely (λ = 1).

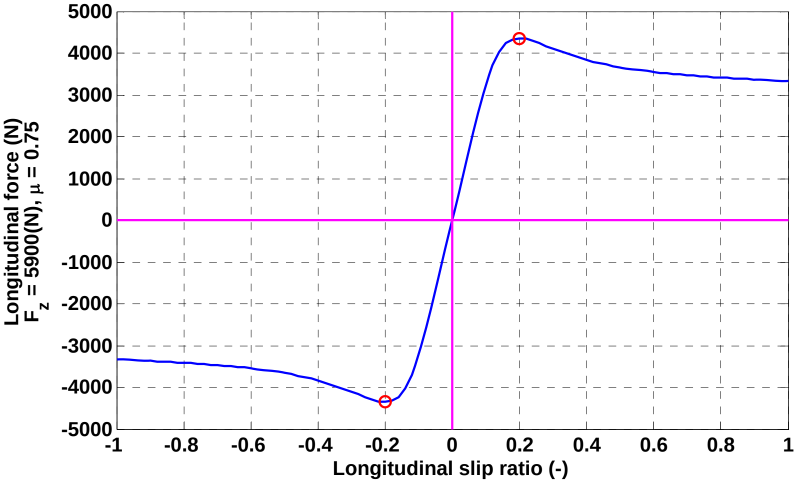

Figure 5.7: Tire longitudinal forces versus longitudinal slips (pure-slip case)

Tire longitudinal forces also vary with tire vertical load, tire-ground adhesion coefficient, and are coupled with tire lateral forces. In general, tire longitudinal forces decrease with decreasing vertical load and adhesion coefficient. The coupled relationship between tire longitudinal and lateral forces will be discussed in Section 5.4.3 later.

5.4.2 Tire Lateral Forces

When a tire is not traveling along the wheel plane, a lateral force will develop at the tire-road contact patch due to lateral tire deformation. Lateral force is a function of tire slip angle (α), i.e. the angle between tire heading direction and the velocity vector at the contact patch. The slip angle is a result of the compliance of the pneumatic tire, and also has a significant effect on the vehicle dynamics.

Similar to the relationship between tire longitudinal forces and slip ratios, Figure 5.8 shows a typical relationship between tire slip angles and lateral forces subject to 5900 (N) vertical load on a road surface with an adhesion coefficient of 0.75. It should be noted that the sign of the slip angle and the lateral force is opposite, consistent with the ISO sign convention and the definition used in the CarSim simulation package. When slip angles are small, lateral force is approximately a linear function of slip angle. After reaching a peak lateral force at a particular slip angle, it decreases with increasing slip angle.

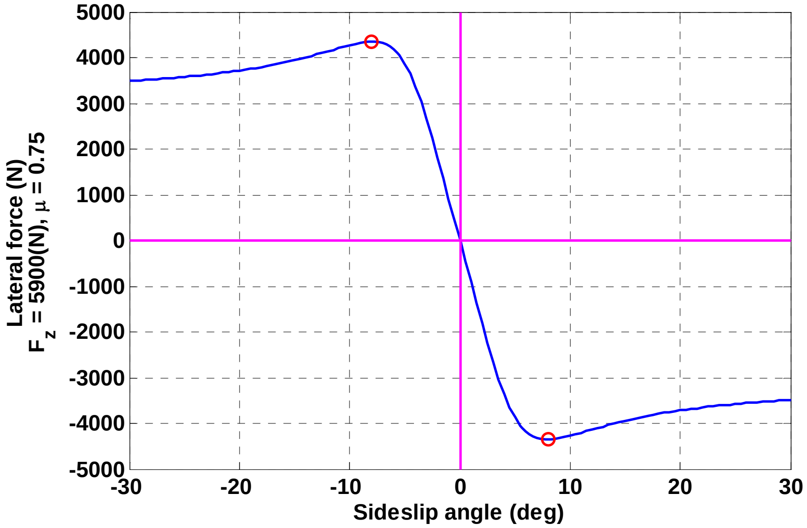

Figure 5.8: Tire lateral force versus tire slip angle (pure-slip case)

Tire lateral forces also vary with tire vertical load, tire-ground adhesion coefficient, and tire longitudinal force. In general, tire lateral forces decrease with decreasing vertical load and adhesion coefficient. The coupled relationship between tire lateral and longitudinal forces will be discussed in the Section 5.4.3 below.

5.4.3 Coupling between Tire Longitudinal and Lateral Forces

It is quite usual that a tire is generating longitudinal and lateral forces simultaneously, for instance, deceleration when cornering, or acceleration when overtaking. The coupling effects between tire longitudinal and lateral forces are crucial in the study on vehicle response simulations and controller design, especially when both tire slip ratio and slip angle are not negligible. The resultant tire force with combined slip ratio and slip angle are present is not a simple sum of pure-slip longitudinal and lateral forces. The attainable total tire forces are approximately contained by an enveloping curve, usually called friction circle or friction ellipse [114].

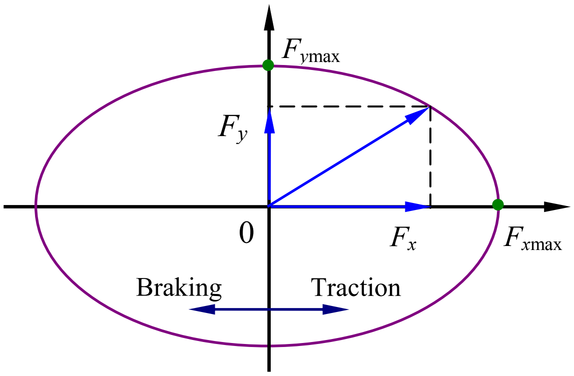

Figure 5.9: Concept of friction ellipse for tire longitudinal and lateral forces

Figure 5.9 illustrates the dependence and the limits of tire longitudinal and lateral forces conceptually. The resultant force is a vector sum of the two components and is contained inside the ellipse

$$\left(\frac{F_{xi}}{F_{x\max i}}\right)^2+\left(\frac{F_{yi}}{F_{y\max i}}\right)^2\le 1\,, \tag{5.39}$$

where $F_{x\max i}$ and $F_{y\max i}$ are the peak values in longitudinal and lateral directions. The maximum longitudinal and lateral forces correspond to pure-slip cases, and depend on the tire vertical load and tire-ground adhesion conditions.

A successful tire model needs to capture the dependence of the tire forces with sufficient accuracy on the slip ratio, slip angle, tire vertical load, adhesion condition, as well as the coupling between longitudinal and lateral components.

$$\begin{Bmatrix} F_x \\ F_y \end{Bmatrix} = f\left(\lambda, \alpha, F_z, \mu_R\right) \tag{5.40}$$

5.4.4 Tire Models

Due to the significance of tire forces for vehicle dynamics and control, it is desirable to use mathematical models to approximate the complex tire behaviors for the purposes of simulation and controller design. Significant research efforts have been dedicated to the development of tire models over the past decades. A number of tire models have been proposed in the literature with different levels of complexity and targeted applications, each with own different focuses, merits, and limitations.

Among existing models, the brush model [115] depicts the physical nature behind tire behavior in an analytical way. Based on elasticity theory, the brush model describes the generation of tire forces by partitioning the contact patch into an adhesion and a sliding region. Typically it assumes that a certain pressure profile is distributed along the deformable contact patch, and tire forces are generated due to the relationship between stress and strain. However, it requires a number of parameters related to elastomer material properties, which are difficult to obtain without material experimental tests.

The Dugoff's tire model originated in 1970's [116, 117]. Due to its relatively simple formulation and capability of accounting for longitudinal and lateral coupling effect, it has been applied to the design of vehicle control systems [118, 119, 120].

The formulation of this tire model is as follows. First an effective adhesion coefficient is computed.

$$\mu_R = \mu_{\text{peak}}\left(1 - A_s R_w \omega \sqrt{\lambda^2 + \tan^2\alpha}\right) \tag{5.41}$$

Table 5.1: Parameters and variables used in the Dugoff's tire model

Symbol	Description	Unit
μ_R	Road adhesion coefficient	−
μ_{peak}	Peak road adhesion coefficient	−
A_s	Adhesion discount factor due to sliding in the contact patch	s/m
R_w	Tire effective radius	m
ω	Wheel rotational velocity	rad/s
λ	Tire longitudinal slip	−
α	Tire slip angle	rad
H	Adhesion/sliding decision variable	−
C_λ	Tire longitudinal stiffness	N
C_α	Tire lateral stiffness	N/rad
F_z	Tire normal force	N

The parameters and variables for this tire model can be found in Table 5.1. Then a dimensionless decision variable is derived.

$$H = \sqrt{\left(\frac{C_\lambda \lambda}{\mu_R F_z (1-\lambda)}\right)^2 + \left(\frac{C_\alpha \tan\alpha}{\mu_R F_z (1-\lambda)}\right)^2} \tag{5.42}$$

The tire planar forces are computed based on the condition of *H*.

$$F_x = \begin{cases} \dfrac{C_\lambda \lambda}{1-\lambda}, & H < \dfrac{1}{2} \\ \dfrac{C_\lambda \lambda}{1-\lambda}\left(\dfrac{1}{H} - \dfrac{1}{4H^2}\right), & H \geq \dfrac{1}{2} \end{cases}, \quad F_y = \begin{cases} \dfrac{C_\alpha \tan\alpha}{1-\lambda}, & H < \dfrac{1}{2} \\ \dfrac{C_\alpha \tan\alpha}{1-\lambda}\left(\dfrac{1}{H} - \dfrac{1}{4H^2}\right), & H \geq \dfrac{1}{2} \end{cases} \tag{5.43}$$

Essentially the only parameters that need to calibrate for a specific tire are C_α and C_λ. An example plot of Dugoff's tire model is shown in Figure 5.10, with parameters taken from [121]. The simplicity of Dugoff's tire model is both its advantage and deficiency. With only two calibration parameters, it performs well for small slip ratio or slip angle regions. However, for the applications where the tire is operating with large slip ratios or slip angles, the coupling effects between tire longitudinal and lateral forces are not modeled adequately.

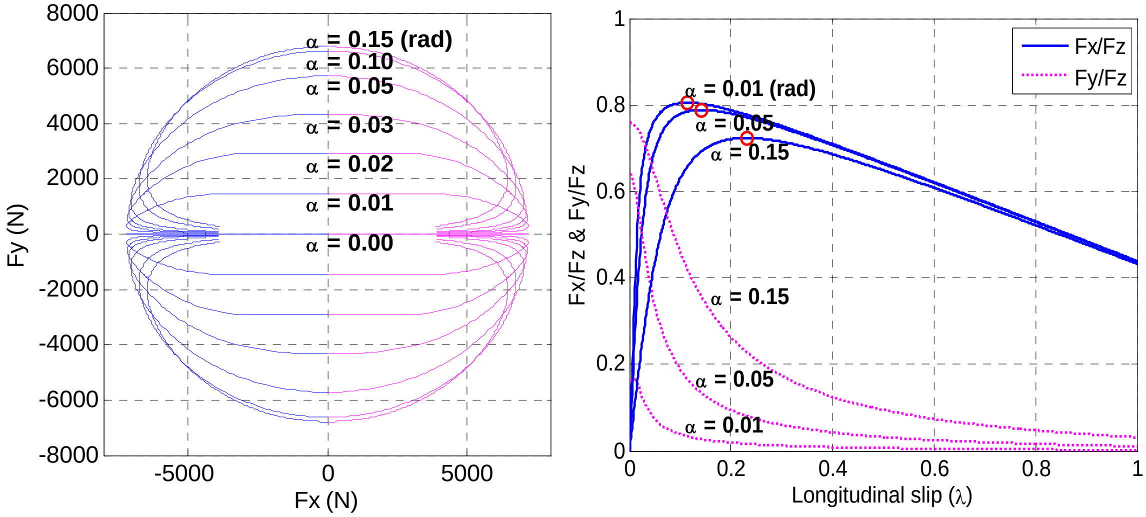

Figure 5.10: Dugoff's tire model. Friction ellipse (left) and normalized longitudinal and lateral forces (right)

Magic Formula tire model [122] is possibly the most popular model in vehicle and tire dynamics community. It consists of empirical formulations based on experimental data. Since eventually it will be used for the development of control system in this dissertation, the details of Magic Formula model are separately elaborated in the Section 5.5.

5.5 Magic Formula Tire Model

One of the best-known tire models is the so-called Magic Formula (MF) tire model developed and constantly refined by Pacejka and other researchers at Delft University of Technology, see Section 4.3 in [123]. The Magic Formula tire model consists of a set of semi-empirical equations to characterize tire behavior, which demonstrate close fitting to experimental data and is widely used for vehicle dynamics simulations and analyses [114]. The MF model describes the characteristics of tire longitudinal force, lateral force, and self-aligning moment with a series of unified equations “magically” well for a wide range of operating conditions, hence named Magic Formula by the vehicle dynamics community. Possible disadvantage of the MF model is that the calibration of its fitting parameters is not straightforward without experimental results.

5.5.1 Magic Formula Tire Model for Pure-slip Case

Given tire vertical loads and camber angles, the basic form of the Magic Formula tire model is expressed as follows, in which the horizontal and vertical shift terms in the original expression are omitted for simplicity.

$$y(x) = D\sin\left\{C\arctan\left[Bx - E\left(Bx - \arctan(Bx)\right)\right]\right\} \tag{5.44}$$

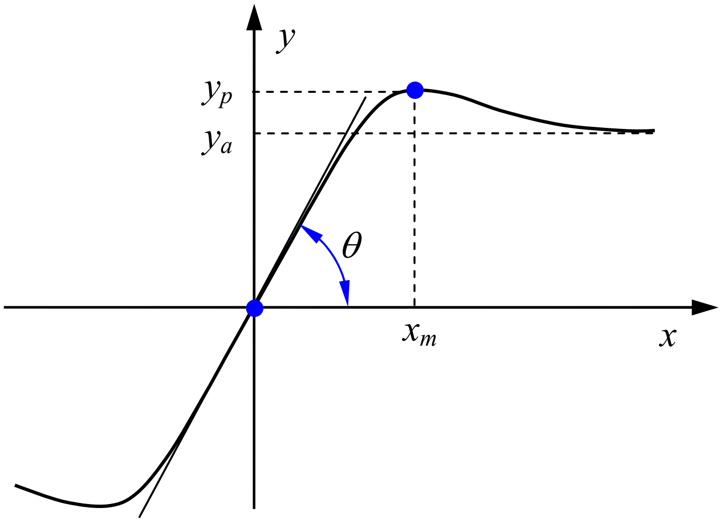

Figure 5.11: Curve generated by the Magic Formula, adapted from Fig. 4.9 in [123]

Among the four defining parameters in the expression, *B* is the stiffness factor, *C* is the shape factor, *D* is the peak factor, and *E* is the curvature factor. They can be parameterized as functions of tire normal load, wheel camber angle, road friction coefficient, and so on. In the formulation, x is the independent variable, such as the slip ratio (λ) or the slip angle (α), and y is the dependent variable, such as the longitudinal or lateral tire force (F_x, F_y), respectively.

The pure-slip Magic Formula generates an anti-symmetric curve that passes through the origin, ascends to its peak, and subsequently declines and converges to a horizontal asymptote. Figure 5.11 illustrates the implication of major influencing factors. It can be shown that the following four equations hold for the relationship among key curve attributes and the defining parameters.

$$y_p = D\,,\; y_a = D\sin\left(\frac{C\pi}{2}\right),\; \tan\left(\theta\right) = BCD\,,\; E = \frac{Bx_m - \tan\left(\frac{\pi}{2C}\right)}{Bx_m - \arctan\left(Bx_m\right)}\left(if\ C > 1\right) \tag{5.45}$$

where y_p is the peak value of the curve, y_a is its asymptotic value, $\tan(\theta)$ is the slope at the origin, and x_m is the “argmax” value of the curve.

5.5.2 Magic Formula Tire Model for Combined-slip Case

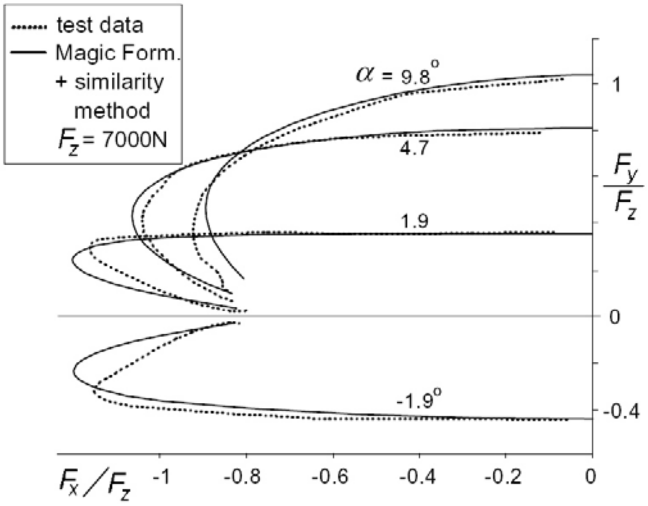

Figure 5.12: Experimental measurements and MF fitting curves (Fig. 4.8 in [123])

Experimental results have shown that the Magic Formula tire model is capable of generating tire characteristics that closely match measured data for longitudinal force, lateral force, and self-aligning moment over large ranges of slip ratio and slip angle (Figure 5.12, reproduced from [123]). There are various treatments to account for combined-slip cases with MF equations in the literature [120, 124, 125]. The approach detailed here is primarily based on Gordon's formulation [124].

First one defines the combined-slip vector

$$\mathbf{s} = \begin{pmatrix} s_x \\ s_y \end{pmatrix}, \tag{5.46}$$

where $s_x = \lambda$ and $s_y = \tan\alpha$. Then the unit vector defining the slip direction is

$$\begin{pmatrix} \hat{s}_x \\ \hat{s}_y \end{pmatrix} = \frac{1}{\sqrt{s_x^2 + s_y^2}} \begin{pmatrix} s_x \\ s_y \end{pmatrix}. \tag{5.47}$$

The basic form of the pure-slip Magic Formula is modified as follows

$$P(x;C,E) \square \sin\left\{ C \arctan\left[\frac{x}{C} - E\left(\frac{x}{C} - \arctan(\frac{x}{C}) \right) \right] \right\}, \tag{5.48}$$

which has a unit peak (*D* = 1) and a unit slope at the origin (*BCD* = 1). The force vector for the case of combined slip ratio and slip angle is computed by

$$\begin{pmatrix} F_x \\ F_y \end{pmatrix} = F_p \cdot P\left(\frac{C_\alpha \|\mathbf{s}\|}{F_p}; C, E \right) \cdot \begin{pmatrix} \hat{s}_x \\ \hat{s}_y \end{pmatrix}. \tag{5.49}$$

In the above equation, the peak tire force F_p is computed as a function of tire vertical load F_z.

$$F_p(F_z) = \frac{F_z}{1 + (1.5 \times F_z / Mg)^3}, \tag{5.50}$$

where *M* is the nominal vehicle mass that effectively determines the tire load rating. The cornering stiffness C_α (equal to the longitudinal stiffness in this modeling approach) also changes with tire normal load as indicated below, and it saturates when the normal load is sufficiently high.

$$C_\alpha(F_z) = c_1 Mg\left(1 - e^{-c_2 F_z / Mg}\right), \tag{5.51}$$

where both c_1 and c_2 are fixed dimensionless constants obtained through data-fitting. Two surface plots are presented in Figure 5.13 and Figure 5.14 to illustrate the dependence of tire longitudinal and lateral forces (in absolute values) on slip ratios and slip angles for a given normal load. The tire parameters are derived to fit vehicle responses of the CarSim "Big SUV" model on a high-μ road. The pure-slip relationship can also be obtained from the figures when one independent variable is set to zero ($\alpha = 0°$ for F_x or $\lambda = 0$ for F_y).

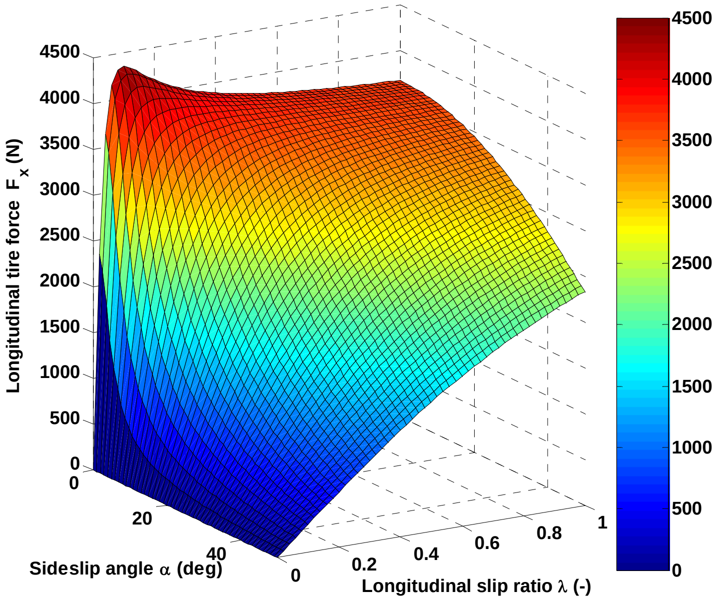

Figure 5.13: Example plot of tire longitudinal forces in combined-slip cases (F_z = 5900 N)

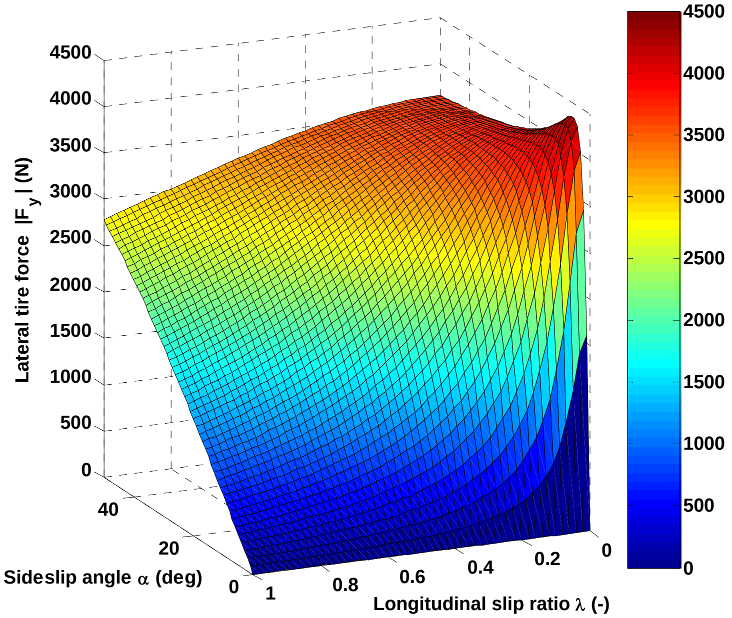

Figure 5.14: Example plot of tire lateral forces in combined slip cases (F_z = 5900 N)

The concept of tire adhesion ellipse can be visualized by plotting tire lateral forces against longitudinal forces and an envelope curve enclosing them (Figure 5.15).

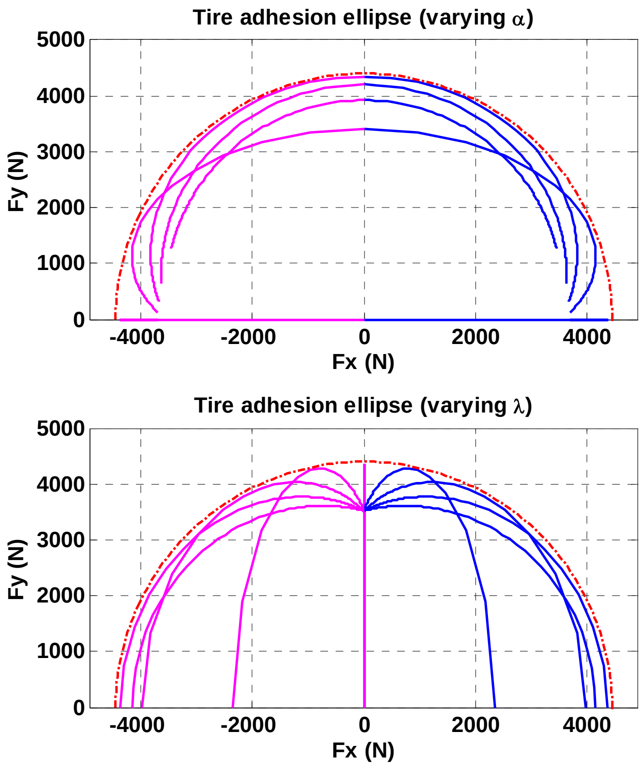

Figure 5.15: Tire forces and enclosing adhesion ellipse (F_z = 5900 N)

The two subplots of Figure 5.15 reveal how the tire force components evolve as the slip ratio and the slip angle change. In the top subplot, the slip ratio varies continuously between -1 and 1, while the sideslip angles are fixed at α = 0°, 2°, 5°, 10°, 20°, respectively. In the bottom subplot, the sideslip angle is varied while the slip ratios are fixed at λ = 0%, 2%, 5%, 10%, 20%. In both scenarios, the plotted curves can be enclosed by one identical elliptical curve, which indicates tire behavior at adhesion limits.

5.5.3 Gradients of Tire Forces wrt Longitudinal and Lateral Slips

The surface plots in Figure 5.13 and Figure 5.14 have shown that although tire forces are nonlinear functions of slip ratios and slip angles, the 3-dimensional surfaces are generally quite smooth. Potentially the longitudinal and lateral forces are differentiable with respect to the two inputs. If the partial derivatives for F_x and F_y can be obtained analytically, the gradients at an arbitrary point on the 3-d surfaces can be determined, which are heavily used in Section 5.3.3 for the control allocation problem.

First take the derivative of Eq. (5.48) with respect to the input x,

$$\frac{dP}{dx} = P'(x) = \cos\left\{ C \arctan\left[\frac{x}{C} - E\left(\frac{x}{C} - \arctan(\frac{x}{C}) \right) \right] \right\} \times$$
$$\frac{C}{1 + \left[\frac{x}{C} - E\left(\frac{x}{C} - \arctan(\frac{x}{C}) \right) \right]^2} \cdot \left[\frac{1}{C} - E\left(\frac{1}{C} - \frac{1/C}{1 + (x/C)^2} \right) \right] . \tag{5.52}$$

For convenience, let

$$s_a = \frac{C_\alpha \sqrt{s_x^2 + s_y^2}}{F_p} , \tag{5.53}$$

then $\frac{\partial s_a}{\partial s_x} = \frac{C_\alpha}{F_p} \cdot \frac{s_x}{\sqrt{s_x^2 + s_y^2}}$, $\frac{\partial s_a}{\partial s_y} = \frac{C_\alpha}{F_p} \cdot \frac{s_y}{\sqrt{s_x^2 + s_y^2}}$. Since $\begin{pmatrix} F_x \\ F_y \end{pmatrix} = F_p \cdot P\left(\frac{C_\alpha \sqrt{s_x^2 + s_y^2}}{F_p} \right) \cdot \frac{1}{\sqrt{s_x^2 + s_y^2}} \begin{pmatrix} s_x \\ s_y \end{pmatrix}$, the four partial derivative terms can be obtained.

$$\frac{\partial F_x}{\partial s_x} = P'(s_a) \cdot C_\alpha \cdot \frac{s_x^2}{s_x^2 + s_y^2} + F_p \cdot P(s_a) \cdot \frac{s_y^2}{(s_x^2 + s_y^2)^{3/2}} , \tag{5.54}$$

$$\frac{\partial F_x}{\partial s_y} = P'(s_a) \cdot C_\alpha \cdot \frac{s_x s_y}{s_x^2 + s_y^2} - F_p \cdot P(s_a) \cdot \frac{s_x s_y}{(s_x^2 + s_y^2)^{3/2}} , \tag{5.55}$$

$$\frac{\partial F_y}{\partial s_x} = P'(s_a) \cdot C_\alpha \cdot \frac{s_x s_y}{s_x^2 + s_y^2} - F_p \cdot P(s_a) \cdot \frac{s_x s_y}{(s_x^2 + s_y^2)^{3/2}} , \tag{5.56}$$

$$\frac{\partial F_y}{\partial s_y} = P'(s_a) \cdot C_\alpha \cdot \frac{s_y^2}{s_x^2 + s_y^2} + F_p \cdot P(s_a) \cdot \frac{s_x^2}{(s_x^2 + s_y^2)^{3/2}} . \tag{5.57}$$

Figure 5.16 shows the same tire behavior as in Figure 5.15 but in an alternative view. Again, in the top subplot, the slip ratio varies between 0 and 1, and the sideslip angles are fixed at discrete levels α = 0°, 2°, 5°, 10°, 20°. In the bottom subplot, the sideslip angle is varied and the slip ratios are fixed at five levels λ = 0%, 2%, 5%, 10%, 20%. In addition, two groups of local tangents, whose values are taken directly from Figure 5.17, are superimposed on the tire force curves as a result of the computation of the partial derivatives. These gradients verify the accuracy of the computation procedures of partial differentiation. Figure 5.17 presents the numerical values of partial derivatives for a given tire vertical load, and they correspond to the slopes on the 3-d plots in Figure 5.13 and Figure 5.14. The fact that the gradients can be obtained analytically in this modeling approach provides great benefits to solve the control allocation problem in Section 5.3.3.

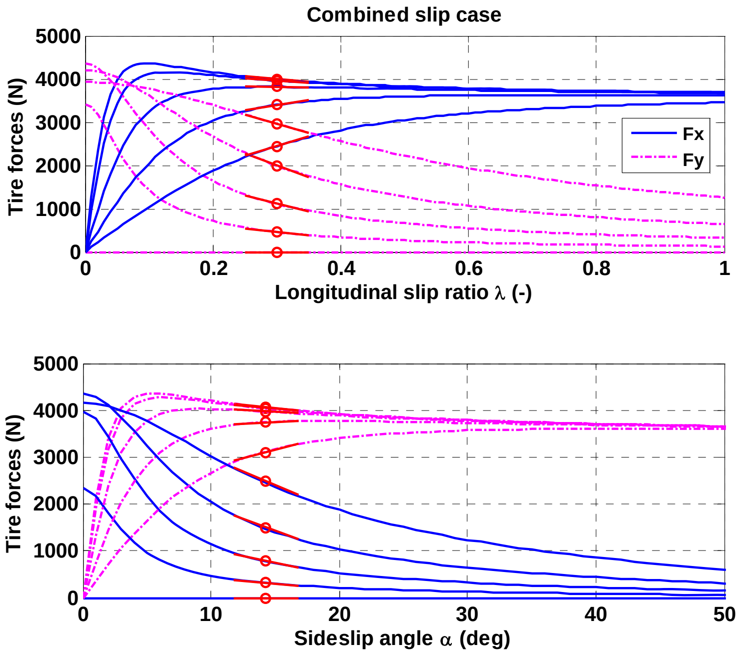

Figure 5.16: Tire forces in combined-slip cases with superimposed local gradients

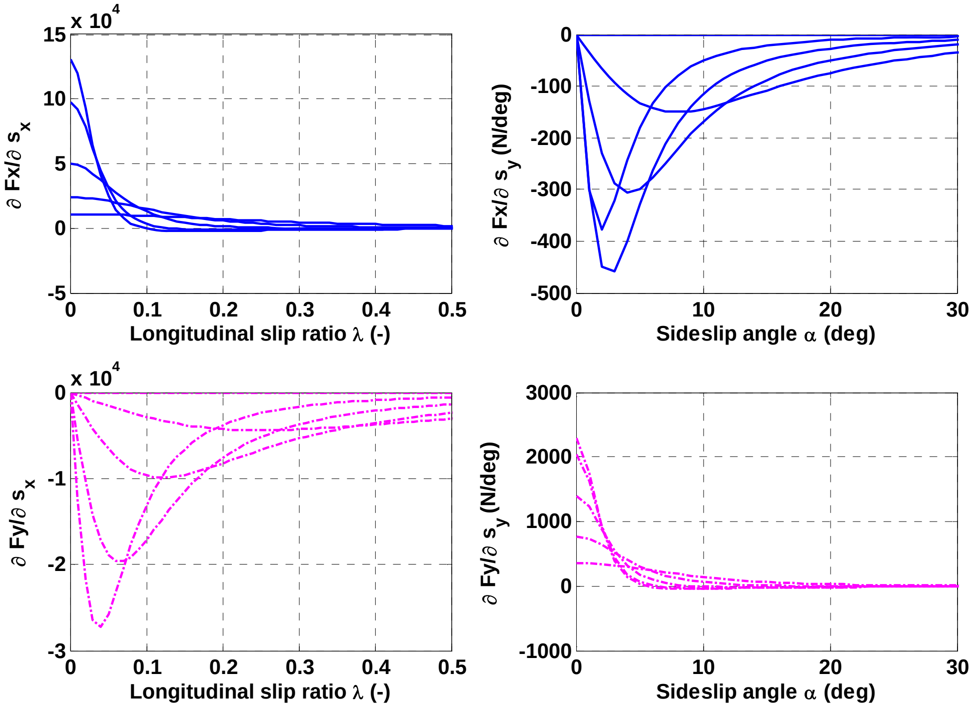

Figure 5.17: Partial derivatives of tire forces w.r.t. slip ratios and slip angles

For different road surfaces with various friction levels, tire parameters need to be adjusted accordingly. The friction similarity technique [126] can be used to approximate the effects of variations of friction level on tire forces and aligning moment.

5.6 Simulation Studies

The proposed hierarchical control system for vehicle handling is applied to the vehicle stabilization task against impulsive disturbances as encountered in PISC scenario. As depicted in Figure 5.18, suppose two vehicles originally moving in the same direction are involved in an angled rear-end impact. It can happen in the form of a lane change or merge accident on highways. It is assumed that the velocity difference before the impact is not significant, and as a result, no substantial vehicle structural deformation occurs in the damage areas on both vehicles. However, the collision can lead to great changes of yaw rate and lateral velocity and costs the loss of directional control, especially for the struck (target) vehicle.

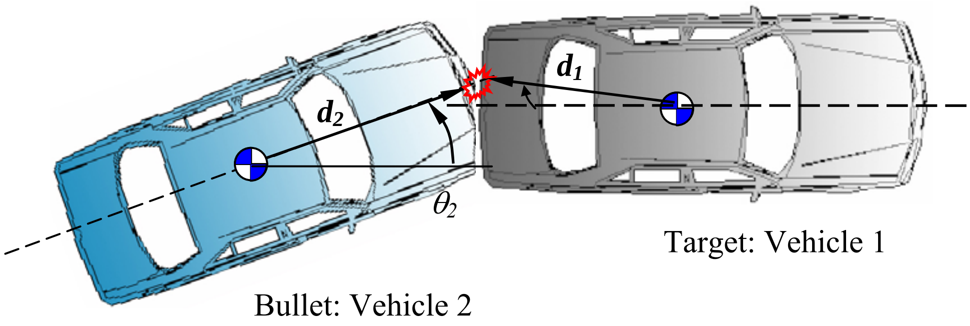

Figure 5.18: A light-impact collision scenario that generates impulsive disturbances

The focus of this section is on the post-impact states regulation of the target vehicle. The modeling approach for the collision process has been discussed in Section 2.4, which computes the kinematic state changes and collision impulses for vehicles involved in light impacts. The objective here is to attenuate and stabilize vehicle motions after severe disturbances by applying the control approach developed in previous sections. The simulation environment is implemented in the vehicle dynamics package CarSim.

The pre-impact longitudinal velocity of the target vehicle is set at $v_x = 29$ m/s, and 33.5 m/s for the bullet vehicle. Before the impact, both vehicles are traveling straight on paved road ($\mu_R = 0.7$), but the bullet vehicle have an oblique angle of 18°. The collision impulses are applied to the front bumper center of the bullet vehicle, and +0.1 m to the right of the rear bumper center of the target vehicle. Both vehicles have parameters (mass, wheelbase, etc.) corresponding to the "Baseline Big SUV" model in CarSim. The assumed coefficients of restitution and tangential interaction during the crash are $e = 0.20$ and $\mu = 0$. After the computation of the collision process, the post-impact lateral velocity and yaw rate of the target vehicle change fast to $V_y = 3.3$ m/s and $\Omega_z = -64$ deg/s due to the impulse.

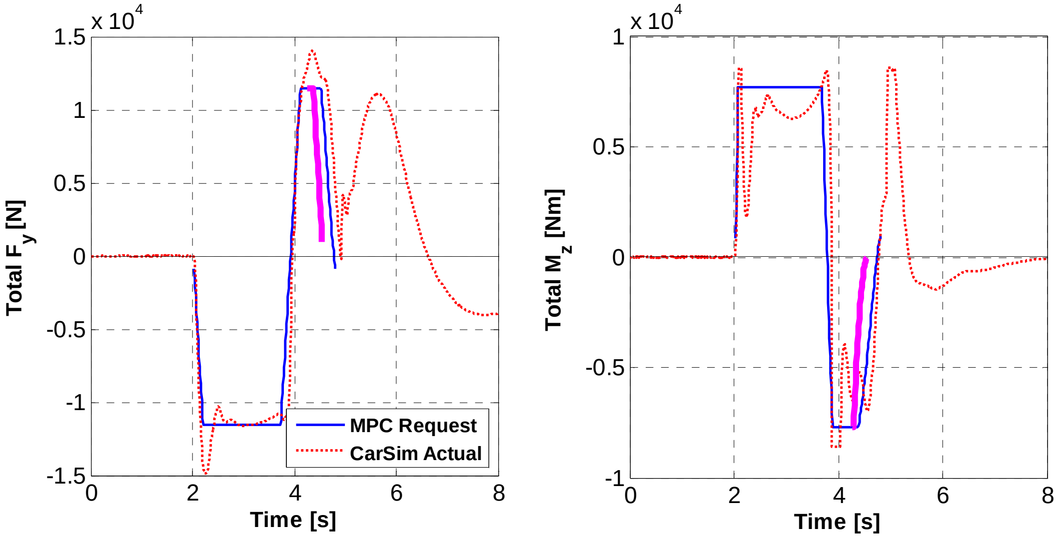

Figure 5.19: Comparison of the desired ground force dictated by MPC and the actual ground force

The impact is detected by the sensing algorithm described in Section 3.2 and the stabilization control module is activated in due time. For the post-impact vehicle motion regulation, a prediction horizon of 0.3 second (or 30 samples) is used for the MPC supervisory controller. The same controller derivation procedure applies to either the 2-state yaw plane model or the 4-state yaw-roll model, with higher computational load associated with the latter model. For the simulation studies in this section, the 4-state model is adopted. The constraints on the virtual controls are found at saturation limits $|F_y| \leq 11500$ N and $|M_z| \leq 7700$ Nm, selected based on vehicle mass and road adhesion conditions. Figure 5.19 shows the comparison of the desired ground forces dictated by

MPC, which are tracked by the actual ground forces generated by the nonlinear vehicle model in the CarSim simulation software.

It should be noted that MPC commands are nonzero only when PISC activation is warranted, roughly during the time interval 2~5 sec. After that, since the vehicle states have been substantially mitigated, the driver takes over, steers the vehicle back to its original lane and proceeds until safely stops. The thick curves starting at 4.2 second in Figure 5.19 exemplifies the optimal control sequence determined at that instant. A comparison of vehicle trajectories is shown in Figure 5.20 and the vehicle responses are shown in Figure 5.21.

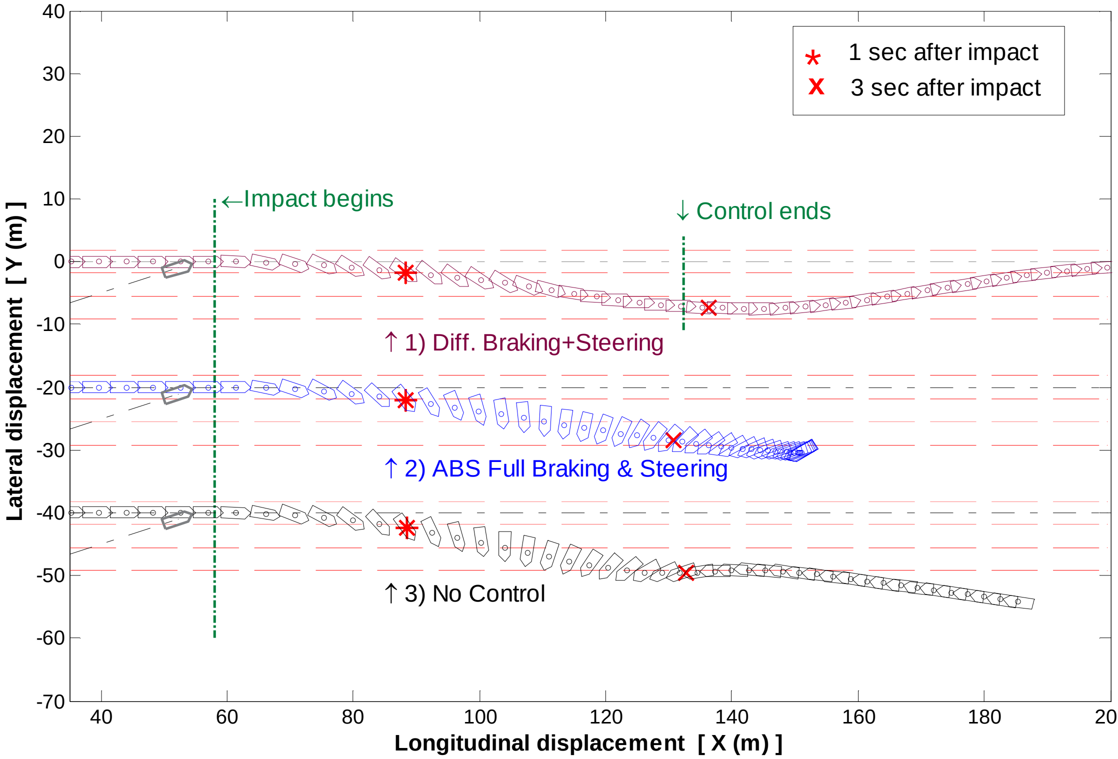

Figure 5.20: Vehicle trajectories in an impulsive disturbance rejection maneuver

Three control scenarios are presented in Figure 5.20 and Figure 5.21 for comparison. Without applying proper braking or steering intervention (Scenario 3), the vehicle quickly develops substantial slip angle and heading angle in response to the impulse, and eventually departs from the designated lanes. With full ABS braking and driver's steering inputs (Scenario 2), the vehicle velocity is significantly reduced. However, the high yaw rate cannot be effectively attenuated, and the vehicle keeps spinning and leads to a heading angle beyond recovery (~150°). With the proposed control scheme actuated through differential braking (Scenario 1), the disturbed vehicle states are effectively regulated. Despite the limited lateral deviations, the vehicle maintains its directional stability and orientation. Eventually its yaw rate and slip angle are attenuated to insignificant levels and the driver can easily maneuver the vehicle and stop safely or proceed to a safe location afterwards.

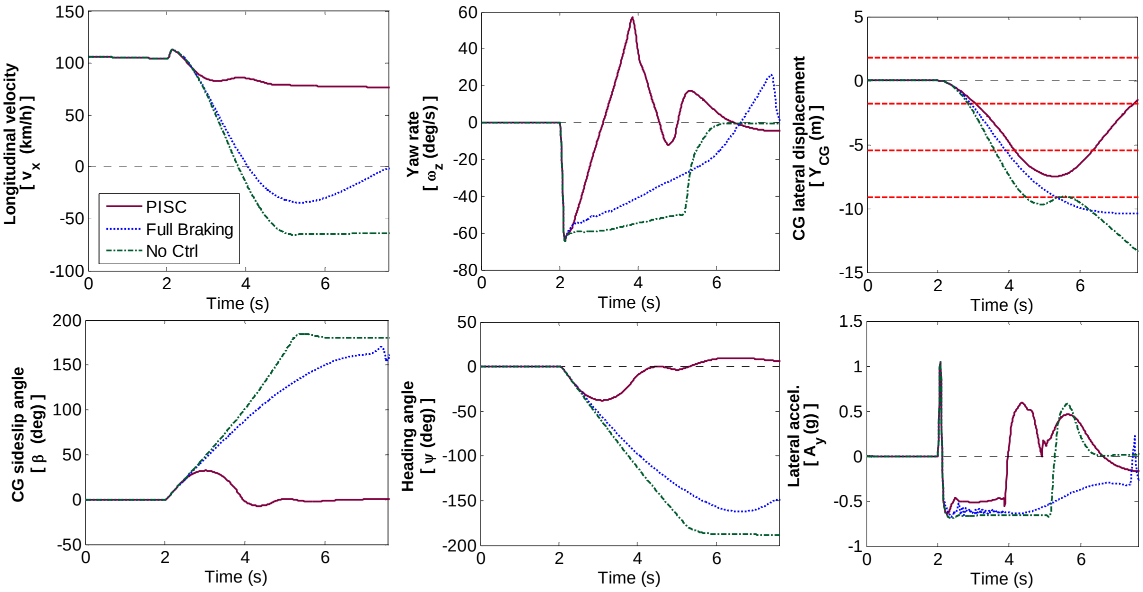

Figure 5.21: Comparison of vehicle responses in an impulsive disturbance rejection maneuver

Further details of the actively controlled scenario are given in the rest of this section. In order to realize the virtual control efforts determined in Figure 5.19, the optimal control allocation scheme is employed to distribute the generalized forces to four wheels, through changing the slip ratio commands. The combined-slip Magic Formula tire model is particularly instrumental during this stage. Figure 5.22 demonstrates the comparison of eight estimated tire force components and the actual values given by the vehicle model in CarSim. The detailed scheme to estimate CG lateral velocity and tire forces is presented in Appendix C. Overall the estimation accuracy is quite satisfactory.

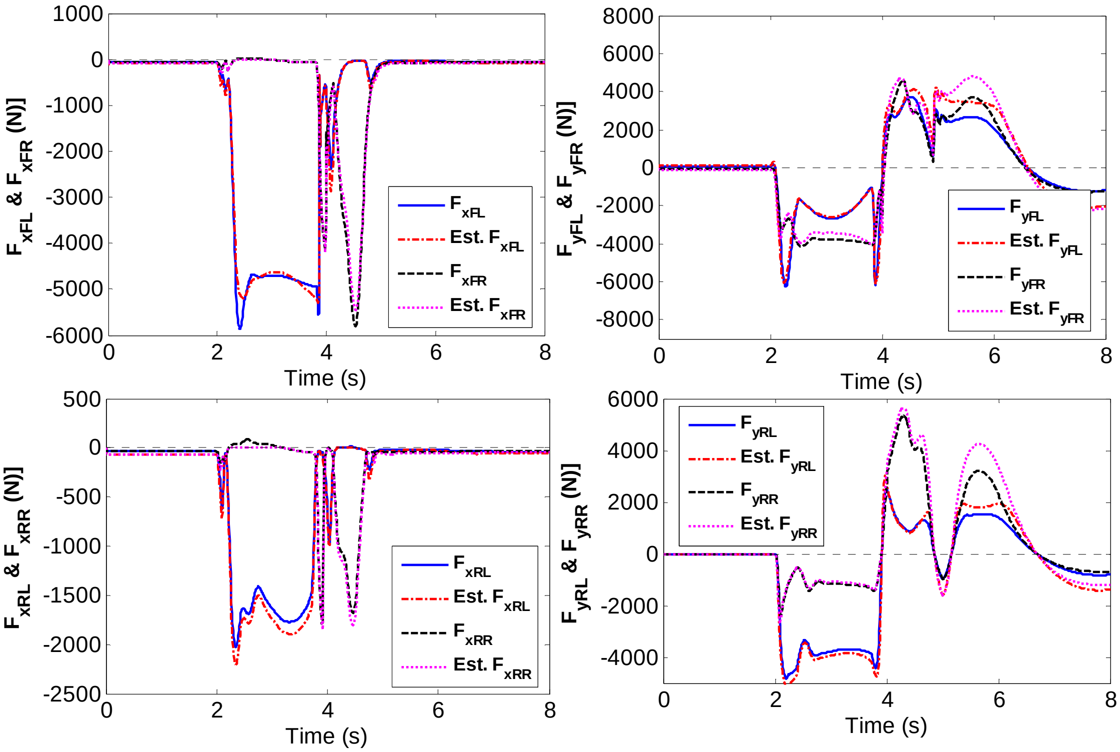

Figure 5.22: Tire force estimation with a combined-slip Magic Formula model

The results of the optimal control allocation are shown in the left subplot of Figure 5.23. At the beginning of the stabilization process, the control commands are given as limit values. In order to achieve the slip ratio commands, a wheel-slip control module based on the sliding model control theory is used as in Section 4.4. It tracks the slip ratio commands by generating the physically realistic control inputs to feed into the controller/CarSim interface: wheel cylinder braking pressure commands, as shown in the left subplot of Figure 5.24. The actually delivered pressures are produced by processing the braking requests through hydraulic systems composed of time lag, time delay, and rate limiters (right subplot of Figure 5.24). The delivered pressures along with wheel dynamic states result in the actual wheel slips shown in the right subplot of Figure 5.23. The instantaneous wheel slips, along with tire slip ratios (not actively controlled in this example) and normal loads, generate tire longitudinal and lateral forces, whose combined effects have been shown in Figure 5.19 (dashed lines).

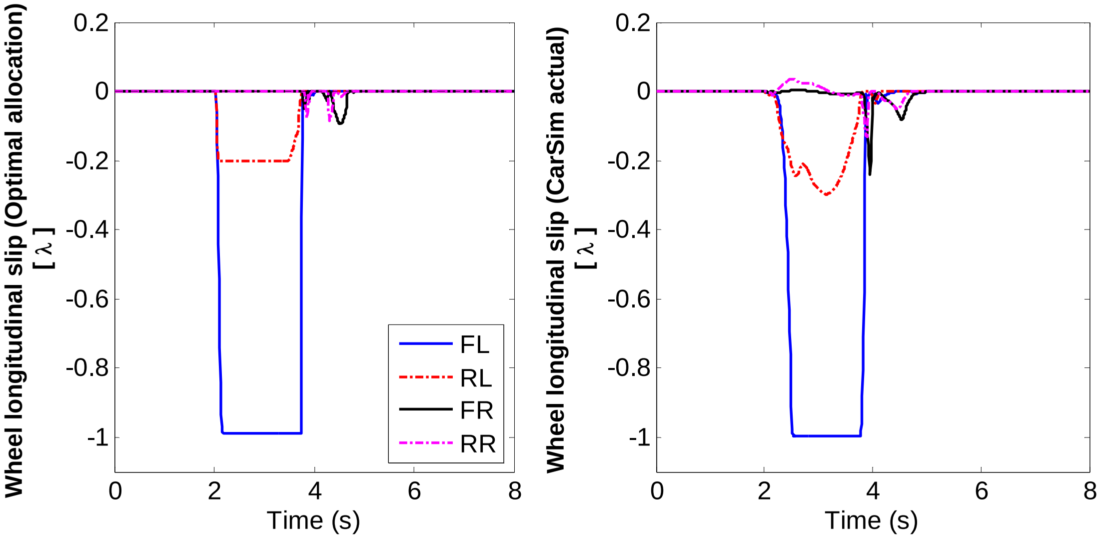

Figure 5.23: Comparison of the slip ratio commands and the actual slip ratios generated in CarSim in a typical PISC maneuver

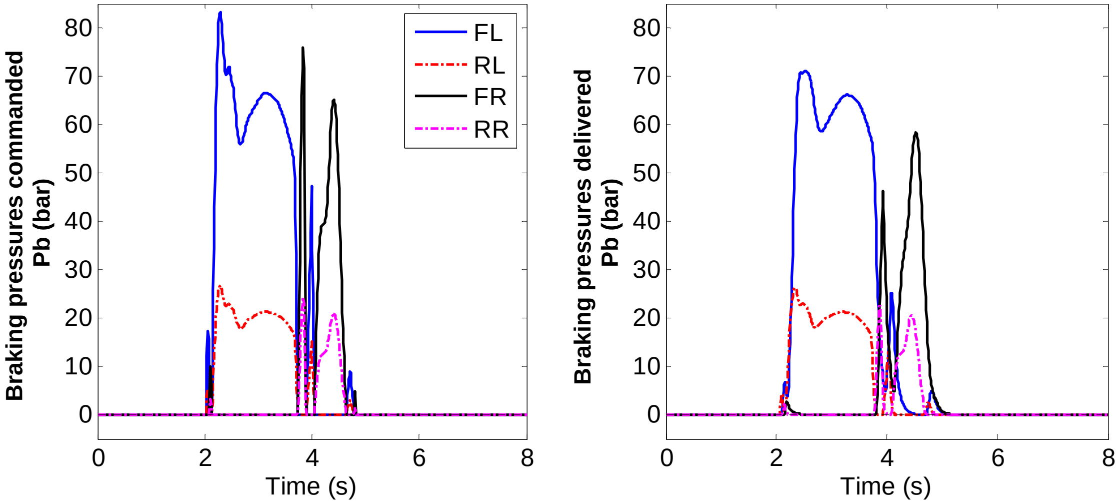

Figure 5.24: Comparison of the braking pressures commanded and delivered in a typical PISC maneuver

Finally, in this section an assessment of the proposed control system to accommodate actuator degradation is conducted. The simulated rear-end crash scenario has the same layout as in Figure 5.18. The vehicles involved are assumed to travel on a highway and the pre-impact forward speed of the struck vehicle is 30 m/s. The collision impulse changes its yaw rate instantly to -50 deg/s, and the struck vehicle would spin out in clockwise direction if no effective stabilization efforts were implemented.

To incorporate the effects of actuator degradation, it is further assumed that the hydraulic braking system on the front left (FL) corner was compromised for certain reasons during the collision. Its hydraulic circuit can only deliver 30% of the braking pressure commands dictated by the upper-level controller. The constrained optimal allocation in Section 5.3.3 and the sliding surface controller in Section 4.2 are compared below in terms of their ability to cope with this degradation in braking performance.

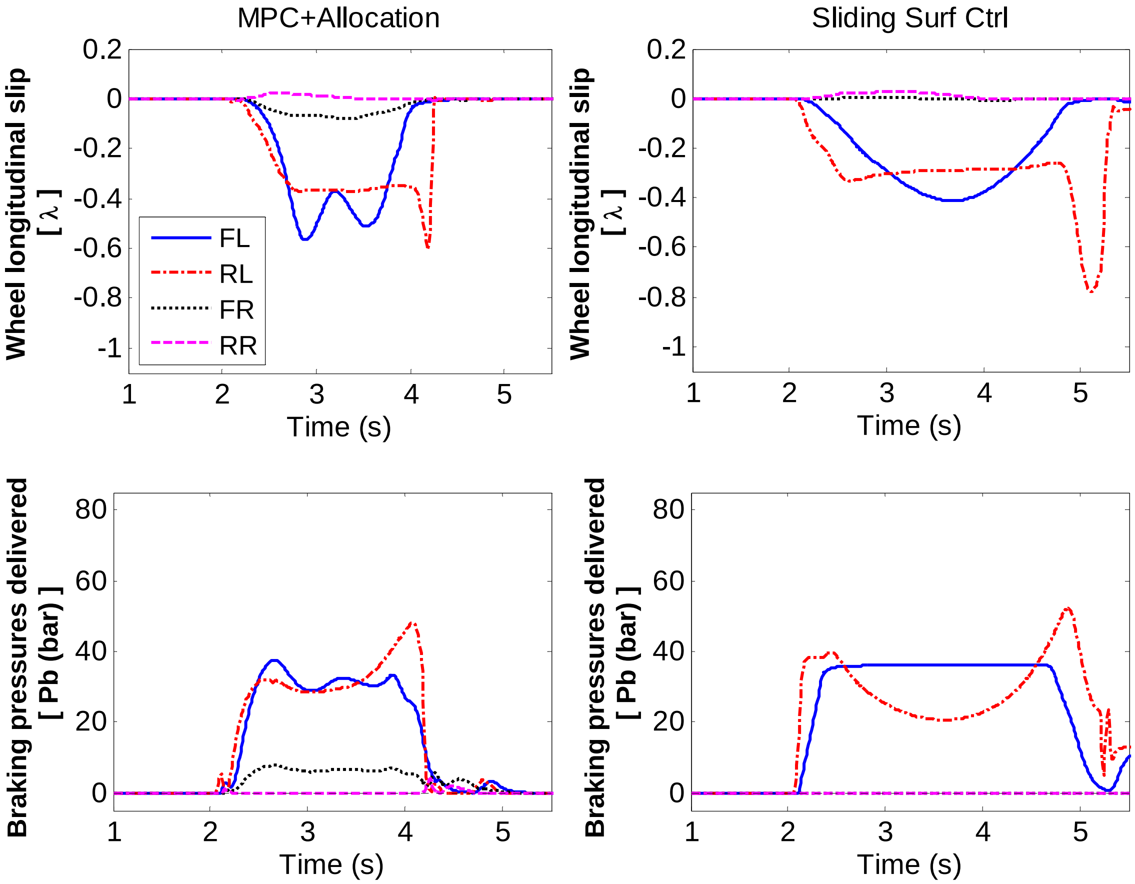

Figure 5.25: Comparison of wheel slip ratios and delivered braking pressures for two control systems (with FL wheel actuator degradation)

The nominal peak cylinder pressure is 120 bar (as in Figure 4.8), and the actual braking pressure on FL corner can build only up to 36 bar. The wheel slip ratios and the delivered braking pressures for the two control systems are illustrated in Figure 5.25. Eventually both systems can stabilize the vehicle, but the case with sliding surface control is less efficient. The braking pressures in the bottom subplots show that the optimal allocation approach can request a slight braking from the FR wheel, so that the desired total yaw moment M_z and lateral force F_y can be attained with a better trade-off, despite the under-performance of the FL wheel.

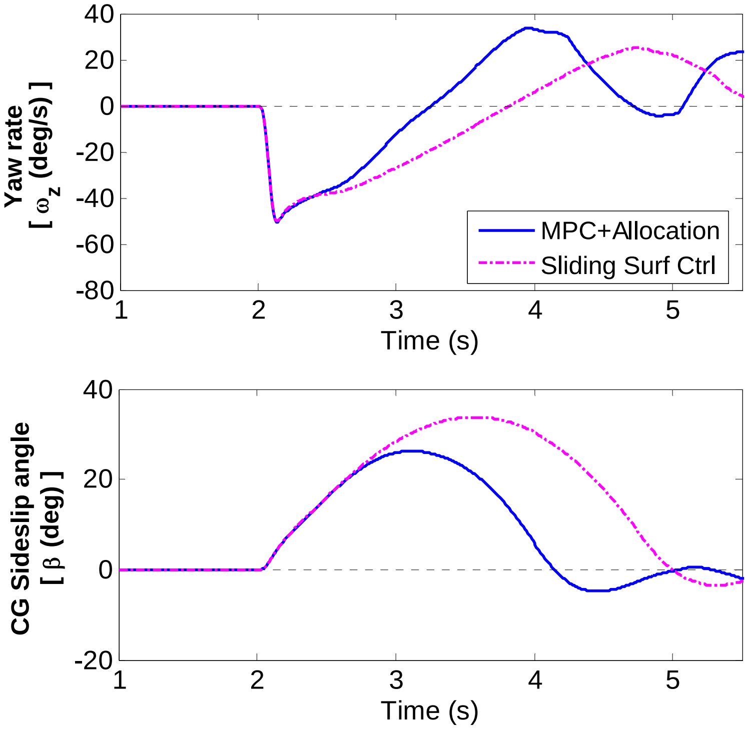

Figure 5.26: Comparison of yaw rates and sideslip angles for two control systems (with FL wheel actuator degradation)

Figure 5.26 verifies that the post-impact motion of the struck vehicle can be stabilized with either control system. It takes the MPC plus optimal allocation approach approximately 3 seconds in this particular case, supposedly longer than either control system when no actuator degradation is present. During the transience of stabilization control, the sliding surface control approach results in slower yaw mitigation and higher peak sideslip angle.

5.7 Conclusions

A model-based hierarchical control framework is developed for vehicle handling and applied to the post-impact stabilization scenario. The proposed architecture consists of three stages, which interact closely but can be independently designed. The supervisory stage dictates the desired total ground forces via MPC scheme, so that certain regulation or tracking objectives are fulfilled. The intermediate stage takes the desired total forces and yaw moment as inputs. Through constrained optimal allocation, wheel slip ratio/angle commands are generated so that the difference between the desired forces and those actually developed on the tires is minimized in the least-square sense. The lower stage seeks to track the wheel slips requested by the intermediate stage, by manipulating the wheel cylinder braking pressures. The control approach adopted at this stage is based on the sliding mode control theory. The developed control system provides the benefits of a modularized approach to integrate vehicle stabilization objective fulfillment, the optimality of tire force allocation, and robust tracking of slip ratio commands.

The overall control system is evaluated on a multibody vehicle model provided by CarSim software under limit handling conditions. Simulations are conducted on a case in which the vehicle subject to a strong impulsive disturbance loses directional stability with manual steering and full braking control. However, with the proposed control system applied, the vehicle remains stable. The simulation results demonstrate the significant improvement of limit handling performance. In order to compare the control system proposed in this chapter with the one in Chapter 4, simulations are conducted to assess their capability of tolerating actuator degradation. The control system composed of MPC and optimal allocation can better coordinate all available actuators and make adjustments to achieve the objective. Finally, although differential braking is illustrated in this chapter, the proposed control framework can be applied to vehicles equipped with other actuators and their combinations such as active steering, braking and traction, so that their influences can be fully leveraged, and the overall control objective can be attained in an integrated and coordinated way.

Chapter 6

Conclusions and Future Work

6.1 Conclusions

In this dissertation, a Post-Impact Stability Control (PISC) system is proposed to assist the driver to recover vehicle stability after an initial impact, so that secondary crashes or rollover accidents can be avoided or mitigated. The PISC system adds a new dimension to a comprehensive vehicle active safety system.

This study first addressed the vehicle-to-vehicle collision problem. A model of vehicle collision was constructed to facilitate the characterization of the post-impact vehicle kinematic states, so that the initial conditions of post-impact vehicle motions can be determined. The colliding vehicles have each been modeled as rigid bodies with four degrees of freedom, which is different from the planar model commonly used in the literature. In contrast to conventional momentum-conservation-based methods, the proposed approach took tire forces into account. Improved model prediction accuracy was demonstrated through numerical examples.

The next task is to ensure that the PISC system will be activated at the right moment when a crash has occurred, and will not get into action due to sensor defects or noises. The crash sensing criteria are based on evaluating the gradients of yaw rate and lateral acceleration. Then a model-based estimation procedure is applied to estimate crash magnitude and location, and to predict vehicle responses within a short future horizon. The crash event is confirmed if a consistency between predictions and actual measurements can be established.

In the next step, differential braking and/or active steering are actuated to attenuate intense post-impact motions of the vehicle, after the PISC system is activated and the crash event is confirmed. The side, timing, and magnitude of braking actuation are based on the generation of a desired stabilizing yaw moment, which is in turn derived by adopting the multiple sliding surface control approach. The overall PISC system is implemented in Simulink and interfaced with a nonlinear SUV vehicle model in CarSim. The simulation results demonstrate the effectiveness of the proposed system in angled rear-end collisions with varying severity and direction.

In order to integrate multiple control objectives, a model-based hierarchical control framework is designed for vehicle handling and applied to the post-impact stabilization scenario. The developed control system consists of an MPC-based supervisory stage, an intermediate stage for optimal allocation, and wheel slip tracking at actuator stage. It provides the benefits of a modularized approach to accommodate control constraints and coordinate multiple control effectors in an optimal way.

6.2 Future Work

There are still a variety of issues that remain to be solved before the proposed system can be successfully implemented. The usefulness and practical performance of the proposed system can be further studied by addressing the following issues.

(1) The assumption that during the collision process, tire lateral forces develop immediately whenever sideslip angles are present needs to be further substantiated. In real crash, suspension compliances may cushion certain amount of collision energy to the sprung mass before the kinematics of the unsprung mass is affected. CarSim provides a multi-body nonlinear model for the study on vehicle handling performance, whereas a dedicated vehicle collision software may be needed to study the detailed responses of vehicle components during the collision.

(2) The reliability and timeliness of the crash sensing and validation procedure to provide triggering signals is crucial, and this procedure needs to be verified with signals actually measured or obtained in crash experiments. Its ability to execute in

real time and robustness against sensor noises needs to be examined more extensively.

(3) The arbitration and prioritization among ESC control commands, PISC control commands, and drivers' actions have to be studied in further depth. Drivers' steering intent has to be followed by active safety systems, but not necessarily "on face value," because drivers may behave irrationally and over-compensate. An interface needs to be designed to arbitrate and prioritize the three parties so as to streamline their interactions.

(4) The hierarchical control system proposed in Chapter 5 has the potential to cope with a plant with multiple interrelated control objectives. A 5-state vehicle model composed of longitudinal and lateral velocities, yaw and roll rates, as well as roll angle can be developed for the MPC supervisory controller, which coordinates and synergizes various demands on speed reduction, sideslip limitation, yaw attenuation, and roll mitigation in an integrated but explicit way. In addition, the treatment of the constraints on the total tire force F_y and moment M_z is simplified in that constant limits are applied to the whole MPC prediction horizon. A more realistic treatment should consider their inter-dependence [102], as well as their dependence on vehicle states. However, due to these nonlinear constraints, quadratic programming cannot be applied any more. If the constraints can be formulated in a quadratic form, the problem can be solved by second order cone programming (SOCP) routines [127].

(5) In the present design, the objective of the PISC system is to mitigate undesired post-impact motions. However, when this objective is achieved, the vehicle might be traveling at a certain angle relative to its original course. If environmental sensors and GPS navigation systems are available, potentially information about upcoming road geometry and neighboring objects can be retrieved. This information can be fused into the generation of control commands and desired trajectory, and help the vehicle follow road bending, especially on curved roads.

Appendices

Appendix A

Matrix Formulation for the Vehicle Collision Problem

Detailed entries for the Equation (2.21) in Section 2.4.

$$\begin{pmatrix} A_{11} & \mathbf{0} & A_{13} \\ \mathbf{0} & A_{22} & A_{23} \\ A_{31} & A_{32} & A_{33} \end{pmatrix} \cdot \mathbf{x} = \mathbf{B}$$

$$A_{11} = \begin{pmatrix} m_1 & 0 & -m_1 \frac{\Delta t}{2} V_{1y} & 0 \\ 0 & m_1 + \frac{\Delta t}{2} \frac{C_{f1} + C_{r1}}{V_{1x}} & m_1 \frac{\Delta t}{2} V_{1x} + \frac{\Delta t}{2} \frac{a_1 C_{f1} - b_1 C_{r1}}{V_{1x}} & -m_{R1} h_1 \\ 0 & \frac{\Delta t}{2} \cdot \frac{-a_1 C_f + b_1 C_r}{V_{1x}} & -I_{zz1} - \frac{\Delta t}{2} \frac{a_1^2 C_{f1} + b_1^2 C_{r1}}{V_{1x}} & -I_{xz1} \\ 0 & -m_{R1} h_1 & I_{xz1} - m_{R1} h_1 \frac{\Delta t}{2} V_{1x} & I_{xxs1} + \frac{\Delta t}{2} D_{s1} \end{pmatrix}$$

$$A_{13} = \begin{pmatrix} -1 & 0 & 0 & 0 \\ 0 & -1 & 0 & 0 \\ -y_A & x_A & 0 & 0 \\ 0 & -(z_A - h_1) & 0 & 0 \end{pmatrix}$$

$$A_{22} = \begin{pmatrix} m_2 & 0 & -m_2 \frac{\Delta t}{2} V_{2y'} & 0 \\ 0 & m_2 + \frac{\Delta t}{2} \frac{C_{f2} + C_{r2}}{V_{2x'}} & m_2 \frac{\Delta t}{2} V_{2x'} + \frac{\Delta t}{2} \frac{a_2 C_{f2} - b_2 C_{r2}}{V_{2x'}} & -m_{R2} h_2 \\ 0 & \frac{\Delta t}{2} \cdot \frac{-a_2 C_{f2} + b_2 C_{r2}}{V_{2x'}} & -I_{zz2} - \frac{\Delta t}{2} \frac{a_2^2 C_{f2} + b_2^2 C_{r2}}{V_{2x'}} & -I_{xz2} \\ 0 & -m_{R2} h_2 & I_{xz2} - m_{R2} h_2 \frac{\Delta t}{2} V_{2x'} & I_{xxs2} + \frac{\Delta t}{2} D_{s2} \end{pmatrix}$$

$$A_{23} = \begin{pmatrix} 0 & 0 & -1 & 0 \\ 0 & 0 & 0 & -1 \\ 0 & 0 & -y_{A'} & x_{A'} \\ 0 & 0 & 0 & -(z_{A'} - h_2) \end{pmatrix}$$

$$A_{31} = \begin{pmatrix} 0 & 0 & 0 & 0 \\ 0 & 0 & 0 & 0 \\ 0 & 0 & 0 & 0 \\ \cos\Gamma & \sin\Gamma & d_c \cos\Gamma - d_d \sin\Gamma & 0 \end{pmatrix}, \quad A_{33} = \begin{pmatrix} 1 & 0 & \cos\theta_2 & -\sin\theta_2 \\ 0 & 1 & \sin\theta_2 & \cos\theta_2 \\ \mu\cos\Gamma + \sin\Gamma & \mu\sin\Gamma - \cos\Gamma & 0 & 0 \\ 0 & 0 & 0 & 0 \end{pmatrix}$$

$$A_{32} = \begin{pmatrix} 0 & 0 & 0 & 0 \\ 0 & 0 & 0 & 0 \\ 0 & 0 & 0 & 0 \\ -\sin\theta_2 \sin\Gamma - \cos\theta_2 \cos\Gamma & \sin\theta_2 \cos\Gamma - \cos\theta_2 \sin\Gamma & d_a \cos\Gamma - d_b \sin\Gamma & 0 \end{pmatrix}$$

$$\mathbf{B} = \begin{pmatrix} m_1 v_{1x} & 0 & 0 & 0 & m_2 v_{2x'} & 0 & 0 & 0 & 0 & 0 & 0 & B_{12} \end{pmatrix}'$$

where $B_{12} = -e\left[(-v_{2x'} \sin\theta_2)\cdot\sin\Gamma + (v_{1x} - v_{2x'}\cos\theta_2)\cdot\cos\Gamma\right]$

Appendix B

Stability Analysis for the Multiple Sliding Surface Control System

B. 1 Problem Formulation

Consider the second-order nonlinear system

$$\begin{cases} \dot{x}_1 = f_1(x_1, x_2) - v_x x_2 \\ \dot{x}_2 = f_2(x_1, x_2) + \dfrac{u}{I_{zz}} \end{cases} \tag{B.1}$$

The regulation problem is to synthesize a control law for u so that x_1 and x_2 converge to zero despite nonzero initial conditions. Based on the multiple sliding surface control design [64], the control input u is chosen to be

$$u = -I_{zz}\hat{f}_2 + I_{zz}\left[\dot{x}_{2d} - k_2\left(x_2 - x_{2d}\right)\right] \tag{B.2}$$

where $\tau\dot{x}_{2d} + x_{2d} = \bar{x}_2$ and $\bar{x}_2 = \dfrac{\hat{f}_1 + k_1 x_1}{v_x}$. The following assumptions on the system in Eq. (B.1) are made in the stability analysis. The maps f_1 and f_2 are C^1, and $f_1(0,0) = f_2(0,0) = 0$. The nominal parts of the nonlinear functions are bounded by

$$\left|\hat{f}_1\right| \le q_{11}\left|x_1\right| + q_{12}\left|x_2\right| \tag{B.3}$$

$$\left|\hat{f}_2\right| \le q_{21}\left|x_1\right| + q_{22}\left|x_2\right| \tag{B.4}$$

In addition, the uncertain nonlinearity $\tilde{f}_1$ and $\tilde{f}_2$ satisfy

$$\left|\tilde{f}_1\right| \le m_{11}\left|x_1\right| + m_{12}\left|x_2\right| \tag{B.5}$$

$$\left|\tilde{f}_2\right| \le m_{21}\left|x_1\right| + m_{22}\left|x_2\right| \tag{B.6}$$

Define the boundary layer error as:

$$y_2 = x_{2d} - \bar{x}_2 \tag{B.7}$$

So $\dot{x}_{2d} = \dfrac{\bar{x}_2 - x_{2d}}{\tau} = \dfrac{-y_2}{\tau}$. Consider a candidate Lyapunov function

$$V = \frac{1}{2}S_1^2 + \frac{1}{2}S_2^2 + \frac{1}{2}y_2^2 \tag{B.8}$$

The subsequent analysis will show that its derivative $\dot V$ is negative definite with a proper selection of k_1, k_2, τ, therefore the closed-loop system given by Eqs. (B.1) and (B.2) for the regulation problem is exponentially stable.

B. 2 Lyapunov Stability Analysis

For the sliding surface errors,

$$\dot S_1 = \dot x_1 = \hat f_1 + \tilde f_1 - v_x\left(S_2 + x_{2d}\right) = \hat f_1 + \tilde f_1 - v_x\left(S_2 + y_2 + \bar x_2\right)$$

$$\dot S_1 = \tilde f_1 - v_x S_2 - v_x y_2 - k_1 x_1 \tag{B.9}$$

$$\dot S_2 = \dot x_2 - \dot x_{2d} = \hat f_2 + \tilde f_2 + \frac{u}{I_{zz}} - \dot x_{2d} = \tilde f_2 - k_2\left(x_2 - x_{2d}\right)$$

$$\dot S_2 = \tilde f_2 - k_2 S_2 \tag{B.10}$$

For the boundary layer error, suppose the change of longitudinal velocity is slow, $\dot v_x \approx 0$.

$$\dot y_2 = \dot x_{2d} - \dot{\bar x}_2 = -\frac{y_2}{\tau} - \frac{\dot{\hat f}_1 + k_1 \dot x_1}{v_x}$$

$$\dot y_2 = -\frac{y_2}{\tau} - \frac{1}{v_x}\left(\frac{\partial \hat f_1}{\partial x_1}\dot x_1 + \frac{\partial \hat f_1}{\partial x_2}\dot x_2\right) - \frac{k_1}{v_x}\dot x_1 \tag{B.11}$$

where $\dot x_2 = \dot S_2 + \dot x_{2d} = \tilde f_2 - k_2 S_2 - \frac{y_2}{\tau}$.

Before the evaluation of $S_1\dot S_1$, $S_2\dot S_2$, and $y_2\dot y_2$, first study the upper bounds of $|x_2|$, $|\dot S_1|$, and $|\dot{\bar x}_2|$. According to the definition of the second sliding surface,

$$x_2 = S_2 + x_{2d} = S_2 + y_2 + \bar x_2 \tag{B.12}$$

Since $\bar x_2 = \frac{\hat f_1 + k_1 S_1}{v_x}$, and $\hat f_1$ is bounded as in Eq. (B.3),

$$|\bar x_2| \le \left(\frac{q_{11}}{v_x} + \frac{k_1}{v_x}\right)|S_1| + \frac{q_{12}}{v_x}|x_2| = e_{21}|S_1| + e_{22}|x_2| \tag{B.13}$$

Therefore

$$|x_2| \le |S_2| + |y_2| + |\bar{x}_2| \le |S_2| + |y_2| + e_{21}|S_1| + e_{22}|x_2|$$

As a result

$$|x_2| \le \frac{1}{1-e_{22}}\left(|S_2| + |y_2| + e_{21}|S_1|\right), \text{ provided that } e_{22} < 1 \tag{B.14}$$

$\dot{S}_1$ is given by Eq. (B.9). Thus its upper bound can be derived as

$$|\dot{S}_1| \le |\tilde{f}_1| + v_x|S_2| + v_x|y_2| + k_1|S_1|$$

$$|\dot{S}_1| \le (m_{11} + k_1)|S_1| + v_x|S_2| + v_x|y_2| + \frac{m_{12}}{1-e_{22}}\left(|S_2| + |y_2| + e_{21}|S_1|\right)$$

$$|\dot{S}_1| \le n_{11}|S_1| + n_{12}|S_2| + n_{13}|y_2| \tag{B.15}$$

Take derivative to the synthetic input in Eq. (B.2),

$$\dot{\bar{x}}_2 = \frac{1}{v_x}\left(\frac{\partial \hat{f}_1}{\partial x_1}\dot{x}_1 + \frac{\partial \hat{f}_1}{\partial x_2}\dot{x}_2\right) + \frac{k_1}{v_x}\dot{x}_1$$

The upper bound of $\dot{\bar{x}}_2$ is then given by

$$|\dot{\bar{x}}_2| \le \left(\frac{1}{v_x}\left|\frac{\partial \hat{f}_1}{\partial x_1}\right| + \frac{k_1}{v_x}\right)|\dot{S}_1| + \frac{1}{v_x}\left|\frac{\partial \hat{f}_1}{\partial x_2}\right||\dot{x}_2|$$

$$|\dot{\bar{x}}_2| \le \left(\frac{1}{v_x}\left|\frac{\partial \hat{f}_1}{\partial x_1}\right| + \frac{k_1}{v_x}\right)\left(n_{11}|S_1| + n_{12}|S_2| + n_{13}|y_2|\right) + \frac{1}{v_x}\left|\frac{\partial \hat{f}_1}{\partial x_2}\right|\left(|\tilde{f}_2| + k_2|S_2| + \frac{|y_2|}{\tau}\right)$$

$$|\dot{\bar{x}}_2| \le k_{21}|S_1| + k_{22}|S_2| + k_{23}|y_2| \tag{B.16}$$

Now it is ready to evaluate the derivative of the candidate Lyapunov function

$$\dot{V} = S_1\dot{S}_1 + S_2\dot{S}_2 + y_2\dot{y}_2 \tag{B.17}$$

The first term is expanded and computed by

$$S_1\dot{S}_1 = S_1\left(\tilde{f}_1 - v_x S_2 - v_x y_2 - k_1 x_1\right) \le -k_1 S_1^2 + v_x|S_1||S_2| + v_x|S_1||y_2| + |S_1||\tilde{f}_1|$$

$$|S_1||\tilde{f}_1| \le |S_1|\left(m_{11}|S_1| + m_{12}|x_2|\right) = m_{11}S_1^2 + m_{12}|S_1||x_2|$$

Substitute Eq. (B.14), the upper bound of $S_1\dot{S}_1$ is obtained

$$S_1\dot{S}_1 \le \left(-k_1 + m_{11} + \frac{m_{12}e_{21}}{1-e_{22}}\right)S_1^2 + \left(v_x + \frac{m_{12}}{1-e_{22}}\right)|S_1||S_2| + \left(v_x + \frac{m_{12}}{1-e_{22}}\right)|S_1||y_2| \tag{B.18}$$

For the second term in $\dot{V}$,

$$S_2\dot{S}_2 = S_2\left(\tilde{f}_2 - k_2 S_2\right) \le -k_2 S_2^2 + |S_2|\left|\tilde{f}_2\right|$$

$$|S_2|\left|\tilde{f}_2\right| \le |S_2|\left(m_{21}|S_1| + m_{22}|x_2|\right)$$

Substitute Eq. (B.14), the upper bound of $S_2\dot{S}_2$ is obtained

$$S_2\dot{S}_2 \le \left(-k_2 + \frac{m_{22}}{1-e_{22}}\right)S_2^2 + \left(m_{21} + \frac{m_{22}e_{21}}{1-e_{22}}\right)|S_1||S_2| + \frac{m_{22}}{1-e_{22}}|S_1||y_2| \qquad \text{(B.19)}$$

For the last term in $\dot{V}$,

$$y_2\dot{y}_2 = y_2\left(\dot{x}_{2d} - \dot{\bar{x}}_2\right) \le \left(\frac{-1}{\tau}\right)y_2^2 + |y_2|\left|\dot{\bar{x}}_2\right|$$

Substitute Eq. (B.16),

$$y_2\dot{y}_2 \le \left(\frac{-1}{\tau} + k_{23}\right)y_2^2 + k_{21}|S_1||y_2| + k_{22}|S_2||y_2| \qquad \text{(B.20)}$$

Collect Eqs. (B.18) -(B.20), and further replace non-square terms with inequality

$$|ab| \le \frac{\varepsilon}{2}a^2 + \frac{1}{2\varepsilon}b^2,\ \varepsilon > 0$$

Finally, after algebraic reductions, it can be shown

$$\dot{V} = S_1\dot{S}_1 + S_2\dot{S}_2 + y_2\dot{y}_2 \le \left(-k_1 + \ldots\right)S_1^2 + \left(-k_2 + \ldots\right)S_2^2 + \left(\frac{-1}{\tau} + \ldots\right)y_2^2 \qquad \text{(B.21)}$$

Let $k_1, k_2, \frac{1}{\tau}$ be sufficiently large, then $\dot{V}$ is negative definite. The closed-loop system composed of the plant in Eq. (B.1) and the controller in Eq. (B.2) is exponentially stable.

Appendix C

Estimation of Lateral Velocity and Tire Forces

In practice, it is challenging to directly measure some vehicle response variables, for instance, vehicle lateral velocity and tire forces. They need to be replaced with estimated versions to be used in control algorithms. The estimation scheme used in this study is outlined in Figure C.1. It takes as inputs vehicle longitudinal velocity v_x, yaw rate ω_z, front wheel steering angle δ_f, wheel rotational velocities ω_{wheel}, longitudinal acceleration A_x, lateral acceleration A_y, and body roll angle ϕ, all of which are available from typical chassis control systems. By performing a set of estimation steps, the scheme outputs wheel longitudinal slips λ, tire longitudinal and lateral forces F_x, F_y, tire sideslip angles α, CG lateral velocity v_y, as well as tire normal forces F_z. There are five subsystems inside the estimation scheme: lateral velocity estimation, calculation of tire longitudinal slips, calculation of tire sideslip angles, calculation tire normal forces, and the estimation of planar tire forces. These five blocks are discussed in this appendix.

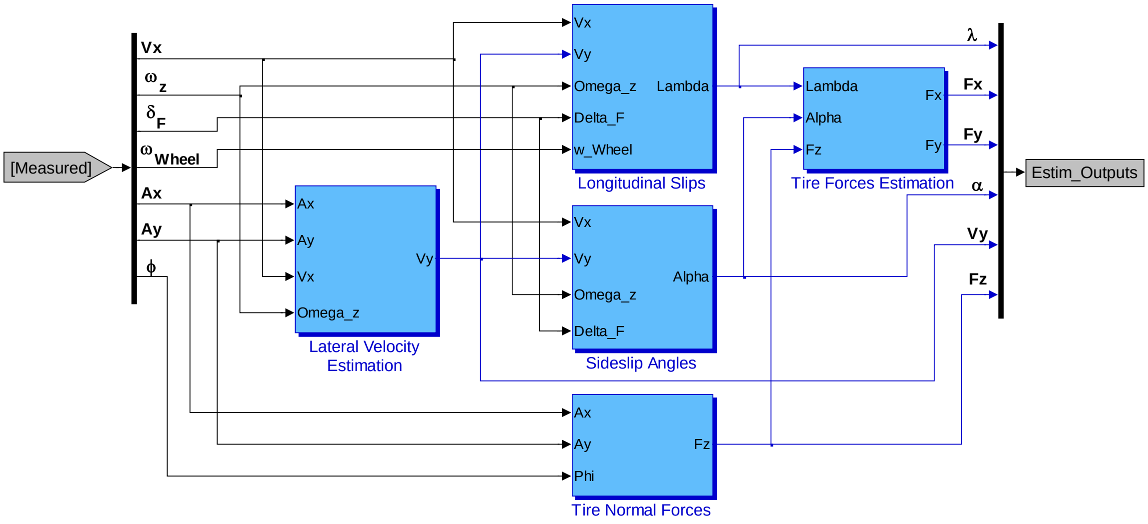

Figure C.1: Block diagram for the estimator of lateral velocity and tire forces

The first major step is to estimate CG lateral velocity, which is not a trivial task and has been approached by a number of studies. The method employed in this work is a kinematics-based lateral velocity estimation adopted from literature [128, 129]. It is chosen because of its ease to implement, if measurements of longitudinal velocity, yaw rate, longitudinal acceleration and lateral acceleration are of high quality, and no substantial road bank angle is present. The estimation is based on the kinematic relationship of the following variables:

$$\begin{cases} A_x = \dot{v}_x - v_y \omega_z \\ A_y = \dot{v}_y + v_x \omega_z \end{cases} \tag{C.1}$$

It can be cast into a state-space formulation

$$\begin{pmatrix} \dot{v}_x \\ \dot{v}_y \end{pmatrix} = \begin{pmatrix} 0 & \omega_z \\ -\omega_z & 0 \end{pmatrix} \cdot \begin{pmatrix} v_x \\ v_y \end{pmatrix} + \begin{pmatrix} A_x \\ A_y \end{pmatrix}, \ v_{xm} = \begin{pmatrix} 1 & 0 \end{pmatrix} \cdot \begin{pmatrix} v_x \\ v_y \end{pmatrix} + n \tag{C.2}$$

$$\text{or } \dot{\mathbf{X}} = \boldsymbol{A} \cdot \mathbf{X} + \boldsymbol{B} \cdot \mathbf{u}, \ \mathbf{Y} = \boldsymbol{C} \cdot \mathbf{X} + n$$

Based on standard observer design, the estimation model is given by

$$\dot{\hat{\mathbf{X}}} = \boldsymbol{A} \cdot \hat{\mathbf{X}} + \boldsymbol{B} \cdot \mathbf{u} + \boldsymbol{L} \cdot \left(\mathbf{Y} - \hat{\mathbf{Y}} \right), \ \hat{\mathbf{X}} = \begin{pmatrix} \hat{v}_x \\ \hat{v}_y \end{pmatrix} \tag{C.3}$$

According to [128], if the observer gains are chosen as

$$\boldsymbol{L} = \begin{pmatrix} 2\xi \left| \omega_z \right| \\ \left(\xi^2 - 1 \right) \cdot \omega_z \end{pmatrix}, (\xi > 0) \tag{C.4}$$

it can be shown the closed-loop poles will be located at $\lambda_{1,2} = -\xi \left| \omega_z \right|$, and the closed-loop system is stable. The convergence rate of the estimates can be adjusted by the positive design parameter ξ.

The second major task is to estimate tire forces. A model-based approach is used for this application. The combined-slip Magic Formula is the underlying tire model because of its capability to account for both cornering and braking forces (even at adhesion limits) and its relatively high modeling accuracy.

Refer to Figure C.1, the signal flow shows that three intermediate blocks are required: longitudinal slips, sideslip angles, and tire normal forces. The tire longitudinal slip is defined in Eq. (4.27). For instance, the slip for the front left (FL) tire is given by

$$\lambda_{FL} = \frac{R_w \omega_{FL}}{V_{FL}} - 1. \tag{C. 5}$$

The linear velocities at wheel hubs are given by

$$V_{FL}=\left(v_x-\frac{T_w}{2}\omega_z\right)\cos\delta_{FL}+\left(v_y+a\omega_z\right)\sin\delta_{FL}\,,\;V_{FR}=\left(v_x+\frac{T_w}{2}\omega_z\right)\cos\delta_{FR}+\left(v_y+a\omega_z\right)\sin\delta_{FR}$$

$$V_{RL}=v_x-\frac{T_w}{2}\omega_z\,,\;V_{RR}=v_x+\frac{T_w}{2}\omega_z \tag{C.6}$$

Similarly, the sideslip angles at four wheels can be computed by

$$\alpha_{FL}=\delta_{FL}-\text{atan}\frac{v_y+a\omega_z}{v_x-\frac{T_w}{2}\omega_z}\,,\;\alpha_{FR}=\delta_{FR}-\text{atan}\frac{v_y+a\omega_z}{v_x+\frac{T_w}{2}\omega_z}$$

$$\alpha_{RL}=-\text{atan}\frac{v_y-b\omega_z}{v_x-\frac{T_w}{2}\omega_z}\,,\;\alpha_{RR}=-\text{atan}\frac{v_y-b\omega_z}{v_x+\frac{T_w}{2}\omega_z} \tag{C.7}$$

δ_{FL} and δ_{FR} refer to road wheel steering angles, obtained through the kinematics of the steering mechanism. Finally, the estimated wheel normal loads vary as follows:

$$F_{zFL}=\frac{Mg}{2}\left(\frac{b}{L}-\frac{a_x}{g}\cdot\frac{h_{CG}}{L}\right)-K_{RSF}\cdot Mg\left(\frac{h_{CG}}{T_W}\cdot\frac{a_y}{g}+\frac{m_R h}{MT_W}\sin\phi\right)$$

$$F_{zFR}=\frac{Mg}{2}\left(\frac{b}{L}-\frac{a_x}{g}\cdot\frac{h_{CG}}{L}\right)+K_{RSF}\cdot Mg\left(\frac{h_{CG}}{T_W}\cdot\frac{a_y}{g}+\frac{m_R h}{MT_W}\sin\phi\right)$$

$$F_{zRL}=\frac{Mg}{2}\left(\frac{a}{L}+\frac{a_x}{g}\cdot\frac{h_{CG}}{L}\right)-\left(1-K_{RSF}\right)\cdot Mg\left(\frac{h_{CG}}{T_W}\cdot\frac{a_y}{g}+\frac{m_R h}{MT_W}\sin\phi\right)$$

$$F_{zRR}=\frac{Mg}{2}\left(\frac{a}{L}+\frac{a_x}{g}\cdot\frac{h_{CG}}{L}\right)+\left(1-K_{RSF}\right)\cdot Mg\left(\frac{h_{CG}}{T_W}\cdot\frac{a_y}{g}+\frac{m_R h}{MT_W}\sin\phi\right) \tag{C.8}$$

where K_{RSF} is the front proportion of total roll stiffness. These estimated tire normal forces are composed of three parts. The first part is due to vehicle static weight. The second part is the load transfer due to longitudinal acceleration without considering pitch dynamics. The third part is the load transfer due to lateral acceleration and sprung mass roll motion. In both load transfer cases, the suspension damping is ignored, so the estimated values are essentially based on quasi-static state moment balance.

In summary, if nominal vehicle parameters, tire fitting coefficients and road friction coefficient are specified, the estimation scheme shown in Figure C.1 can be used to estimate CG lateral velocity and tire forces. The estimation accuracy will be affected by the closeness of nominal values to true values and the quality of sensor measurements.

Bibliography

Bibliography

[1] Seiffert, U.W., Wech, L.: *Automotive Safety Handbook*. SAE International, Warrendale, PA (2003).

[2] Girling, P.: *Driving-Safety Systems*, Robert Bosch GmbH. SAE International, Warrendale, PA (1999).

[3] van Zanten, A., Erhardt , R., *et al*.: Simulation for the Development of the Bosch-VDC. *SAE Technical Paper* 960486 (1996).

[4] Vahidi, A. and Eskandarian, A.: Research Advances in Intelligent Collision Avoidance and Adaptive Cruise Control. IEEE Trans. on Intelligent Transportation Systems, **4** (3), pp. 143–153 (2003).

[5] Zhou, J. and Peng, H.: Range Policy of Adaptive Cruise Control for Improved Flow Stability and String Stability. IEEE Trans. on Intelligent Transportation Systems, **6** (2), pp. 229-237 (2005).

[6] Eidehall, A., Pohl, J., *et al*.: Toward Autonomous Collision Avoidance by Steering. IEEE Trans. on Intelligent Transportation Systems, **8** (1), pp. 84–94 (2007).

[7] Peters, G. and Peters, B.J.: *Automotive Vehicle Safety*. CRC Press, Boca Raton, FL, (2002).

[8] NHTSA: Traffic Safety Facts 2006. NHTSA Report DOT HS 810 818 (2008).

[9] Lu, J., Personal communication (2006).

[10] Lu, J., *et al.*, “Enhanced Yaw Stability Control to Mitigate a Vehicle's Abnormal Yaw Motion due to a Disturbance Force Applied to Vehicle Body”, Patent Publication WO/2007/044744, World Intellectual Property Organization (2007).

[11] Langwieder, K., Sporner, A., Hell, W.: RESICO – Retrospective Safety Analysis of Car Collisions Resulting in Serious Injuries. GDV 9810, Munich, Germany (1999).

[12] Accident case number NASS-CDS 2003-079-057, http://www-nass.nhtsa.dot.gov.

[13] Zhou, J. and Peng, H.: Feedforward and Feedback Control of Lane Keeping by the Human Driver. IMECE 2007-41337, Proc. 2007 ASME Conf., Seattle, WA (2007).

[14] Jansson, J., Eidehall, A., and Pohl, J.: Systems for Collision Avoidance in Road Vehicles. IVSS (Intelligent Vehicle Safety Systems) Project Report, Sweden (2007).

[15] Christoffel, T. and Gallagher, S. S.: Injury Prevention and Public Health Practical Knowledge, Skills and Strategies. 2nd Ed. Jones and Bartlett Publishers (2006).

[16] Chan, C.-Y. and Tan, H.-S.: Feasibility Analysis of Steering Control as a Driver-Assistance Function in Collision Situations. IEEE Trans. on Intelligent Transportation Systems, **2** (1), pp. 1–9 (2001).

[17] More safety in accidents: Secondary Collision Mitigation from Bosch. Retrieved August 06, 2007, from http://www.bosch-presse.de.

[18] Tseng, H.E., Ashrafi, B., Madau, D., Brown, T.A. and Recker, D.: The Development of Vehicle Stability Control at Ford. IEEE/ASME Trans. on Mechatronics, **4** (3), pp. 223–234 (1999).

[19] Hoffman, D.D. and Michael, D.R.: Chevrolet C5 Corvette Vehicle Dynamic Control System. *SAE Technical Paper* 980233 (1998).

[20] Leffler, H., Auffhammer, R., Heyken, R. and Roeth, H.: New Driving Stability Control System with Reduced Technical Effort for Compact and Medium Class Passenger Cars. *SAE Technical Paper* 980234 (1998).

[21] van Zanten, A.T., Erhardt, R., Pfaff, G.: VDC, the Vehicle Dynamics Control System of Bosch. *SAE Technical Paper* 950759 (1995).

[22] Ackermann, J., Guldner, J., Sienel, R., et al.: Linear and Nonlinear Controller Design for Robust Automatic Steering. IEEE Trans. Control Systems Technology, **3** (1), pp. 132–143 (1995).

[23] Mammer, S. and Koenig, D.: Vehicle Handling Improvement by Active Steering. Vehicle System Dynamics, **38** (3), pp. 211–242 (2002).

[24] Nagai, M., and Ohki, M.: Theoretical Study on Active Four-Wheel-Steering System by Virtual Vehicle Model Following Control. JSAE Review, **9** (4), pp. 62–71 (1988).

[25] Dang, J. N.: Preliminary Results Analyzing the Effectiveness of Electronic Stability Control (ESC) Systems. NHTSA Report, DOT HS 809 790 (2004).

[26] Lie, A., Tingvall, C., Krafft, M., and Kullgren, A.: The Effectiveness of Electronic Stability Control (ESC) in Reducing Real Life Crashes and Injuries. Traffic Injury Prevention, **7** (1), pp. 38–43 (2006).

[27] Farmer, C. M.: Effect of Electronic Stability Control on Automobile Crash Risk. Traffic Injury Prevention, **5**, pp. 317–325 (2004).

[28] Zhou, J., Lu, J., and Peng, H.: Vehicle Dynamics in Response to the Maneuver of Precision Immobilization Technique. ASME Dynamic Systems and Control Conf. DSCC2008-2183, Ann Arbor, MI (2008).

[29] Ghoneim, Y.A., *et al.*: Integrated Chassis Control System to Enhance Vehicle Stability. Intl. Journal of Vehicle Design, **23** (1/2), pp. 124–144 (2000).

[30] Nagai, M., Shino, M., and Feng, G.: Study on Integrated Control of Active Front Steer Angle and Direct Yaw Moment. JSAE Review, **23** (3), pp. 309–315 (2002).

[31] Thor, M.: The Efficiency of Electronic Stability Control after Light Collisions, Master's Thesis, Chalmers University of Technology, Goeteborg, Sweden (2007).

[32] Caird, J.K. ,Lees, M. and Edwards, C.: The Naturalistic Driver Model: A Review of Distraction, Impairment and Emergency Factors. California PATH Research Report UCB-ITS-PRR-2005-4 (2005).

[33] Olson, P.L., and Farber, E.: Forensic aspects of driver perception and response. 2nd Ed., Lawyers and Judges Publishing (2002).

[34] Babu, V., Thomson, K.R., and Sakatis, C.: LS-DYNA 3D Interface Component Analysis to Predict FMVSS 208 Occupant Responses. *SAE Technical Paper* 2003-01-1294 (2003).

[35] Solanki, K., Oglesby, D.L., Burton, C.L., *et al.*: Crashworthiness Simulations Comparing PAM-CRASH and LS-DYNA. *SAE Technical Paper* 2004-01-1174 (2004).

[36] Day, T. D.: An Overview of the EDSMAC4 Collision Simulation Model. *SAE Technical Paper* 1999-01-0102 (1999).

[37] Steffan, H. and Moser, A.: The Collision and Trajectory Models of PC-CRASH. *SAE Technical Paper* 960886 (1996).

[38] McHenry, R.: Development of a Computer Program to Aid the Investigation of Highway Accidents. Calspan Report No. VJ-2979-V-1, DOT HS-800 821 (1971).

[39] Brach, R.M.: Mechanical Impact Dynamics: Rigid Body Collisions. Wiley, New York, 1991.

[40] Brach, R.M. and Brach, R.M.: *Vehicle Accident Analysis and Reconstruction Methods*. SAE, Warrendale, PA, 2005.

[41] Brach, R.M. and Brach, R.M.: Crush Energy and Planar Impact Mechanics for Accident Reconstruction. *SAE Technical Paper* 980025 (1998).

[42] Cipriani, A.L., Bayan, F.P., Woodhouse, M.L., *et al.*: Low Speed Collinear Impact Severity, A Comparison between Full Scale Testing and Analytical Prediction Tools with Restitution Analysis. *SAE Technical Paper* 2002-01-0540 (2002).

[43] Zhou, J., Peng, H., and Lu, J.: Collision Model for Vehicle Motion Prediction after Light Impacts. *Vehicle System Dynamics*, **46**, Suppl. 1, pp. 3-15 (2008).

[44] Cannon, J.W: Dependence of a Coefficient of Restitution on Geometry for High Speed Vehicle Collisions. *SAE Technical Paper* 2001-01-0892 (2001).

[45] Antonetti, V.W.: Estimating the Coefficient of Restitution of Vehicle-to-Vehicle Bumper Impacts. *SAE Technical Paper* 980552 (1998).

[46] Brach, R.M.: Modeling of Low-Speed, Front-to-Rear Vehicle Impacts. *SAE Technical Paper* 2003-01-0491 (2003).

[47] Monson, K.L. and Germane, G.J.: Determination and Mechanisms of Motor Vehicle Structural Restitution from Crash Test Data. *SAE Technical Paper* 1999-01-0097 (1999).

[48] Marine, M.C.: On the Concept of Inter-Vehicle Friction and Its Application in Automobile Accident Reconstruction. *SAE Technical Paper* 2007-01-0744 (2007).

[49] Segel, L.: Theoretical Prediction and Experimental Substantiation of the Response of the Automobile to Steering Control. *Proc. IMechE*, pp.310–330 (1956).

[50] Gillespie, T.D.: Fundamentals of Vehicle Dynamics. Society of Automotive Engineers, Warrendale, PA, 1992.

[51] Anderson, R.D., *et al.*: Effect of Braking on Human Occupant and Vehicle Kinematics in Low Speed Rear-End Collisions. *SAE Technical Paper* 980298 (1998).

[52] Huang, M.: *Vehicle Crash Mechanics*. CRC Press, Boca Raton, FL (2000).

[53] Varat, M.S. and Husher, S.E.: Vehicle Impact Response Analysis through the Use of Accelerometer Data. *SAE Technical Paper* 2000-01-0850 (2000).

[54] Mechanical Simulation Corporation. CarSim User Manual. Homepage http://www.carsim.com, 2007.

[55] Ashley, S.: Reducing the Risks of Police Pursuit. *Police and Security News*, **18** (5), September/October (2002).

[56] Eisenberg, C.: Pursuit Management. *Law & Order*, **47** (3), March, pp. 73–77 (1999).

[57] "Hot Pursuit - Going For a Spin." See URL http://www.trutv.com/video/index.html

[58] Court case Scott v. Harris, No. 05–1631, U.S. Supreme Court, April 30 2007. See also URL http:// www.supremecourtus.gov/opinions/06slipopinion.html

[59] Chan, C-Y.: Fundamentals of Crash Sensing in Automotive Air Bag Systems. Society of Automotive Engineers, Warrendale, PA (2000).

[60] Chan, C-Y.: On the Detection of Vehicular Crashes – System Characteristics and Architecture. IEEE Trans. on Vehicular Technology, **51** (1), pp. 180-193 (2002).

[61] Chan, C-Y.: A Treatise on Crash Sensing for Automotive Air Bag Systems. IEEE/ASME Trans. on Mechatronics, **7** (2), pp. 220-234 (2002).

[62] Winkler, G., Stierle, T. and Malbouef, T.: Side-Impact Restraint Activation System Combining Acceleration and Dynamic-Pressure Sensing. *SAE Technical Paper* 2003-01-0197 (2003).

[63] Jeong, H-Y. and Kim, Y-H.: New algorithm and Accelerometer Locations for Frontal Crash Discrimination. IMechE, Proc. Instn. Mech. Engrs., 215 Part D, pp. 1171-1178 (2001).

[64] Hedrick, J.K. and Yip, P.P.: Multiple Sliding Surface Control: Theory and Application, *ASME Journal of Dynamic Systems, Measurement and Control*, 122, pp. 586–593 (2000).

[65] Yip, P.P.: Robust and Adaptive Nonlinear Control Using Dynamic Surface Controller with Applications to Intelligent Vehicle Highway Systems, Ph. D. Dissertation, UC Berkeley (1997).

[66] Layne, J.R., Passino, K.M. and Yurkovich, S.: Fuzzy Learning Control for Anti-Skid Braking Systems. IEEE Trans. Control Systems Technology, **1** (2), pp. 122–129 (1993).

[67] Mauer, G.F.: A Fuzzy Logic Controller for an ABS Braking System. IEEE Trans. Fuzzy Systems, **3** (4), pp. 381–388 (1995).

[68] Drakunov, S., Ozguner, U., Dix, P., and Ashrafi, B.: ABS Control Using Optimum Search via Sliding Modes. IEEE Trans. Control Systems Technology, **3** (1), pp. 79–85 (1995).

[69] Unsal, C., and Kachroo, P.: Sliding Mode Measurement Feedback Control for Antilock Braking Systems. IEEE Trans. Control Systems Technology, **7** (2), pp. 271–281 (1999).

[70] Bang, M.S., Lee, S.H., Han, C.S., Maciuca, D.B. and Hedrick, J.K.: Performance Enhancement of a Sliding Mode Wheel Slip Controller by the Yaw Moment Control. Proc. ImechE, Vol. 215, Part D, pp. 455–468 (2001).

[71] Slotine, J.J.E. and Li, W.: *Applied Nonlinear Control*. Prentice-Hall (1991).

[72] TESIS DYNAware Technische Simulation Dynamischer Systeme GmbH. veDYNA Homepage http://www.tesis.de/en/index.php?page=544 (2007).

[73] Inagaki, S., Kshiro, I., and Yamamoto, M.: Analysis on Vehicle Stability in Critical Cornering Using Phase-Plane Method. Proc. 2nd Intl. Symposium on Advanced Vehicle Control (AVEC), Tsukuba, Japan (1994).

[74] Ono, E., Hosoe, S., Tuan, H. D. and Doi, S.: Bifurcation in Vehicle Dynamics and Robust Front Wheel Steering Control. IEEE Trans. Control Systems Technology, **6** (3), pp. 412-420 (1998).

[75] Kiencke, U. and Nielsen, L.: Automotive Control Systems. Springer-Verlag (2000).

[76] Shibahata, Y., Shimada, K., and Tomari, T.: Improvement of Vehicle Maneuverability by Direct Yaw Moment Control. Vehicle System Dynamics, **22**, pp. 465–481 (1993).

[77] Peng, H., and Hu, J.-S.: Traction/Braking Force Distribution for Optimal Longitudinal Motion during Curve Following. Vehicle System Dynamics, **26**, pp. 301–320 (1996).

[78] Hattori, Y., Koibuchi, K., and Yokoyama, T.: Force and Moment Control with Nonlinear Optimum Distribution for Vehicle Dynamics. Proc. 6th International Symposium on Advanced Vehicle Control (AVEC), Hiroshima, Japan (2002).

[79] Ono, E., Hattori, Y., Muragishi, Y. and Koibuchi, K.: Vehicle Dynamics Integrated Control for Four-Wheel-Distributed Steering and Four-Wheel-Distributed Traction/Braking Systems. Vehicle System Dynamics, **44** (2), pp. 139-151 (2006).

[80] Mokhiamar, O. and Abe, M.: Effects of Optimum Cooperative Chassis Control from the Viewpoint of Tire Workload. ASME Journal of Dynamic Systems, Measurement and Control **126** (12), pp. 753 -763 (2004).

[81] Page. A. B. and Steinberg, M. L.: A Closed-Loop Comparison of Control Allocation Methods, AIAA-200-4538, AIAA Guidance, Navigation, and Control Conference and Exhibit, Denver, CO (2000).

[82] Burken, J., Lu, P., Wu, Z., and Bahm, C.: Two Reconfigurable Flight–Control Design Methods: Robust Servomechanism and Control Allocation. Journal of Guidance, Control, and Dynamics, **24** (3), pp. 482–493 (2001).

[83] Fossen, T., Johansen, T., and Berge, S.: Constrained Nonlinear Control Allocation with Singularity Avoidance Using Sequential Quadratic Programming. IEEE Trans. Control Systems Technology, **12** (2004).

[84] Johansen, T., Fuglseth, T., Tøndel, P., and Fossen, T.: Optimal Constrained Control Allocation in Marine Surface Vessels with Rudders. IFAC Conf. Manoeuvring and Control of Marine Craft, Girona (2003).

[85] Plumlee, J. H., Bevly, D. M., and Hodel, A. S.: Control of a Ground Vehicle Using Quadratic Programming Based Control Allocation Techniques. Proc. American Control Conf., Boston (2004).

[86] Wang, J., Solis, J.M., and Longoria, R.G.: On the Control Allocation for Coordinated Ground Vehicle Dynamics Control Systems. Proc. American Control Conf., New York City (2007).

[87] Maciejowski, J.M.: Predictive Control with Constraints. Prentice Hall (2002).

[88] Agachi, P. S., Nagy, Z. K., Cristea, M. V., and Imre-Lucaci, A.: Model Based Control: Case Studies in Process Engineering, Wiley-VCH, Weinheim, Germany (2006).

[89] Qin, S.J. and Badgwell, T.A.: A Survey of Industrial Model Predictive Control Technology. Control Engineering Practice, **11**, pp.733-746 (2003).

[90] Kwon, W.-H., Han, S.: Receding Horizon Control: Model Predictive Control for State Models. Springer, London (2005).

[91] Rawlings, J. B.: Tutorial Overview of Model Predictive Control. IEEE Control Systems Magazine, **20**, pp. 38–52 (2000).

[92] Mayne, D., Rawlings, J., Rao, C., and Scokaert, P.: Constrained Model Predictive Control: Stability and Optimality. Automatica, **36** (6), pp. 789–814 (2000).

[93] Nikolaou, M.: Model Predictive Controllers: A Critical Synthesis of Theory and industrial Needs. In: Stephanopoulos, G. (Ed.), Advances in Chemical Engineering Series, Academic Press, New York (2001).

[94] Garcia, C.E, Prett, D.M., and Morari, M.: Model Predictive Control: Theory and Practice - a Survey. Automatica, **25** (3), pp.335-348 (1989).

[95] Camacho, E.F. and Bordons, C.: Model Predictive Control. Second Edition, Springer, London (2004).

[96] Falcone, P., Bemporad, A., Fodor, M. and Hrovat, D.: An MPC/Hybrid System Approach to Traction Control. IEEE Trans. Control Systems Technology, **14** (3), pp. 541–552 (2006).

[97] Falcone, P., Borrelli, F., Asgari, J., Tseng, H. E. and Hrovat, D.: Predictive Active Steering Control for Autonomous Vehicle Systems. IEEE Trans. Control Systems Technology, **15** (3), pp. 566–580 (2007).

[98] Falcone, P., Tseng, H. E., Borrelli, F., Jahan, A. and Hrovat, D.: MPC-based Yaw and lateral Stabilisation via Active Front Steering and Braking. Vehicle System Dynamics. **46**, Supp. 1, pp. 611–628 (2008).

[99] Chang, S. and Gordon, T.J.: Model-based Predictive Control of Vehicle Dynamics. Intl. Journal of Vehicle Autonomous System. **5** (1/2), pp. 3–27 (2007).

[100] Chang, S. and Gordon, T.J.: A Flexible Hierarchical Model-Based Control Methodology for Vehicle Active Safety Systems. Vehicle System Dynamics, **46**, Supp. 1, pp. 63-75 (2008).

[101] Carlson, C. R. and Gerdes, J.C.: Optimal Rollover Prevention with Steer by Wire and Differential Braking. Proc. ASME IMECE 2003-41825 (2003).

[102] Hattori, Y., Ono, E. and Hosoe, S.: Optimum Vehicle Trajectory Control for Obstacle Avoidance Problem. IEEE/ASME Trans. Mechatronics, **11** (5), pp. 507 -512 (2006).

[103] Rossiter, J.A.: Model-based Predictive Control: a Practical Approach, CRC Press (2004).

[104] MathWorks: Optimization Toolbox User's Guide, Version 4 (2008).

[105] Wang, J. and Longoria, R. G.: Coordinated Vehicle Dynamics Control with Control Distribution. Proc. American Control Conf. (2006).

[106] Schiebahn, M., Zegelaar, P.W.A., Lakehal-Ayat, M., Hofmann, O.: Analysis and Coordination of Multiple Active Systems for Vehicle Dynamics Controls. Proc. 9th International Symposium on Advanced Vehicle Control (AVEC), Kobe Japan (2008).

[107] Hac, A., Doman, D. and Oppenheimer, M.: Unified Control of Brake- and Steer-by-Wire Systems Using Optimal Control Allocation Methods. SAE Technical Paper 2006-01-0924 (2006).

[108] Tøndel, P., Johansen, T. A.: Control Allocation for Yaw Stabilization in Automotive Vehicles using Multiparametric Nonlinear Programming. Proc. American Control Conf., Portland, OR (2005).

[109] Kay, S. M.: Fundamentals of Statistical Signal Processing: Estimation Theory. New Jersey, USA: Prentice-Hall (1993).

[110] Loetstedt, P.: Solving the Minimal Least Squares Problem Subject to Bounds on the Variables, BIT, **24**, pp. 206-224 (1984).

[111] Stark, P.B. and Parker, R.L.: Bounded Variable Least Squares: An Algorithm and Applications'. Journal of Computational Statistics, **10**, pp. 129-141 (1995).

[112] Björck, Å.: Numerical Methods for Least Squares Problems. Philadelphia: SIAM (1996).

[113] Coleman, T.F. and Li, Y.: A Reflective Newton Method for Minimizing a Quadratic Function Subject to Bounds on Some of the Variables. SIAM Journal on Optimization, **6** (4), pp. 1040-1058 (1996).

[114] Wong, J.Y.: Theory of Ground Vehicles, 3rd Edition. John Wiley & Sons (2001).

[115] Svendenius, J. and Gäfvert, M.: A Brush-Model Based Semi-Empirical Tire-Model for Combined Slips. *SAE Technical Paper* 2004-01-1064 (2004).

[116] Dugoff, H., Fancher, P.S., and Segel, L.: An Analysis of Tire Traction Properties and their Influence on Vehicle Dynamic Performance. *SAE Technical Paper* 700377 (1970).

[117] Guntur, R. and Sankar, S.: A Friction Circle Concept for Dugoff's Tyre Friction Model. Intl. J. Vehicle Design, **1** (4), pp 373-377 (1980).

[118] Van Zanten, A.T., Erhardt, R., Pfaff, G., Kost, F., Hartmann, U., and Ehret, T.: Control Aspects of the Bosch-VDC. Proc. Intl. Sym. on Advanced Vehicle Control, pp. 573-608 (1996).

[119] Smith, D.E., and Starkey, J.M.: Effects of Model Complexity on the Performance of Automated Vehicle Steering Controllers: Model Development, Validation and Comparison. Veh. Syst. Dyn., **24**, pp. 163–181 (1995).

[120] Wang, J. and Longoria, R. G.: Coordinated Vehicle Dynamics Control with Control Distribution. Proc. American Control Conf., Minneapolis, MN (2006).

[121] Gerdes, J.C. and Rossetter, E.J.: A Unified Approach to Driver Assistance Systems Based on Artificial Potential Fields. J. Dynamic Systems, Measurement, and Control, **123** (3), pp. 431-438 (2001).

[122] Pacejka, H.B. and Bakker, E.: The Magic Formula Tyre Model. Veh. Sys. Dyn., Vol. 21, Supplement, Tyre Models for Vehicle Dynamics Analysis, pp. 1-18 (1993).

[123] Pacejka, H. B.: Tire and Vehicle Dynamics (Second edition). SAE International (2005).

[124] Gordon, T. J.: ME 542 Vehicle Dynamics Coursepack Section 3.3. University of Michigan (2007).

[125] Gordon, T. J. and Best, M. C.: On the Synthesis of Driver Inputs for the Simulation of Closed-loop Handling Manoeuvres. Int. J. of Vehicle Design, **40** (1-3), pp. 52-76 (2006).

[126] Pasterkamp, W. R. and Pacejka, H. B.: On-line Estimation of Tyre Characteristics for Vehicle Control. Proc. 2nd Intl. Symposium on Advanced Vehicle Control (AVEC), Tsukuba, Japan (1994).

[127]Boyd, S. and Vandenberghe, L.: Convex Optimization. Cambridge University Press, New York, NY (2004).

[128] Ungoren, A.Y., Peng, H., and Tseng, H.E.: A Study on Lateral Speed Estimation Methods. Intl. J. Vehicle Autonomous Systems, **2** (1/2), pp.126-144 (2004).

[129] Farrelly, J. and Wellstead, P.: Estimation of Vehicle Lateral Velocity. Proc. 1996 IEEE Intl. Conf. on Control Applications, Dearborn, MI, pp.552-557 (1996).